Applied Research Laboratory

Technical Report

THE EFFECTS OF SEDIMENT POROSITY ON ACOUSTIC REFLECTION AND TRANSMISSION AT THE SEAFLOOR

by

Charles W. Holland

PENNSTATE

The Pennsylvania State University
APPLIED RESEARCH LABORATORY
P.O. Box 30
State College, PA 16804

THE EFFECTS OF SEDIMENT POROSITY ON ACOUSTIC REFLECTION AND TRANSMISSION AT THE SEAFLOOR

by

Charles W. Holland

Technical Report No. TR 91-012
October 1991

Supported by:
Space and Naval Warfare Systems Command

L.R. Hettche, Director
Applied Research Laboratory

REPORT DOCUMENTATION PAGE

Form Approved
OMB No. 0704-0188

1. AGENCY USE ONLY (Leave blank)	2. REPORT DATE	3. REPORT TYPE AND DATES COVERED
	May 1991	

4. TITLE AND SUBTITLE

The Effects of Sediment Porosity on Acoustic Reflection and Transmission at the Seafloor

5. FUNDING NUMBERS

N-00039-88-C-0051

6. AUTHOR(S)

Charles William Holland

7. PERFORMING ORGANIZATION NAME(S) AND ADDRESS(ES)

Penn State University
Applied Research Laboratory
P.O. Box 30
State College, PA 16804

8. PERFORMING ORGANIZATION REPORT NUMBER

TR#91-012

9. SPONSORING / MONITORING AGENCY NAME(S) AND ADDRESS(ES)

Space and Naval Warfare Systems Command
Department of the Navy
Washington, DC 20363-5100

10. SPONSORING / MONITORING AGENCY REPORT NUMBER

11. SUPPLEMENTARY NOTES

12a. DISTRIBUTION / AVAILABILITY STATEMENT

12b. DISTRIBUTION CODE

13. ABSTRACT *(Maximum 200 words)*

The Biot theory of propagation in a porous medium provides a mathematical framwork for studying acoustic interaction with the seafloor. The theory considers the two-phase porous nature of marine sediments in contrast to the classical models of wave propagation in the seafloor that consider marine sediments as an extended single-phase fluid or solid. A boundary value problem is set up and solved for a line source in a fluid medium above a poro-viscoelastic halfspace. Expressions for the reflected and transmitted field are given in integral form and asymptotic expansions in the high-frequency, far-field limit. A set of simultaneous equations is solved to give plane wave reflection and transmission (Type I, Type II and shear wave) coefficients. These equations also yield the Scholte, pseudo-Scholte and pseudo-Rayleigh wave phase velocities and attenuations. The plan wave coefficients and the surface wave velocities and attenuations are compared with commensurate quantities from the single-phase theories. A number of recent experiments of high frequency transmission through a water-sand interface have indicated anomalously high transmitted energy at angles near the critical angle. The Type II wave (predicted by Biot theory but not the single-phase theories) was suspected as a possible reason for the anomalies. Data from one of the experiments are examined using Biot theory to

14. SUBJECT TERMS	15. NUMBER OF PAGES
sediment porosity, seafloor, reflection, transmission, porous medium, acoustic interaction, two-phase, water-sand interface, Biot theory	145
	16. PRICE CODE

17. SECURITY CLASSIFICATION OF REPORT	18. SECURITY CLASSIFICATION OF THIS PAGE	19. SECURITY CLASSIFICATION OF ABSTRACT	20. LIMITATION OF ABSTRACT
Unclassified	Unclassified	Unclassified	

(cont)

determine whether or not the Type II wave was responsible for the anomalies. Calculations indicate that the contributions from the Type II wave are negligible and thus not the cause of anomalies. Much of the anomalous behavior appeared to arise simply as a result of an incorrect compressional wave attenuation in the geoacoustic model.

ABSTRACT

The Biot theory of propagation in a porous medium provides a mathematical framework for studying acoustic interaction with the seafloor. The theory considers the two-phase porous nature of marine sediments in contrast to the classical models of wave propagation in the seafloor that consider marine sediments as an extended single-phase fluid or solid. A boundary value problem is set up and solved for a line source in a fluid medium above a poro-viscoelastic halfspace. Expressions for the reflected and transmitted field are given in integral form and asymptotic expansions in the high-frequency, far-field limit. A set of simultaneous equations is solved to give plane wave reflection and transmission (Type I , Type II and shear wave) coefficients. These equations also yield the Scholte, pseudo-Scholte, and pseudo-Rayleigh wave phase velocities and attenuations. The plane wave coefficients and the surface wave velocities and attenuations are compared with commensurate quantities from the single-phase theories.

A number of recent experiments of high frequency transmission through a water-sand interface have indicated anomalously high transmitted energy at angles near the critical angle. The Type II wave (predicted by Biot theory but not the single-phase theories) was suspected as a possible reason for the anomalies. Data from one of the experiments are examined using Biot theory to determine whether or not the Type II wave was responsible for the anomalies. Calculations indicate that the contributions from the Type II wave are negligible and thus not the cause of the anomalies. Much of the anomalous behavior appeared to arise simply as a result of an incorrect compressional wave attenuation in the geoacoustic model.

TABLE OF CONTENTS

Page

LIST OF FIGURES vi

LIST OF TABLES ix

LIST OF SYMBOLS x

ACKNOWLEDGEMENTS xiii

Chapter

1. INTRODUCTION 1

1.1 Background 1

1.2 Objective and Approach 3

2. THEORY I - FORWARD TRANSFORM 6

2.1 The Fluid 6

2.2 The Poro-viscoelastic Halfspace 12
2.2.1 Equation of Motion 12
2.2.2 Wave Velocities and Attenuations 20

2.3 Application of the Boundary Conditions 35

3. PLANE WAVE COEFFICIENTS AND SURFACE WAVES 37

3.1 Exact Solution for Plane Wave Coefficients 37
3.1.1 Single Phase Media 37
3.1.2 Two-Phase Porous Media 42

3.2 Implications for Acoustic Propagation Predictions 51
3.2.1 Sand 51
3.2.2 Silty Clay 52
3.2.3 Sandstone 55

TABLE OF CONTENTS (Continued)

3.3 Approximate Models 55

3.4 Interface Waves 63
3.4.1 Sand 65
3.4.2 Silty Clay 65
3.4.3 Sandstone 70

3.5 Summary and Conclusions 75

4. THEORY II - INVERSE TRANSFORM 77

4.1 Mixed Approach 77
4.1.1 Field in Upper Halfspace 77
4.1.2 Field in Lower Halfspace 87

4.2 FFT Evaluation of Field Integrals 99

4.3 Comparison of Two Approaches 101
4.3.1 Upper Halfspace 101
4.3.2 Lower Halfspace 103

4.4 Summary and Conclusions 103

5. COMPARISONS WITH EXPERIMENTAL DATA 108

5.1 The Sediment Model 112

5.2 Sound Pressure Level Comparisons 124

5.3 Summary and Conclusions 129

6. SUMMARY AND CONCLUSIONS 132

BIBLIOGRAPHY 135

APPENDIX A: DEFINITION OF THE COMPLEX ELASTIC MODULI 142

APPENDIX B: NUMERICAL METHODS 143

APPENDIX C: LOCATION OF THE VIRTUAL SOURCE 144

LIST OF FIGURES

Figure		Page
2.1	Path of integration in the complex k_z plane for (z-h) < 0	7
2.2	Path of integration in the complex k_z plane for (z-h) > 0	8
2.3	Type I wave phase velocity for carbonate sand	22
2.4	Type II and shear wave phase velocity for carbonate sand	23
2.5	Type I wave attenuation for carbonate sand	24
2.6	Type II wave attenuation for carbonate sand	25
2.7	Shear wave attenuation for carbonate sand	26
2.8	Type I wave phase velocity for silty clay	28
2.9	Type II and shear wave phase velocity for silty clay	29
2.10	Type I wave attenuation for silty clay	30
2.11	Type II and shear wave attenuation for silty clay	31
2.12	Type I, Type II, and shear wave phase velocity for sandstone	32
2.13	Type I and shear wave attenuation for sandstone	33
2.14	Type II wave attenuation for sandstone	34
3.1	Plane wave reflection coefficients at a fluid-lossy fluid boundary	39
3.2	Plane wave reflection coefficients at a fluid-viscoelastic boundary	41
3.3	Plane wave reflection coefficients at a fluid-poro-viscoelastic boundary. The sediment is sand.	44
3.4	Pseudo-critical angle for a poro-viscoelastic sand from Biot theory	45
3.5	Type II wave transmissivity for poro-viscoelastic sand	47
3.6	Plane wave reflection coefficients at a fluid-poro-viscoelastic boundary. The sediment is silty-clay.	48
3.7	Plane wave reflection coefficients at a fluid-poro-viscoelastic boundary. The sediment is sandstone.	49
3.8	Plane wave transmission coefficients at a fluid-poro-viscoelastic boundary. The sediment is sandstone.	50

Figure | Page

3.9 Comparison of reflectivity from a commonly used geoacoustic extrapolation technique with Biot theory. The sediment is sand..... 53

3.10 Comparison of reflectivity from a commonly used geoacoustic extrapolation technique with Biot theory. The sediment is silty clay..... 54

3.11 Comparison of reflectivity from a commonly used geoacoustic extrapolation technique with Biot theory. The sediment is sandstone..... 56

3.12 Comparison of Biot theory with an approximate model (#). The sediment is sand..... 57

3.13 Comparison of Biot theory with an approximate model (#). The sediment is sandstone..... 60

3.14 Comparison of Biot theory with the constant phase velocity approximate model (*)..... 61

3.15 Comparison of Biot theory with the constant phase velocity approximate model (*)..... 62

3.16 Phase velocity of various wave types in carbonate sand..... 66

3.17 Attenuation of various wave types in carbonate sand..... 67

3.18 Phase velocity of various wave types in silty clay..... 68

3.19 Attenuation of various wave types in silty clay..... 69

3.20 Phase velocity of various wave types in sandstone..... 71

3.21 Attenuation of various wave types in sandstone..... 72

3.22 Phase velocity of various wave types in sandstone..... 73

3.23 Attenuation of various wave types in sandstone..... 74

4.1 Coordinate system for the reflected field,'h' is the source height..... 79

4.2 Complex θ Plane for the Reflected Field..... 82

4.3 Deformation of steepest descent path..... 84

4.4 Pseudo-Scholte wave pole location in the complex angle plane for sand..... 88

4.5 Pseudo-Scholte wave pole location in the complex angle plane for silty clay..... 89

Figure Page

4.6 Pseudo-Scholte wave pole location in the complex angle plane for sandstone. 90

4.7 Coordinate system for the transmitted field. 93

4.8 Reflected plus image source field at 100 Hz calculated by FFT, numerical integration, and asymptotic expansion. The source and receiver are 50 m above a poro-viscoelastic silty clay halfspace. 103

4.9 Reflected plus image source field at 100 Hz calculated by FFT, numerical integration, and asymptotic expansion. The source and receiver are 20 m above a poro-viscoelastic sand halfspace. 104

4.10 Reflected plus image source field at 10 Hz calculated by FFT and numerical integration. The source and receiver are on the boundary of a poro-viscoelastic sand halfspace. 105

4.11 Transmitted field at 100 Hz calculated by FFT, numerical integration, and asymptotic expansion. The source and receiver are respectively 20 m above and below a poro-viscoelastic sand halfspace. 107

5.1 Layout of the experiment. 110

5.2 Type I wave velocity predicted by Biot theory 115

5.3 Type I wave attenuation predicted by Biot theory 116

5.4 Type II wave velocity predicted by Biot theory 117

5.5 Type II wave attenuation predicted by Biot theory 118

5.6 Shear wave velocity predicted by Biot theory 119

5.7 Shear wave attenuation predicted by Biot theory 120

5.8 Measured velocity at 120 kHz and 400 kHz from core data taken at the buried array site with mean grain size. 122

5.9 Measured attenuation at 120 kHz and 400 kHz from core data taken at the buried array site with mean grain size 123

5.10 Measured minus predicted acoustic pressure levels in the sediment. 125

5.11 Biot theory minus the ARL-UT geoacoustic model predictions. 127

5.12 Plane wave transmission coefficient predicted by Biot theory and the ARL-UT geoacoustic model. 128

5.13 Comparison of attenuation in dB/m/kHz. 130

LIST OF TABLES

Table		Page
2.1	Material Properties for Three Marine Sediments	22
3.1	Geoacoustic Parameters for the Single-Phase Fluid Model	40
3.2	Geoacoustic Parameters for the Single-Phase Solid Model	42
5.1	ARL-UT Geoacoustic Model	114
5.2	Geophysical Inputs to Biot Theory	114

LIST OF SYMBOLS

Symbol	Units	Definition
a	cm	pore size parameter
$\mathbf{a}_1$	—	unit vector in the x direction
$\mathbf{a}_3$	—	unit vector in the z direction
C	dyne/cm^2	complex elastic modulus
c	—	structure factor
D	cm	total displacement field in the sediment
F	—	visco-dynamic function
$f(t)$		forcing function
G_2	—	ratio of displacement potential coefficient in the fluid to that in the frame for the Type II wave
G_p	—	ratio of displacement potential coefficient in the fluid to that in the frame for the Type I wave
G_s	—	ratio of displacement potential coefficient in the fluid to that in the frame for the shear wave
H	dyne/cm^2	complex elastic modulus
$H_o^{(2)}$	—	zero-order Hankel function of the second kind
h	m	source height
$\mathbf{I}$	—	identity matrix
k_o	1/cm	wavenumber in the fluid halfspace
k_1	1/cm	wavenumber for the compressional wave in a single phase medium
k_2	1/cm	wavenumber of the Type II wave
k_p	1/cm	wavenumber of the Type I wave
k_s	1/cm	wavenumber of the shear wave
k_x	1/cm	horizontal component of wavevector
k_z	1/cm	vertical component of wavevector

K_f	dyne/cm^2	fluid bulk modulus
K_m	dyne/cm^2	sediment frame bulk modulus
K_s	dyne/cm^2	sediment grain bulk modulus
M	dyne/cm^2	complex elastic modulus
p	N/m^2	acoustic fluctuation pressure
$\overline{\mathfrak{R}}$	—	plane wave reflection coefficient
s	cm	distance from image source to receiver for reflected path
s_2	cm	distance from image source to receiver for transmitted Type II path
s_p	cm	distance from image source to receiver for transmitted Type I path
s_s	cm	distance from image source to receiver for transmitted shear path
t	sec	time
$\overline{\tau_2}$	—	plane wave transmission coefficient for the Type II wave
$\overline{\tau_p}$	—	plane wave transmission coefficient for the Type I wave
$\overline{\tau_s}$	—	plane wave transmission coefficient for the shear wave
u	cm	absolute sediment frame displacement
U	cm	absolute interstitial fluid displacement
V_0	cm/sec	velocity of upper fluid halfspace
V_1	cm/sec	compressional velocity in sediment halfspace for single-phase model
V_2	cm/sec	velocity of Type II wave
V_p	cm/sec	velocity of Type I wave
V_s	cm/sec	velocity of shear wave
w	cm	relative displacement between fluid and frame
α	1/cm	vertical component of wavevector in fluid halfspace

α_2	1/cm	vertical component of wavevector for Type II wave
α_p	1/cm	vertical component of wavevector for Type I wave
α_s	1/cm	vertical component of wavevector for shear wave
β	—	porosity
$\delta(x)$	—	Dirac delta function
η	poise	fluid viscosity
χ	cm^2	permeability
λ	$dyne/cm^2$	Lame constant
μ	$dyne/cm^2$	shear modulus
ρ_o	g/cm^3	upper halfspace fluid density
ρ_1	g/cm^3	sediment density in single-phase sediment
ρ_b	g/cm^3	complex dynamic sediment density
ρ_f	g/cm^3	interstitial fluid density
ρ_s	g/cm^3	sediment grain density
ρ_T	g/cm^3	total static sediment density
τ	N/m^2	stress
ω	1/sec	radian frequency
∇	—	vector derivative operator
θ	radian	angle of incidence

Chapter 1
INTRODUCTION

An important problem in the field of underwater acoustics is the interaction of a sound field with the seafloor. The seafloor is an acoustically complex medium exhibiting properties that can be highly variable in both vertical and lateral extent. On a microscopic scale the seafloor is no less complicated; marine sediments manifest themselves as two- and sometimes three-phase materials with solid grains of variable dimension, shape, and composition randomly oriented and connected in space, the interstices being filled by seawater and dissolved gases.

1.1 Background

The modeling of wave propagation through the physically complex medium of the seafloor has progressed from treating the sediments as a lossy fluid, to a viscoelastic solid, to a poro-viscoelastic solid. The great bulk of modeling efforts of acoustic interaction with the seafloor in the ocean acoustics community have considered the seafloor sediments to be modelable as a fluid [e.g., Ingenito (1973), Ellis and Chapman (1980), Rubano (1980), Dicus and Anderson (1982), and Brocher (1983)]. The fluid model has been sufficient in fact to successfully predict various measures of a propagating acoustic field: most commonly transmission loss. Some of the experimental results [e.g., Ingenito and Wolf (1976), McDaniel and Beebe (1980), Chapman and Ellis (1984), Beebe and Holland (1986), Hughes et al. (1990)], however, indicated that the effect of the sediment rigidity could be significant for various environments. Modeling efforts [Fryer (1978), Vidmar (1980), Holland (1985)] that considered the sediments as viscoelastic attempted to determine the bounds of validity for the fluid approximation as a function of frequency and seafloor environment.

In the meantime a substantial effort was directed toward an even more rigorous accounting of the physics of propagation in marine sediments, using Biot theory (1956a, 1956b, 1962), which considered marine sediments as a poro-elastic solid. The theory predicts, in contrast to both the fluid model and the viscoelastic model (which will be referred to as single-phase models) a non-linear frequency dependence of wave attenuations and a compressional wave of the second kind (which will hereafter be referred to as the Type II wave) in addition to the classical compressional (Type I) and shear wave of geophysics.

The foundations of the Biot theory were laid by Rayleigh [Strutt (1883)] who considered propagation in a porous medium whose solid frame was rigid and whose interstices were circular cylinders. Later, Zwikker and Kosten (1949) developed the rigid frame theory further and began initial developments of a flexible frame theory. It was Biot, however, who provided the first comprehensive theory of wave propagation in fluid saturated porous media that accounted for both the losses due to the relative motion between the interstitial pore fluid and the solid frame and accounted for displacements in the solid frame.

In an exhaustive series of papers, Deresewicz and co-authors (1962-1964) used Biot theory to examine a number of seafloor interaction problems. Later, Stoll (1974) introduced the notion of complex frame moduli to account for viscoelastic effects and in a series of papers [Stoll (1977), Stoll (1979), Stoll (1980), Stoll and Kan (1981)] was largely responsible for bringing Biot theory to the attention of the underwater acoustics community. Thus, the poro-viscoelastic model (sometimes termed the Biot-Stoll model) considers loss mechanisms due to the relative motion between the fluid and frame as well as (approximately) constant Q effects such as the squeeze-film phenomena, frictional losses at grain-to-grain contacts, and relaxation phenomena associated with electrochemical effects. Yamamoto (1983a, 1983b) was also active in applying the theory to a number of

problems and generalized the form of the visco-dynamic operator to include a distribution of grain sizes [Yamamoto and Turgut (1988)].

Laboratory experiments have to date confirmed many aspects of the Biot theory including the frequency dependence of the Type I compressional velocity and attenuation [e.g., Hovem and Ingram (1979), Addison (1984), Winkler (1985)], the dependence of the Type I compressional wave velocity and attenuation on the properties of the interstitial pore fluid [e.g., Domenico (1977) and Costley (1986)], the frequency dependence of the shear wave attenuation [Brunson and Johnson (1980)] and the existence of the Type II wave [Paterson (1956) and Plona (1980)]. Actually, the existence of the Type II wave was well known in aeroacoustics and its properties had been measured in porous architectural materials such as foams and fibrous tiles. At-sea experiments [e.g., Ingenito (1973)] also have indicated that the frequency dependence of the Type I wave compressional wave attenuation is not always linear with frequency and Biot theory has been successfully employed in explaining such non-linearities [Beebe (1981)]. An excellent recent summary of the state of understanding of the frequency dependence of compressional wave attenuation in marine sediments and the evidence for a non-linear frequency dependence is given by Kibblewhite (1989).

1.2 Objective and Approach

The motivation for this work was to understand how the porous, two-phase nature of marine sediments influences reflection from and transmission through the seafloor since the majority of current models of seafloor interaction consider marine sediments to be a single-phase fluid or a single-phase solid. In order to focus on the effects of the two-phase poro-viscoelastic medium, a great many complexities in nature are ignored here, including interface roughness and slopes; velocity, attenuation, and density gradients; and macroscopic inhomogeneities.

The approach taken is to set up and solve a boundary value problem of a fluid (seawater) overlying a poro-viscoelastic halfspace (sediment) where the source is in the upper medium. For simplicity the source is chosen to be a line source such that the problem can be solved in two dimensions. The linearized wave equation is employed in the upper halfspace and the equations of motion for a poro-viscoelastic medium derived by Biot are employed for the sediment. The form of the Biot theory in this work largely follows Stoll (1974). The effects arising from the two-phase nature of the sediments in the reflection/transmission problem are isolated by a comparison with commensurate results from the single-phase models. The comparison of reflection and transmission between the single phase models and the poro-viscoelastic model is performed for three sediment types: a silty clay, a carbonate sand, and a sandstone. These sediment types were chosen as representative of common sediment types and because they represent distinct relationships between the ratio of their velocities to that of the overlying bottom water. For the silty clay, the Type I and shear wave velocity are both less than that of the upper halfspace; for the carbonate sand, the Type I wave velocity is greater and the shear velocity less than that of the upper halfspace; and for the sandstone, the Type I wave and shear velocity are both greater than that of the upper halfspace. The Type II velocity is less than that of the upper halfspace for all sediment types.

In Chapter 2, the time harmonic equations of motion are written for both media and Fourier transformed into wavenumber space. The dispersion relations for the poro-viscoelastic medium are obtained and examples of the frequency dependent velocities and attenuations for the three sediment types are shown. The boundary conditions are then applied, resulting in a set of simultaneous equations that can be solved for the plane wave reflection and transmission coefficients. In Chapter 3, the reflection coefficients from a poro-viscoelastic halfspace, a viscoelastic halfspace, and a fluid halfspace are compared in frequency and angle space for the three kinds of sediments. Differences in the reflectivity between models is noted and observations are made regarding the effect of using one model

or another in acoustic modeling. Several approximate models are also examined. The secular equation is derived and surface wave speeds and attenuations are obtained and compared with predictions from the single-phase viscoelastic solid sediment model. In Chapter 4, the inverse transform is applied using a combination of techniques to obtain the contribution from each wave type (i.e., direct path, geometrical reflected/transmitted ray, head wave, surface wave) and the results are compared with the "exact" solution (obtained by numerical integration) and with the solution obtained by a Fast Fourier Transform. The decomposition of the field into discrete wave types allows identification of dominant path contributions that arise in specific source/receiver geometries. In Chapter 5, recent anomalous experimental data of acoustic transmission through a water-sand interface are examined using Biot theory to determine whether the anomalies are attributable to effects predicted by Biot theory. A summary and conclusions of this work are given in Chapter 6.

Chapter 2

THEORY I - FORWARD TRANSFORM

In this chapter the equations of motion are given for each medium and transformed to the frequency domain, the boundary conditions are stated and a set of simultaneous equations are written to obtain the reflection and transmission coefficients.

2.1 The Fluid

The linearized equation of motion for an ideal fluid with a line source perpendicular to the x-z plane can be written:

$$\nabla^2 p - \frac{1}{V_o^2}\frac{\partial^2 p}{\partial t^2} = \rho_o\,\delta(x)\,\delta(z-h)\,\frac{\partial^2}{\partial t^2}\,f(t) \qquad (2.1)$$

where:

p	is the dynamic acoustic fluctuation pressure
V_o	is the acoustic wave speed
ρ_o	is the static density
$f(t)$	is the forcing function

and the (line) source is located at x=0, z=h. Letting f(t) be a unit time harmonic function, $f(t) = e^{i\omega t}$, equation (2.1) becomes

$$\nabla^2 p + k_o^2 p = -\omega^2 \rho_o\,\delta(x)\,\delta(z-h) \;;\quad k_o = \frac{\omega}{V_o} \qquad (2.2)$$

where the harmonic time dependence has been suppressed. Defining a Fourier Transform on the x variable:

$$\hat{p}(k_x,z) = \int_{-\infty}^{\infty} p(x,z)e^{ik_x x}dx$$

$$p(x,z) = \frac{1}{2\pi}\int_{-\infty}^{\infty} \hat{p}(k_x,z)e^{-ik_x x}dk_x \qquad (2.3)$$

then

$$\frac{\partial^2 \hat{p}}{\partial z^2} + \hat{p}\ (k_o^2 - k_x^2) = -\omega^2 \rho_o \delta\ (z-h) \tag{2.4}$$

which admits a homogeneous solution of the form

$$\hat{p}(k_x, z) = A_1 e^{-i(k_o^2 - k_x^2)^{1/2} z} + B_1 e^{i(k_o^2 - k_x^2)^{1/2} z} \tag{2.5}$$

The particular solution is obtained by a Fourier Transform on the z variable;

$$\hat{\hat{p}}(k_x, k_z)(k_o^2 - k_x^2 - k_z^2) = -\omega^2 \rho_o e^{ik_z h} \tag{2.6}$$

and

$$\hat{p}\ (k_x, z) = \frac{\omega^2 \rho_o}{2\pi} \int_{-\infty}^{\infty} \frac{e^{-ik_z(z-h)}}{k_z^2 + k_x^2 - k_o^2}\ dk_z\ . \tag{2.7}$$

The integrand has simple poles at

$$k_{z_o} = \pm\ (k_o^2 - k_x^2)^{1/2} \tag{2.8}$$

Taking the case (z-h) < 0 first and closing the contour in the upper half plane

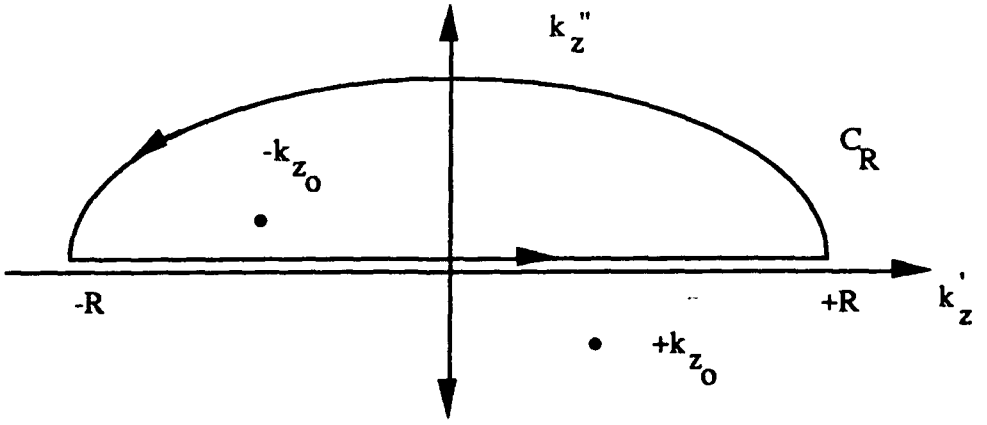

Figure 2.1 Path of integration in the complex k_z plane for (z-h) < 0

we have from the Residue Theorem that

$$\int_{-R}^{R} \frac{e^{-ik_z(z-h)}}{k_z^2+k_x^2-k_o^2}\,dk_z + \int_{C_R} \frac{e^{-ik_z(z-h)}}{k_z^2+k_x^2-k_o^2}\,dk_z = 2\pi i \,\mathrm{res}\left(-k_{z_o}\right) \tag{2.9}$$

where

$$\mathrm{res}\left(-k_{z_o}\right) = \left.\frac{e^{ik_z(z-h)}}{\left(k_z-k_{z_o}\right)}\right|_{-k_{z_o}} = \frac{e^{-i\left(k_o^2-k_x^2\right)^{1/2}(z-h)}}{-2\left(k_o^2-k_x^2\right)^{1/2}} \tag{2.10}$$

To make the integral on C_R vanish as $R\rightarrow\infty$; we require that Im $\{k_z\} > 0$ or, Im$\{(k_o^2 - k_x^2)^{1/2}\} < 0$; then

$$\hat{p}(k_x, z<h) = -\frac{i\omega^2\rho_o}{2}\frac{e^{-i(k_o^2-k_x^2)^{1/2}(z-h)}}{(k_o^2-k_x^2)^{1/2}} \tag{2.11}$$

For (z-h) > 0: we close the contour in the lower half plane

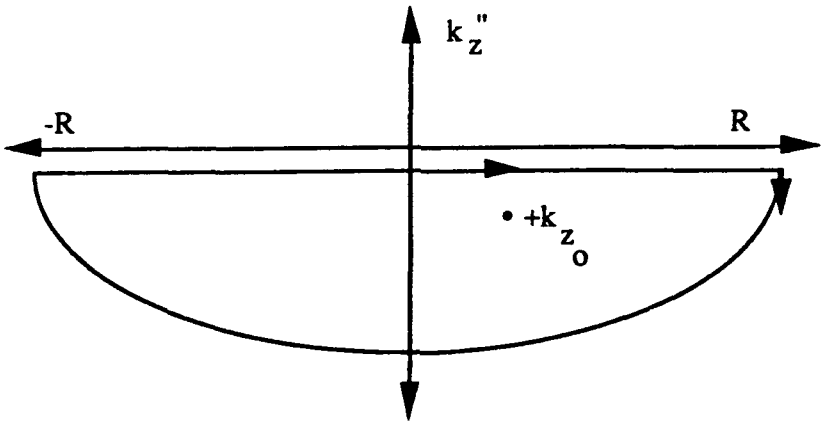

Figure 2.2 Path of integration in the complex k_z plane for (z-h) > 0

and from the Residue Theorem

$$\int_{-R}^{R} \frac{e^{-ik_z(z-h)}}{k_z^2+k_x^2-k_o^2}\,dk_z + \int_{C_R} \frac{e^{-ik_z(z-h)}}{k_z^2+k_x^2-k_o^2}\,dk_z = -2\pi i \,\mathrm{res}\left(+k_{z_o}\right) \tag{2.12}$$

$$\mathrm{res}\left(+k_{z_o}\right) = \frac{e^{-i\left(k_o^2-k_x^2\right)^{1/2}(z-h)}}{2\left(k_o^2-k_x^2\right)^{1/2}} \tag{2.13}$$

Note that the minus sign on the RHS of Eq. (2.12) follows from Cauchy's law closing the contour clockwise. To make the integral on C_R vanish as $R\to 0$ we require that $\mathrm{Im}\{kz\}<0$ or $\mathrm{Im}\ \{(k_o^2 - k_x^2)^{1/2}\}<0$, then

$$\hat{p}(k_x, z\geq h) = -\frac{i\omega^2\rho_o}{2}\frac{e^{-i(k_o^2-k_x^2)^{1/2}(z-h)}}{(k_o^2-k_x^2)^{1/2}} \tag{2.14}$$

and for all z (combining Eq. (2.11) and Eq. (2.14))

$$\hat{p}(k_x, z) = -\frac{i\omega^2\rho_o}{2}\frac{e^{-i(k_o^2-k_x^2)^{1/2}|z-h|}}{(k_o^2-k_x^2)^{1/2}} \tag{2.15}$$

The total solution is the sum of the homogeneous and the particular solution. The radiation condition, however, requires that Im $\{(k_o^2 - k_x^2)^{1/2}\} < 0$ so that $B_1 = 0$, and the full solution is

$$\hat{p}(k_x, z) = A_1 e^{-i(k_o^2 - k_x^2)^{1/2} z} - \frac{i\omega^2 \rho_o}{2} \frac{e^{-i(k_o^2 - k_x^2)^{1/2}|z-h|}}{(k_o^2 - k_x^2)^{1/2}} \quad . \tag{2.16}$$

Now let

$$A_1 = \Re \left[\frac{-i\rho_o \omega^2}{2(k_o^2 - k_x^2)^{1/2}} \right]$$

where $\Re$ can be thought of as a reflection factor for the amplitude of the velocity potential, then

$$\hat{p}(k_x, z) = -\frac{i\omega^2 \rho_o}{2(k_o^2 - k_x^2)^{1/2}} \left[\Re e^{-i(k_o^2 - k_x^2)^{1/2} z} + e^{-i(k_o^2 - k_x^2)^{1/2}|z-h|} \right] \quad . \tag{2.17}$$

The boundary conditions will require an expression for the field in terms of the displacement vector U_o where the subscript denotes the upper medium. From Eulers equation

$$-\nabla p = \rho_o \frac{\partial^2 U_o}{\partial t^2} \quad . \tag{2.18}$$

Since we are assuming a time harmonic field ($e^{i\omega t}$)

$$\nabla p = \rho_o \omega^2 U_o \tag{2.19}$$

and transforming Euler's equation, we get

$$-a_1 i k_x \hat{p} + a_3 \frac{\partial \hat{p}}{\partial z} = \rho_o \omega^2 \hat{U}_o \tag{2.20}$$

where a_1, a_3 are the x and z unit vectors respectively. Letting $\alpha = (k_o^2 - k_x^2)^{1/2}$,

$$\hat{U}_o(k_x, z) = \frac{1}{\rho_o \omega^2}\left\{-a_1 i k_x \left(\frac{-i\rho_o \omega^2}{2\alpha}\right)\left[\Re e^{-i\alpha z} + e^{-i\alpha|z-h|}\right] + a_3\left(\frac{-i\rho_o \omega^2}{2\alpha}\right)\left[\Re(-i\alpha)e^{-i\alpha z} \pm (-i\alpha)e^{-i\alpha|z-h|}\right]\right\} \tag{2.21}$$

Note that $$\frac{\partial}{\partial z} e^{-i\alpha|z-h|} = -i\alpha e^{-i\alpha|z-h|}\left(\frac{\partial}{\partial z}|z-h|\right)$$

and

$$\frac{\partial}{\partial z}|z-h| = \begin{cases} +1 \text{ for } z > h \\ -1 \text{ for } z < h \end{cases}$$

For the last term of Eq. (2.21) the minus sign is chosen because we want to use this expression for the boundary conditions (where z = 0) so that

$$\hat{U}_o(k_x, z < h) = \frac{-1}{2\alpha}\left\{a_1 k_x\left[\Re e^{-i\alpha z} + e^{-i\alpha|z-h|}\right] + a_3\alpha\left[\Re e^{-i\alpha z} - e^{-i\alpha|z-h|}\right]\right\} \tag{2.22}$$

2.2 The Poro-viscoelastic Halfspace

2.2.1 Equation of Motion

In this section the equations of motion for a poro-viscoelastic medium are derived, the dispersion relation is found and the Fourier transformed displacement vectors for the motion of the sediment frame and the relative motion between the frame and the interstitial fluid are obtained.

The equations of motion are obtained by specifying both the constitutive equations (relating the internal restoring forces of the medium to the corresponding deformations) and the force balance equations which come from Newton's second law. For the two-phase material under consideration each kind of conservation law is expressed by two equations; one for the solid component and one for the fluid component.

For the constitutive equations, generalized Hooke's law for an isotropic porous medium yields in dyadic notation

$$\boldsymbol{\tau} = \mathbf{I}\,\{\lambda(\nabla\cdot\mathbf{u}) - C\,(\nabla\cdot\mathbf{w})\} + \mu\,(\nabla\,\mathbf{u} + \mathbf{u}\,\nabla) \tag{2.23}$$

where $\boldsymbol{\tau}$ is the stress, $\mathbf{I}$ is the identity matrix, λ and μ are the Lame' constants, $\mathbf{u}$ is the absolute displacement of the solid frame, $\mathbf{w}$ is the relative displacement of the two phases

$$\mathbf{w} = \beta\,(\mathbf{u} - \mathbf{U}) \tag{2.24}$$

$\mathbf{U}$ is the absolute displacement of the fluid, β is the material porosity, and C is an operator that characterizes the elastic and inelastic response of the sediment frame (see Appendix A). Without the term $C(\nabla\cdot\mathbf{w})$, Eq. (2.23) reduces to the constitutive equation for an isotropic elastic solid. The constitutive equation for the fluid is:

$$p_f = M(\nabla\cdot\mathbf{w}) - C(\nabla\cdot\mathbf{u}) \tag{2.25}$$

where p_f is the pressure in the interstitial fluid and M is an operator of the same form described for C. Eq. (2.25) has the same form as the equation of continuity for an isotropic fluid.

The force balance equations likewise resemble their isotropic counterparts,

$$\nabla \cdot \tau = \frac{\partial^2}{\partial t^2} \left[\rho_T \mathbf{u} - \rho_f \mathbf{w} \right] \tag{2.26}$$

$$-\nabla p = \frac{\partial^2}{\partial t^2} \left[\rho_f \mathbf{u} - \rho_b \mathbf{w} \right] \tag{2.27}$$

where

ρ_T = the total static density of the medium
ρ_f = the density of the interstitial fluid
ρ_b = the complex density

The total static density of the medium can be obtained by a simple material average, i.e.

$$\rho_T = \rho_f \beta + \rho_s (1 - \beta) \tag{2.28}$$

where ρ_s is the density of the solid grains. The complex density was derived by Biot (1962) as

$$\rho_b = c \frac{\rho_f}{\beta} - i\omega \frac{\eta}{\chi} F(\gamma) \tag{2.29}$$

The first term accounts for the fact that since the pore space is tortuous not all the fluid moves in the direction of the applied pressure gradient. The parameter c is equal to one where the pores are aligned in the direction of the pressure gradient and greater than one for randomly ordered pore geometries characteristic of sediment interstices. The second term accounts for viscous drag caused by fluid viscosity η scaled by the permeability χ. The

function $F(\gamma)$ was derived originally by Zwikker and Kosten (1949) to account for the transition between Poiseuille flow at low frequencies and Helmholtz flow at high frequencies. The function is defined as:

$$F(\gamma) = \frac{1}{4} \frac{\gamma T(\gamma)}{1-2T(\gamma)/\gamma} \tag{2.30}$$

where

$$T(\gamma) = \frac{\mathrm{ber}'(\gamma) + i\,\mathrm{bei}'(\gamma)}{\mathrm{ber}(\gamma) + i\,\mathrm{bei}'(\gamma)} \tag{2.31}$$

and

$$\gamma = a\,(\omega\rho_f/\eta)^{1/2} \tag{2.32}$$

and a is a parameter with the dimension of length that depends on the size and shape of the pores.

Now, substituting the constitutive equations into the force balance equations

$$\nabla \cdot \boldsymbol{\tau} = \nabla \left\{ \lambda\, (\nabla \cdot \mathbf{u}) - C(\nabla \cdot \mathbf{w}) \right\} + \mu \nabla^2 \mathbf{u} + \mu \nabla \cdot (\mathbf{u} \nabla) \tag{2.33}$$

and since

$$\nabla \cdot (\mathbf{u} \nabla) = \nabla\, (\nabla \cdot \mathbf{u}) \tag{2.34}$$

$$\nabla \cdot \boldsymbol{\tau} = (H - \mu)\, \nabla\, (\nabla \cdot \mathbf{u}) - C \nabla (\nabla \cdot \mathbf{w}) + \mu \nabla^2 \mathbf{u} = -\omega^2 \left[\rho_T \mathbf{u} - \rho_f \mathbf{w} \right] \tag{2.35}$$

and

$$\nabla p = C \nabla (\nabla \cdot \mathbf{u}) - M \nabla (\nabla \cdot \mathbf{w}) = -\omega^2 \left[\rho_f \mathbf{u} - \rho_b \mathbf{w} \right] \tag{2.36}$$

where $H = \lambda + 2\mu$.

We wish to express the equations in terms of potentials, and performing the usual Helmholtz decomposition, let

$$\mathbf{u} = \nabla\phi_s + \nabla\times\psi_s \quad ; \quad \nabla\cdot\psi_s = 0 \tag{2.37}$$

$$\mathbf{w} = \nabla\phi_f + \nabla\times\psi_f \quad ; \quad \nabla\cdot\psi_f = 0$$

then

$$(H-\mu)\,\nabla(\nabla^2\phi_s) - C\nabla(\nabla^2\phi_f) + \mu\,\nabla^2(\nabla\phi_s + \nabla\times\psi_s) = \tag{2.38}$$

$$-\omega^2\left[\rho_T(\nabla\phi_s + \nabla\times\psi_s) - \rho_f(\nabla\phi_f + \nabla\times\psi_f)\right]$$

$$C\nabla(\nabla^2\phi_s) - M\nabla(\nabla^2\phi_f) = -\omega^2\left[\rho_f(\nabla\phi_s + \nabla\times\psi_s) - \rho_f(\nabla\phi_f + \nabla\times\psi_f)\right] \tag{2.39}$$

The irrotational field can be obtained by taking the divergence of Eqs. (2.38, 2.39), i.e.

$$H\nabla^2\phi_s - C\nabla^2\phi_f = -\omega^2\left[\rho_T\phi_s - \rho_f\phi_f\right] \tag{2.40}$$

$$C\nabla^2\phi_s - M\nabla^2\phi_f = -\omega^2\left[\rho_f\phi_s - \rho_b\phi_f\right] \tag{2.41}$$

and the rotational component of the field can be obtained by taking the curl of Eqs. (2.38, 2.39)

$$\mu\,\nabla^2\psi_s = -\omega^2\left[\rho_T\psi_s - \rho_f\psi_f\right] \tag{2.42}$$

$$\rho_f\psi_s = \rho_b\psi_f = \left[c\,\frac{\rho_f}{\beta} - \frac{i}{\omega}\,\frac{\eta}{\chi}\,F(\gamma)\right]\psi_f \tag{2.43}$$

The equations for the irrotational component of the field allow solutions of the form

$$\phi_s(\mathbf{r}) = Ae^{-i(\mathbf{q}\cdot\mathbf{r})} \tag{2.44}$$

$$\phi_f(\mathbf{r}) = Be^{-i(\mathbf{q}\cdot\mathbf{r})}$$

where $\mathbf{q}\cdot\mathbf{q} = k^2$

and plugging them into Eqs. (2.40, 2.41) we obtain the dispersion relation

$$\begin{bmatrix} -k^2H + \omega^2 \rho_T & k^2C - \omega^2 \rho_f \\ -k^2C + \omega^2 \rho_f & k^2M - \omega^2 \rho_b \end{bmatrix} = 0 \qquad (2.45)$$

or in terms of the velocity $V=\omega/k$ we have

$$V^4 (\rho_f^2 - \rho_T\rho_b) + V^2 \left[\rho_bH + \rho_TM - 2\rho_fC\right] + C^2 - HM = 0 \qquad (2.46)$$

There are two solutions to Eq.(2.46) corresponding to two dilatational waves (Type I and Type II) that can propagate in porous media. The Type I wave is the wave of classical geophysics with wave speeds on the order of .95 - 1.3 times the speed of the interstitial fluid speed for unconsolidated marine sediments. Henceforth the subscript to designate this wave type will be "p" as a reminder that it is the classical p-wave. The Type II wave is diffusive (that is the imaginary part of the wavenumber is not small compared with the real part) at low frequencies for water saturated sediments and propagatory at high frequencies. For this wave type the interstitial fluid and the sediment move essentially out of phase. The subscript designating this wave type will be "2". The subscript for the shear wave will be "s". Thus, the velocities for the Type I, Type II and shear wave will be V_p, V_2 and V_s respectively. Rewriting the potentials

$$\phi_s (\mathbf{r}) = A_p e^{-i(\mathbf{q}_p \cdot \mathbf{r})} + A_2 e^{-i(\mathbf{q}_2 \cdot \mathbf{r})} \qquad (2.47)$$

$$\phi_f (\mathbf{r}) = B_p e^{-i(\mathbf{q}_p \cdot \mathbf{r})} + B_2 e^{-i(\mathbf{q}_2 \cdot \mathbf{r})}$$

we can solve for the ratio of coefficients between the two potentials using Eq. (2.45).

$$Gp \equiv \frac{B_p}{A_p} = \frac{H/V_p^2 - \rho_T}{C/V_p^2 - \rho_f} \tag{2.48}$$

$$G_2 \equiv \frac{B_2}{A_2} = \frac{H/V_2^2 - \rho_T}{C/V_2^2 - \rho_f} \tag{2.49}$$

The dispersion relation for the rotational component of the field may be had by assuming solutions of the form

$$\psi_s = De^{-i(q\cdot r)} \tag{2.50}$$

$$\psi_f = Ee^{-i(q\cdot r)}$$

so that Eqs. (2.42, 2.43) yield

$$\begin{bmatrix} -k^2\mu + \omega^2 \rho_T & -\omega^2 \rho_f \\ \rho_f & \rho_b \end{bmatrix} = 0 \quad . \tag{2.51}$$

The shear velocity $V_s = \omega/k$ is :

$$V_S = \left[\frac{\mu}{\rho_T - \rho_f^2/\rho_b}\right]^{1/2} \tag{2.52}$$

and

$$G_s = \frac{E}{D} = \frac{\mu/V_s^2 - \rho_T}{\rho_f} \tag{2.53}$$

We can write the transformed displacement potentials now, letting the q_i have z components only

$$q_i = -a_3 (k_i^2 - k_x^2)^{1/2} = -a_3 \alpha_i \qquad i = p, 2, s \tag{2.54}$$

for i = Type I, II, and shear waves. The x component of the wave vector is the same in both the fluid and porous solid (Snell's law) and we choose α_i to be negative for waves traveling in the negative z direction (away from the boundary), so that

$$\phi_s = A_p e^{i\alpha_p z} + A_2 e^{i\alpha_2 z}$$

$$\phi_f = A_p G_p e^{i\alpha_p z} + A_2 G_2 e^{i\alpha_2 z} \tag{2.55}$$

$$\psi_s = a_2 D e^{i\alpha_s z}$$

$$\psi_f = a_2 D G_s e^{i\alpha_s z}$$

Recalling Eq. (2.37), then

$$u(x,y) = a_1 \frac{\partial \phi_s}{\partial x} + a_3 \frac{\partial \phi_s}{\partial z} + a_3 \frac{\partial \psi_s}{\partial x} - a_1 \frac{\partial \psi_s}{\partial z} \tag{2.56}$$

$$w(x,y) = a_1 \frac{\partial \phi_f}{\partial x} + a_3 \frac{\partial \phi_f}{\partial z} + a_3 \frac{\partial \psi_f}{\partial x} - a_1 \frac{\partial \psi_f}{\partial z} \tag{2.57}$$

and from our definition of the Fourier Transform [Eq. (2.3)]

$$\hat{u} = a_1\left(-ik_x\hat{\phi}_s - \frac{\partial \hat{\psi}_s}{\partial z}\right) + a_3\left(-ik_x\hat{\psi}_s + \frac{\partial \hat{\phi}_s}{\partial z}\right) \tag{2.58}$$

$$\hat{w} = a_1\left(-ik_x\hat{\phi}_f - \frac{\partial \hat{\psi}_f}{\partial z}\right) + a_3\left(-ik_x\hat{\psi}_f + \frac{\partial \hat{\phi}_f}{\partial z}\right) \tag{2.59}$$

so that

$$\hat{u} = -i\left[a_1\left\{k_x A_p e^{i\alpha_p z} + k_x A_2 e^{i\alpha_2 z} + \alpha_s D e^{i\alpha_s z}\right\} + a_3\left\{-\alpha_p A_p e^{i\alpha_p z} - \alpha_2 A_2 e^{i\alpha_2 z} + k_x D e^{i\alpha_s z}\right\}\right] \tag{2.60}$$

$$\hat{w}=-i\left[a_1\left\{k_x G_p A_p e^{i\alpha_p z}+k_x G_2 A_2 e^{i\alpha_2 z}+\alpha_s G_s D e^{i\alpha_s z}\right\}+\right.$$
$$\left.a_3\left\{-\alpha_p G_p A_p e^{i\alpha_p z}-\alpha_2 G_2 A_2 e^{i\alpha_2 z}+k_x G_s D e^{i\alpha_s z}\right\}\right] \qquad (2.61)$$

Redefining the constants such that the coefficients correspond with those for the displacement field in the upper medium, we have

$$-i\,A_p=\mathcal{T}_p\ \frac{-1}{2\alpha} \qquad (2.62)$$

$$-i\,A_2=\mathcal{T}_2\ \frac{-1}{2\alpha} \qquad (2.63)$$

$$-i\,D=\mathcal{T}_s\ \frac{-1}{2\alpha} \qquad (2.64)$$

where $\mathcal{T}_p$, $\mathcal{T}_2$, and $\mathcal{T}_s$ are the displacement potential transmission factors for the Type I, Type II and shear waves, respectively. The displacements in the porous medium can then be written

$$\hat{u}(k_x,z)=\frac{-1}{2\alpha}\left[a_1\left\{k_x\mathcal{T}_p e^{i\alpha_p z}+k_x\mathcal{T}_2 e^{i\alpha_2 z}+\alpha_s\mathcal{T}_s e^{i\alpha_s z}\right\}+\right.$$
$$\left.a_3\left\{-\alpha_p\mathcal{T}_p e^{i\alpha_p z}-\alpha_2\mathcal{T}_2 e^{i\alpha_2 z}+k_x\mathcal{T}_s e^{i\alpha_s z}\right\}\right] \qquad (2.65)$$

$$\hat{w}(k_x,z)=\frac{-1}{2\alpha}\left[a_1\left\{k_x\mathcal{T}_p G_p e^{i\alpha_p z}+k_x\mathcal{T}_2 G_2 e^{i\alpha_2 z}+\alpha_s\mathcal{T}_s G_s e^{i\alpha_s z}\right\}+\right.$$
$$\left.a_3\left\{-\alpha_p\mathcal{T}_p G_p e^{i\alpha_p z}-\alpha_2\mathcal{T}_2 G_2 e^{i\alpha_2 z}+k_x\mathcal{T}_s G_s e^{i\alpha_s z}\right\}\right] \qquad (2.66)$$

2.2.2 Wave Velocities and Attenuations

In this section we plot Eq. (2.46 and 2.52) to demonstrate the velocity dependence of the Type I, Type II, and shear wave on frequency and sediment type. Three sediment types are represented: 1) an unconsolidated sand, 2) an unconsolidated clay, and 3) a consolidated sandstone. The material properties for each sediment, required by Biot theory, are given in Table 2.1.

Figures 2.3 and 2.4 show the frequency dependence of the phase velocities for a marine sand. Material properties in Table 2.1 and were derived from measurements on a shallow-water carbonate sand [Badiey et al. (1988)]. The Type I wave (the classical wave type in geophysics) is propagatory at all frequencies and shows a phase velocity dispersion of roughly 5% over this frequency range. The Type II wave is a diffusive wave at low frequencies and becomes propagatory at nigh frequencies with a phase velocity about one-tenth of that for the Type I wave. The velocity of the Type II wave in the kiloHertz region for this set of parameters happens to be close to that measured by Paterson (1956) (approximately 115 m/s) on a fully saturated beach sand at low confining pressures. The shear wave velocity predicted by Biot theory is only slightly dispersive.

Figures 2.5 - 2.7 show the attenuation (scaled by frequency) as a function of frequency. A common assumption in marine sediment acoustics is that the attenuation is linearly proportional to frequency (or that the attenuation scaled by frequency is constant). The Biot theory predicts a non-linear frequency dependence of attenuation due to the relative motion between the solid matrix and the interstitial fluid. At low frequency the oscillating fluid obeys Poiseuille flow where the velocity distribution across a (cylindrical) pore is parabolic, with zero velocity at the pore wall and a maximum velocity on the axis of the pore. At high frequency, the fluid obeys Helmholtz flow where the fluid inertia causes

Table 2.1 Material Properties for Three Marine Sediments

Property	Units	Sand	Silty-Clay	Sandstone
Fluid density, (ρ_o)	g/cm^3	1.024	1.024	1.024
Fluid bulk modulus, (K_f)	dyne/cm^2	2.38 10^{10}	2.38 10^{10}	2.38 10^{10}
Fluid viscosity, (η)	poise	.0101	.0101	.0101
Grain density, (ρ_s)	g/cm^3	2.85	2.68	2.65
Grain bulk modulus, (K_s)	dyne/cm^2	4.0 10^{11}	3.5 10^{11}	3.7 10^{11}
Porosity, (β)	---	.487	.68	.203
Permeability, (κ)	cm^2	4.26 10^{-7}	5.2 10^{-10}	1.07 10^{-7}
Structure factor, (c)	---	1.75	3.0	2.0
Pore size, (a)	cm	4.18 10^{-3}	1.25 10^{-4}	2.5 10^{-4}
Frame bulk modulus (K_m)	dyne/cm^2	3.33 10^8+	3.67 10^7+ i6.67 10^6	8.32 10^{10}+ i1.2 10^6
Frame shear bulk modulus (μ)	dyne/cm^2	2.5 10^8+ i3.75 10^6	7.86 10^6+ i2.5 10^5	8.53 10^{10}+ i4.25 10^8

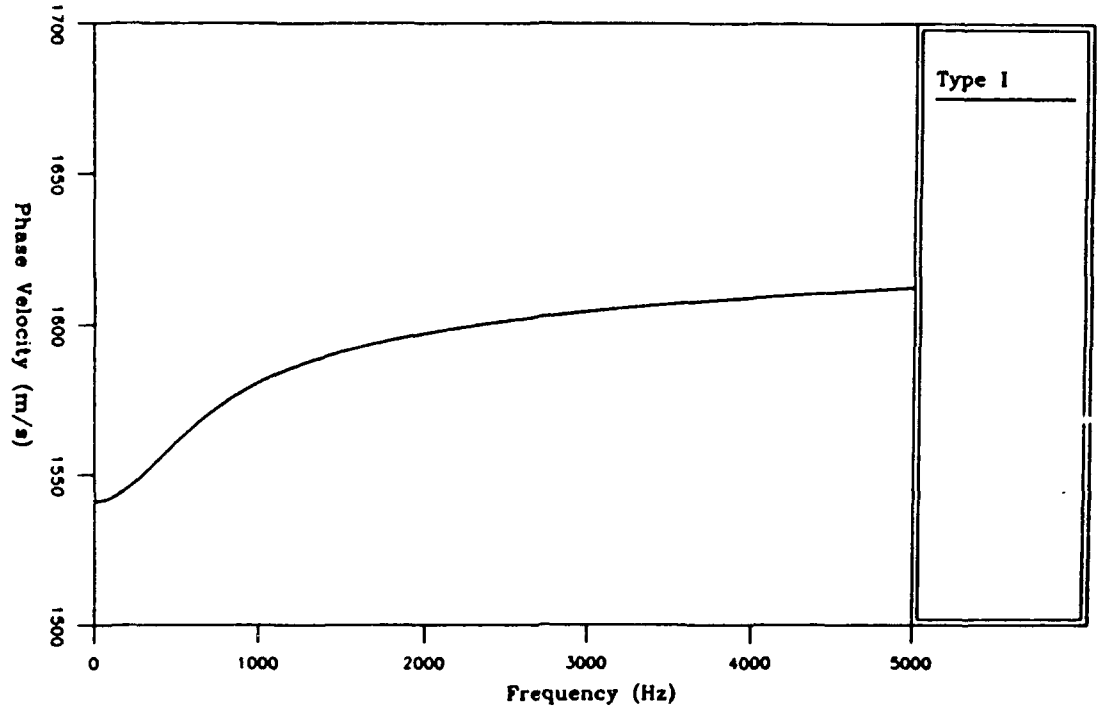

Figure 2.3 Type I wave phase velocity for carbonate sand

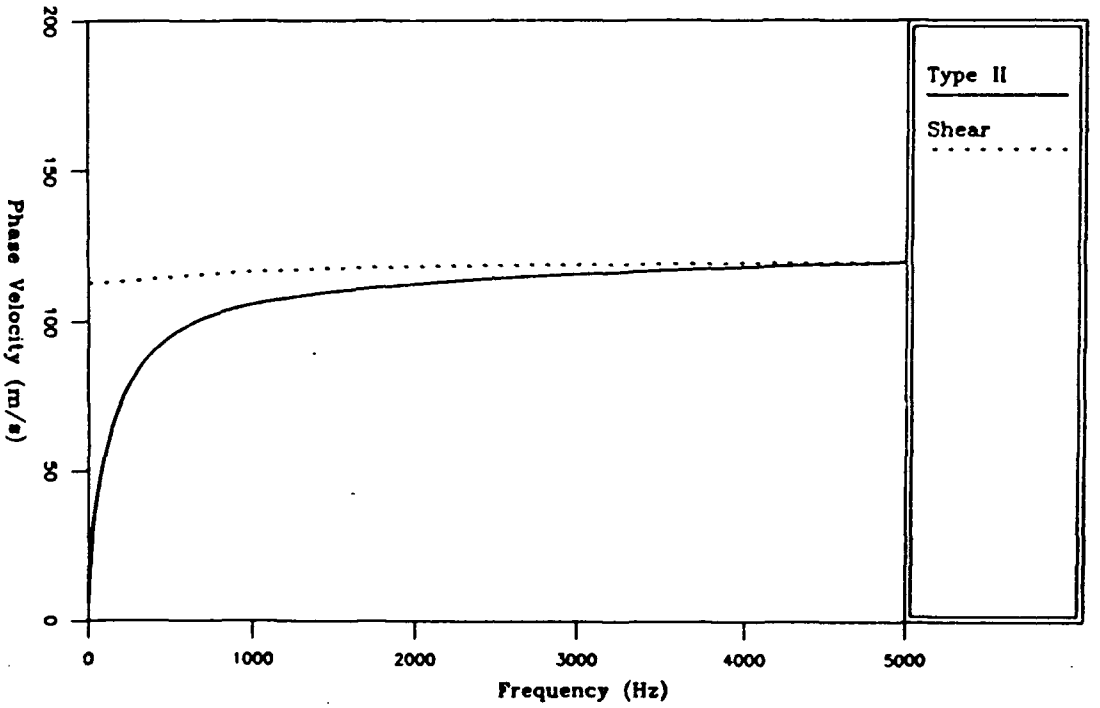

Figure 2.4 Type II and shear wave phase velocity for carbonate sand

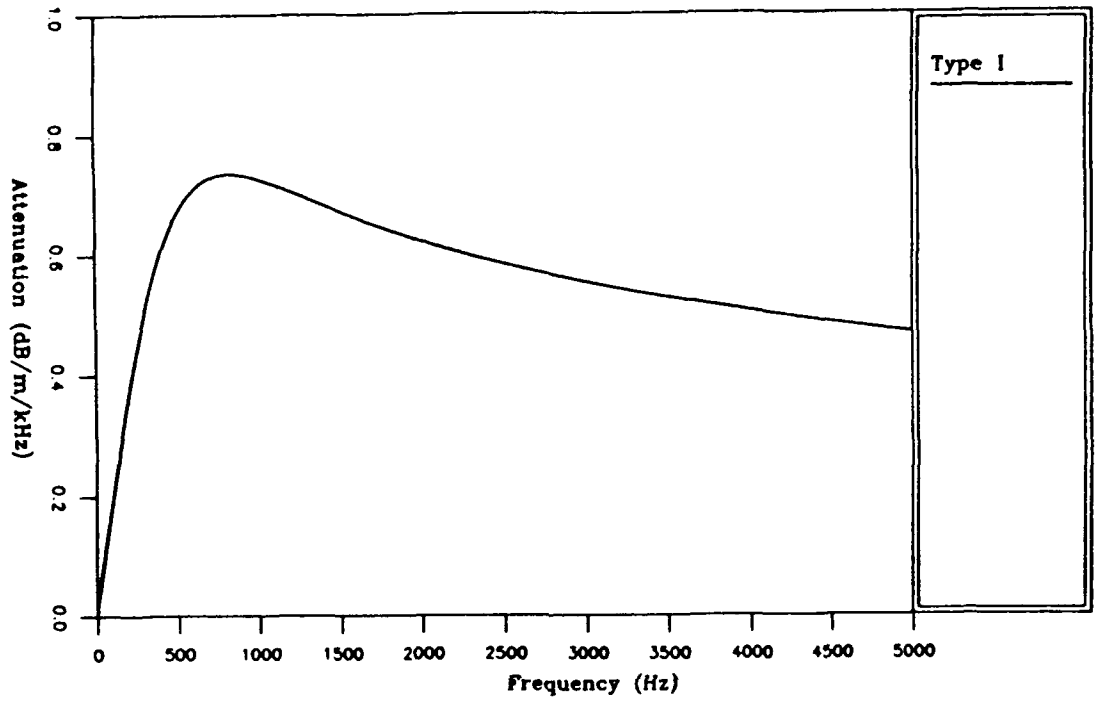

Figure 2.5 Type I wave attenuation for carbonate sand

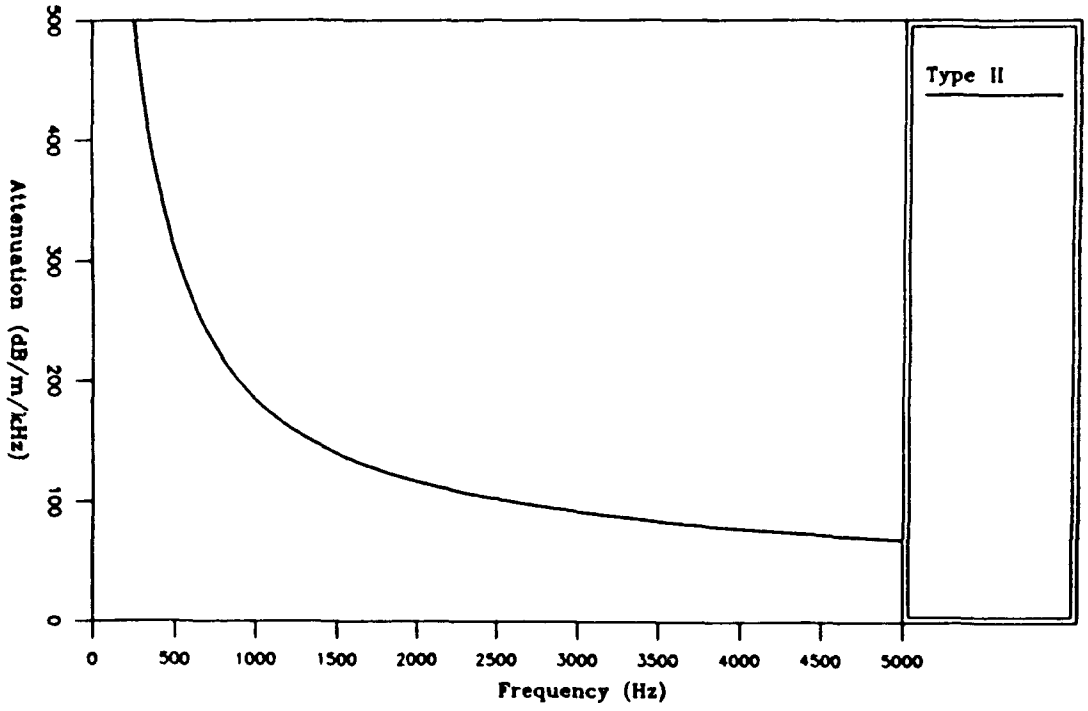

Figure 2.6 Type II wave attenuation for carbonate sand

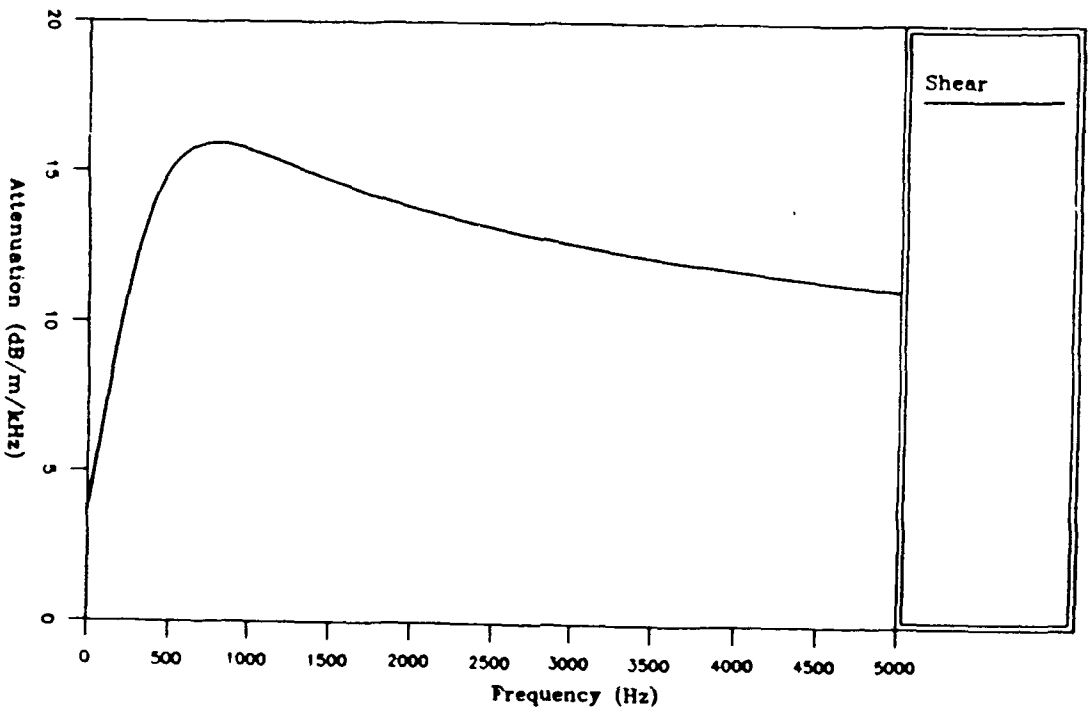

Figure 2.7 Shear wave attenuation for carbonate sand

the velocity distribution to be nearly flat across the diameter of the pore with an infinitesimal boundary layer at the pore wall. The frequency separating these two regimes is termed the critical frequency and is defined by

$$f_c = \frac{1}{5\pi} \frac{\eta\beta}{\chi} . \tag{2.67}$$

It is clear from Figures 2.5 - 2.7 that only far below or above the critical frequency (735 Hz) is the attenuation linearly dependent on frequency for porous media.

Figures 2.8 through 2.14 show the frequency dependence of velocities and attenuations for a marine clay and sandstone. The influence of the velocity and attenuation dispersion shown in these figures on seafloor reflection will be probed in detail in Chapter III. Material properties for these sediments are given in Table 2.1; the silty clay properties were taken from Holland and Brunson (1988) and the properties of the sandstone were taken from Winkler (1985).

2.3 Application of the Boundary Conditions

There are four boundary conditions [Deresewiecz and Skalak (1963)] specified at the interface between a fluid and a poro-viscoelastic solid:

1) continuity of normal fluid displacement

$$\hat{n} \cdot \mathbf{U_0} = \hat{n} \cdot \mathbf{u} - \hat{n} \cdot \mathbf{w} \qquad ; z = 0$$

2) continuity of normal traction

$$H(\nabla \cdot \mathbf{u}) - C(\nabla \cdot \mathbf{w}) - 2\mu \frac{\partial u_x}{\partial x} = -p \quad ; \quad z = 0 \tag{2.68}$$

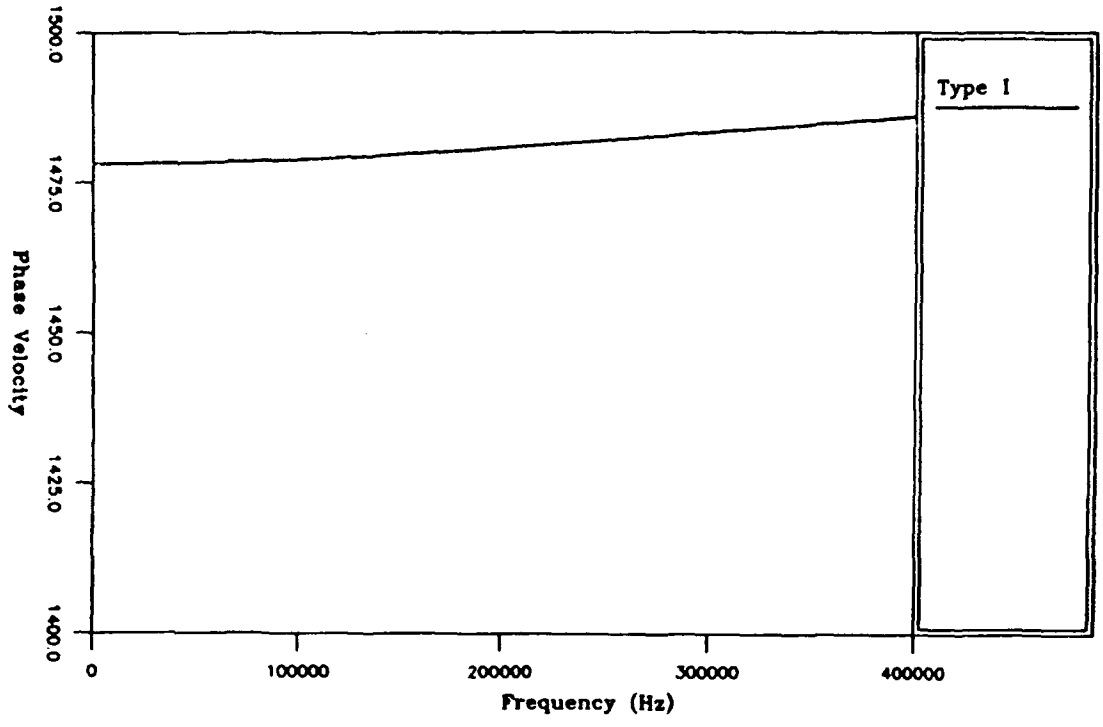

Figure 2.8 Type I wave phase velocity for silty clay

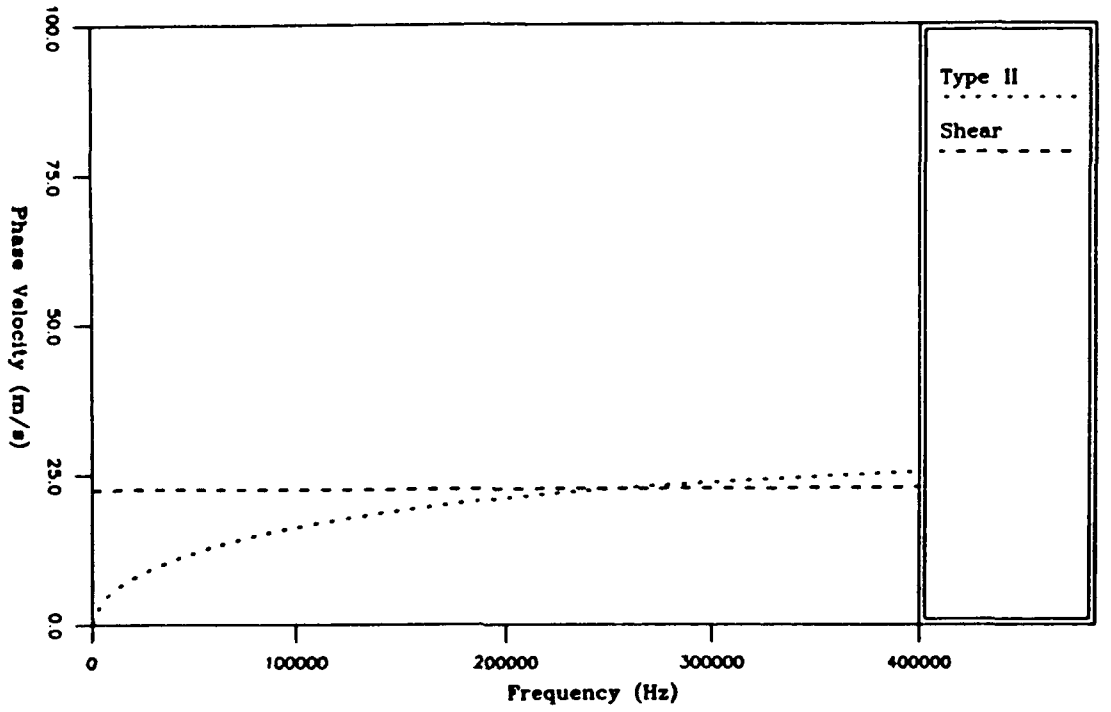

Figure 2.9 Type II and shear wave phase velocity for silty clay

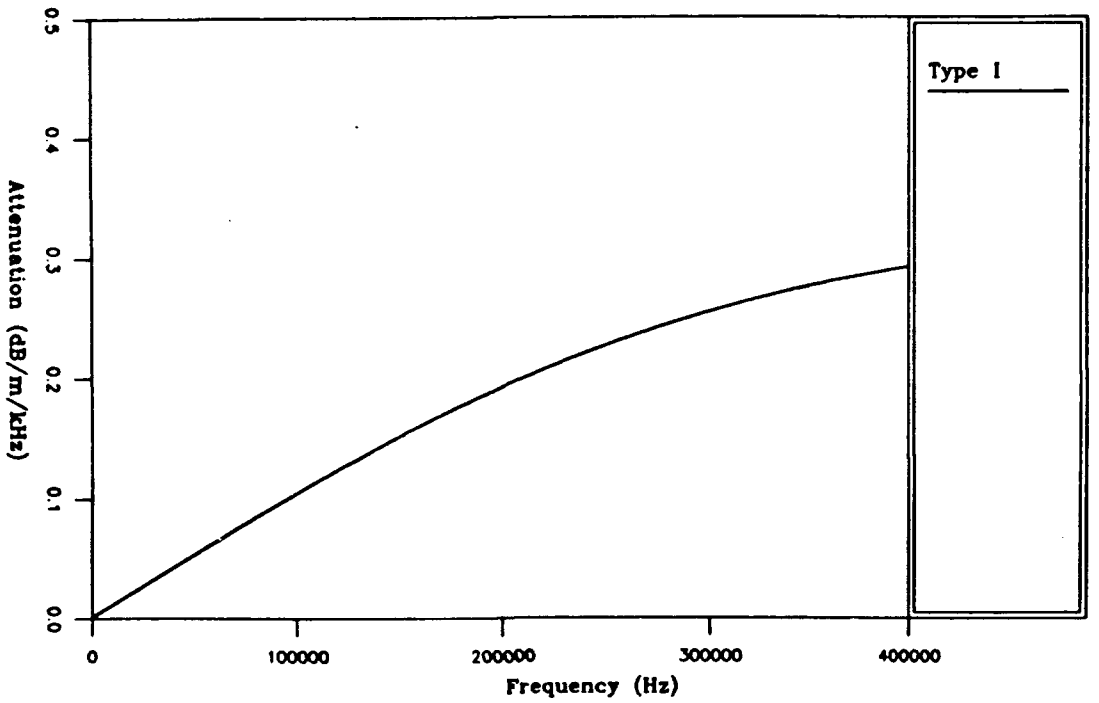

Figure 2.10 Type I wave attenuation for silty clay

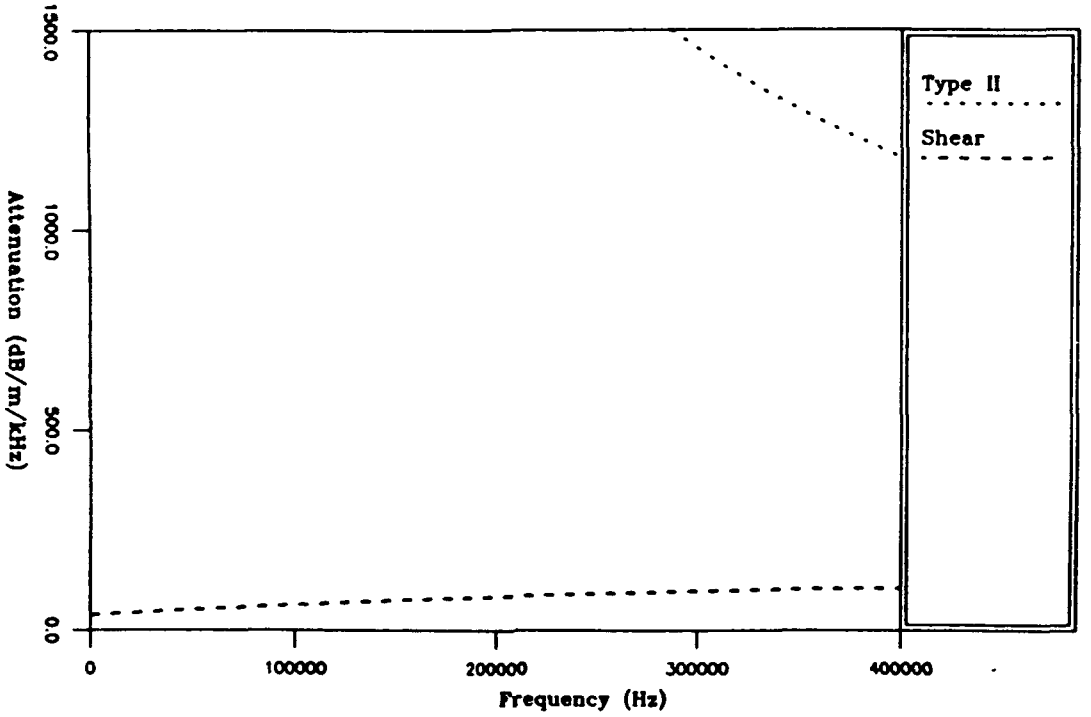

Figure 2.11 Type II and shear wave attenuation for silty clay

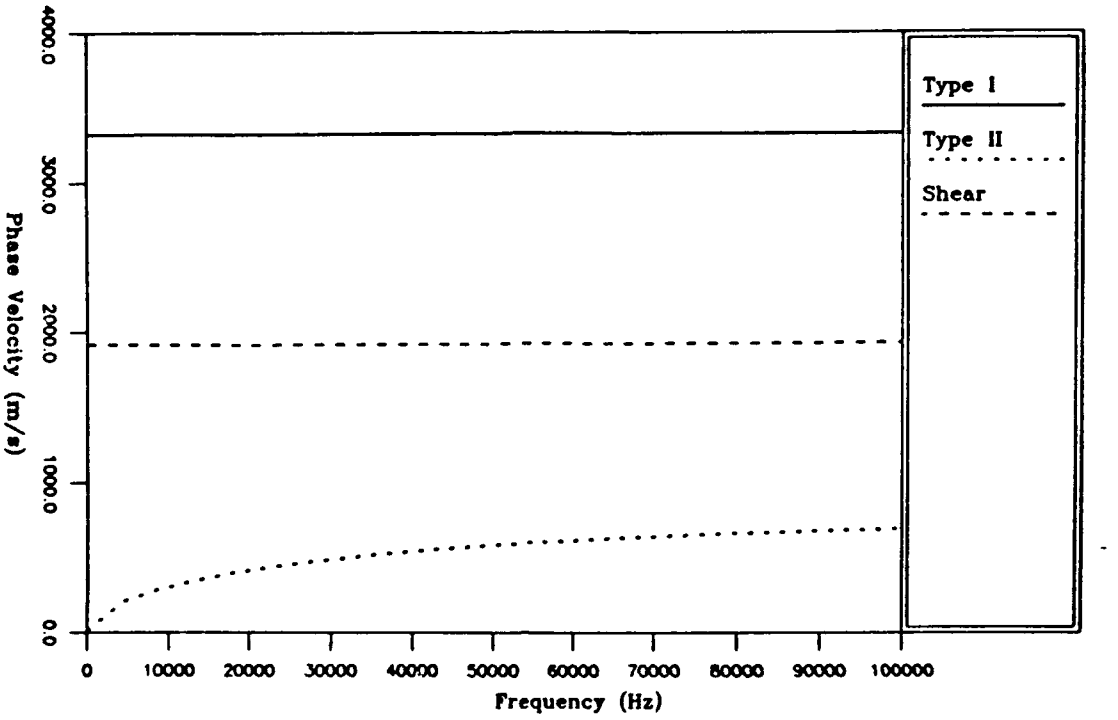

Figure 2.12 Type I, Type II, and shear wave phase velocity for sandstone

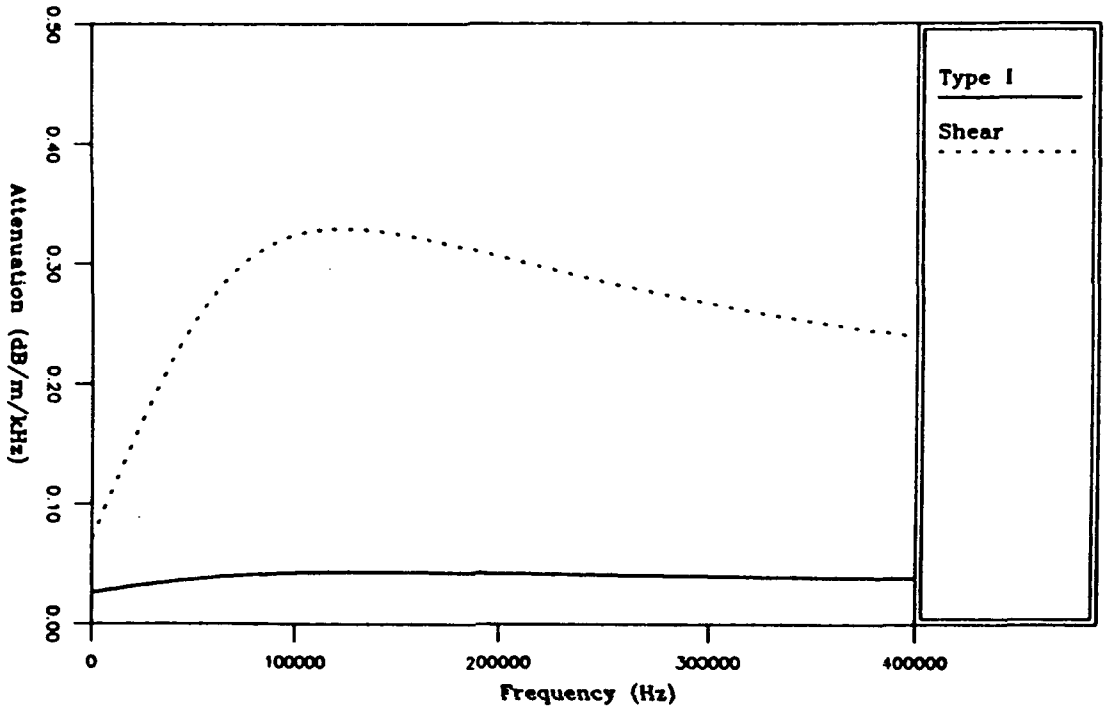

Figure 2.13 Type I and shear wave attenuation for sandstone

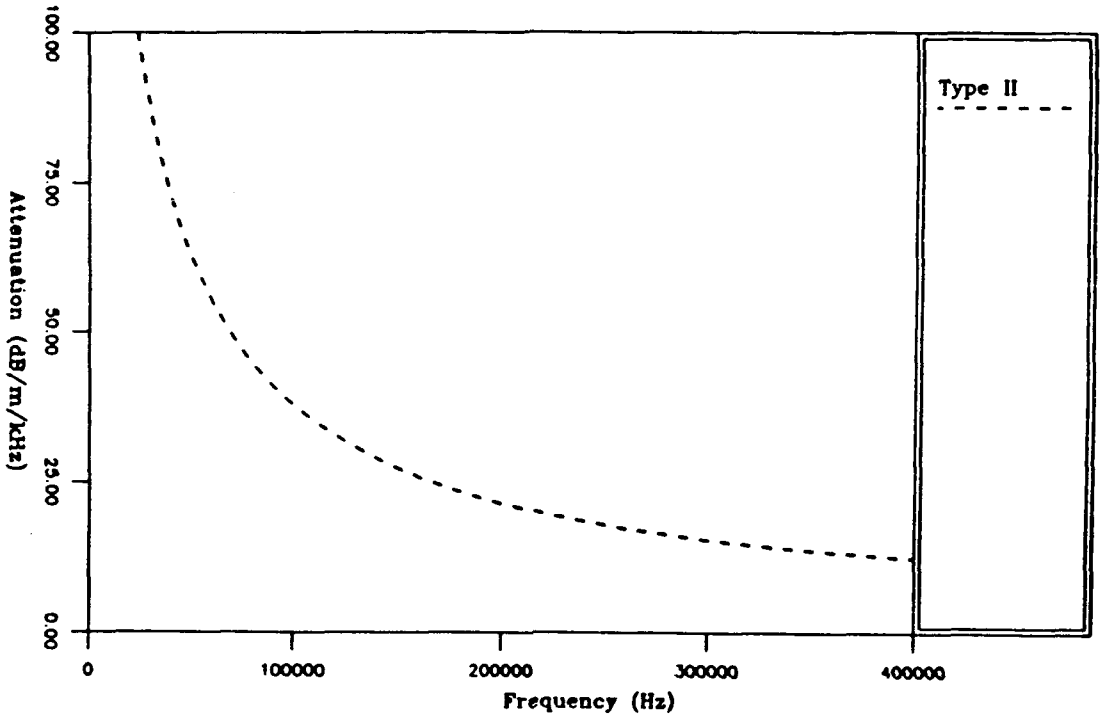

Figure 2.14 Type II wave attenuation for sandstone

3) equilibrium of tangential traction

$$\frac{\partial u_x}{\partial z} + \frac{\partial u_z}{\partial x} = 0 \qquad ; \quad z = 0$$

4) equilibrium of fluid pressure (open pores)

$$M(\nabla \cdot \mathbf{w}) - C(\nabla \cdot \mathbf{u}) = p \qquad ; z = 0$$

and the Fourier transforms of the boundary conditions are:

1) $$\hat{U}_{oz} = \hat{u}_z - \hat{w}_z \qquad ; z = 0 \qquad (2.69)$$

2) $$H\left(-ik_x\hat{u}_x + \frac{\partial u_z}{\partial z}\right) - C\left(-ik_x\hat{w} + \frac{\partial w_z}{\partial z}\right) + 2\mu ik_x\hat{u}_x = -\hat{p} \qquad ; z=0$$

3) $$\frac{\partial \hat{u}_x}{\partial x} - ik_x\hat{u}_z, = 0 \qquad ; z=0$$

4) $$M\left(-ik_x\hat{w}_x + \frac{\partial \hat{w}_z}{\partial x}\right) - C\left(-ik_x\hat{u}_x + \frac{\partial \hat{u}_z}{\partial z}\right) = \hat{p} \qquad ; z=0$$

Then, substituting the equations for transformed pressure and displacement Eq (2.17, 2.22, 2.65, 2.66) in the boundary conditions, the expression for the reflection and transmission factors is obtained as:

$$\begin{bmatrix} \alpha & \alpha_p(1-G_p) & \alpha_2(1-G_2) & -k_x(1-G_s) \\ \rho_o & \frac{CG_p-H}{V_p^2}+\frac{2\mu k_x^2}{\omega^2} & \frac{CG_2-H}{V_2^2}+\frac{2\mu k_x^2}{\omega^2} & \frac{2k_x\alpha_s\mu}{\omega^2} \\ 0 & \alpha_p & \alpha_2 & \frac{\omega^2}{2V_s^2k_x}-k_x \\ -\rho_o & \frac{C-MG_p}{V_p^2} & \frac{C-MG_2}{V_2^2} & 0 \end{bmatrix} \begin{bmatrix} \mathcal{R} \\ \mathcal{T}_p \\ \mathcal{T}_2 \\ \mathcal{T}_s \end{bmatrix} = \begin{bmatrix} \alpha \\ -\rho_o \\ 0 \\ \rho_o \end{bmatrix} e^{-i\alpha h} \tag{2.70}$$

which can be solved (see Appendix B) to obtain the reflection and transmission factors.

Chapter 3

PLANE WAVE COEFFICIENTS AND SURFACE WAVES

3.1 Exact Solution for Plane Wave Coefficients

In this section, the plane wave reflection coefficients from a water-sediment halfspace are examined where the sediment is modeled as a poro-viscoelastic solid, as a viscoelastic solid, and as a fluid. Both consolidated and unconsolidated sediments are considered. It will be instructive to consider the reflectivity from simplest model of the sediment to the most complex (i.e., fluid, solid, then poro-viscoelastic).

3.1.1 Single Phase Media

For a fluid-fluid interface the reflectivity is governed by

$$\bar{R}_{ff} = \frac{\rho_1 V_1 \cos\theta_o - \rho_o V_o \cos\theta_1}{\rho_1 V_1 \cos\theta_o + \rho_o V_o \cos\theta_1} \tag{3.1}$$

which is independent of frequency. The subscript "o" signifies the medium where the wave originates and the 1 signifies the transmitting medium. For a non-lossy material the critical angle is defined as the angle above which there is total reflection and is given by

$$\theta_c = \sin^{-1}\left[\frac{V_o}{V_1}\right] \quad ; \; V_1 > V_o \tag{3.2}$$

where V_o is the velocity of the medium where the wave originates and V_1 is the velocity of the transmitting medium. For any real material with frictional and/or viscous losses, there is no critical angle, since there is no total reflection. It is, however, useful to refer to that angle that divides angle space from nearly total reflection to moderate or small reflectivity.

This angle will be called (for lack of any universally applied name) the pseudo-critical (p-c) angle:

$$\theta_{pc} = \sin^{-1}\left[\frac{Re\{k_1\}}{Re\{k_0\}}\right] \quad ; \; Re\{k_0\} > Re\{k_1\} \tag{3.3}$$

where k is the complex wavenumber. For a non-lossy material the angle of intromission is defined as that angle for which the reflection coefficient is zero and is given by:

$$\theta_i = \sin^{-1}\left[\frac{\rho_1^2 V_1^2 - \rho_0^2 V_0^2}{\rho_1^2 V_1^2 - \rho_0^2 V_1^2}\right]^{1/2} \quad ; V_1 < V_0, \; \rho_1 > \rho_0 \tag{3.4}$$

For a lossy medium, the reflection coefficient is non-zero at all angles and the pseudo-intromission angle is:

$$\theta_{pi} = \sin^{-1}\left[\frac{\rho_1^2 \, Re\{k_0\}^2 - \rho_0^2 \, Re\{k_1\}^2}{\rho_1^2 \, Re\{k_0\}^2 - \rho_0^2 \, Re\{k_0\}^2}\right]^{1/2} ; Re\{k_0\} < Re\{k_1\}, \; \rho_1 > \rho_0. \tag{3.5}$$

Figure 3.1 shows the magnitude of the plane wave reflection coefficient of the amplitude of the displacement potential for a sand, silty clay, and sandstone. The angle of pseudo-intromission exists for the clay and pseudo-critical angles exist for the sand and sandstone. The geoacoustic parameters are given in Table 3.1. For all plots in this chapter the upper halfspace velocity is 1524 m/s and the density is 1.024 g/cm^3.

For a fluid-viscoelastic solid interface the reflectivity is governed by

$$\bar{R}_{fs} = \frac{\rho_1 V_1 \cos\theta_0 \left[\cos^2(2\gamma_1)\cos\gamma_1 + \frac{V_s}{V_1}\sin^2(2\gamma_1)\cos\theta_1\right] - \rho_0 V_0 \cos\theta_1 \cos\gamma_1}{\rho_1 V_1 \cos\theta_0 \left[\cos^2(2\gamma_1)\cos\gamma_1 + \frac{V_s}{V_1}\sin^2(2\gamma_1)\cos\theta_1\right] + \rho_0 V_0 \cos\theta_1 \cos\gamma_1} \tag{3.6}$$

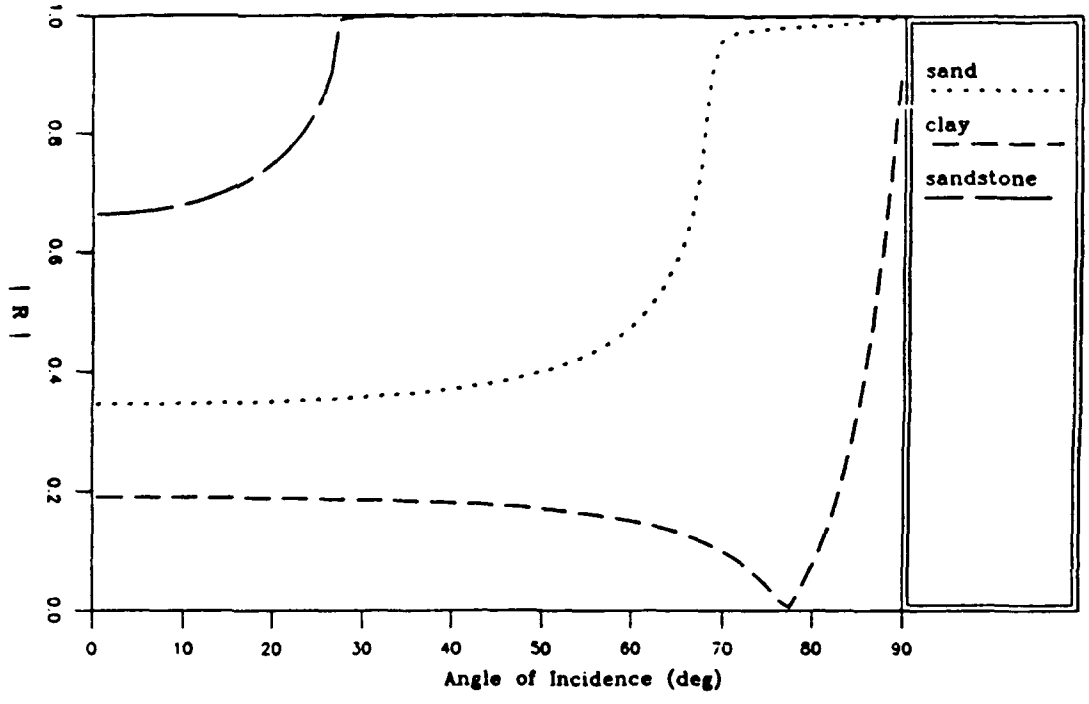

Figure 3.1 Plane wave reflection coefficients at a fluid-fluid boundary

which is also independent of frequency. V_s is the shear velocity and γ_1 is the angle of the refracted shear wave. For this case two critical angles can arise, one due to the compressional wave (as in the fluid case) and one due to the shear wave:

$$\theta_{pcs} = \sin^{-1}\left[\frac{\mathrm{Re}\,\{k_s\}}{\mathrm{Re}\,\{k_o\}}\right] \qquad ;\mathrm{Re}\,\{k_o\} > \mathrm{Re}\,\{k_s\}. \tag{3.7}$$

Figure 3.2 shows the magnitude of plane wave reflection coefficient for the same marine sand, clay , and sandstone case as in Table 3.1 with shear wave parameters added (see Table 3.2). The reflectivity for the viscoelastic sand and clay sediments is essentially identical with that for the fluid sediments (see Figure 3.1) indicating that the conversion of energy to shear waves is negligible for these material parameters. Loss of energy to shear waves is clearly seen in the sandstone case (compare Figures 3.1 and 3.2) and the shear pseudocritical angle is apparent at 51°. The geoacoustic parameters are given in Table 3.2.

Table 3.1 Geoacoustic Parameters for the Single-Phase Fluid Model

Property	Units	Sand	Silty-Clay	Sandstone
Compressional velocity	m/s	1638.52	1478.22	3331.52
Compressional attenuation	dB/m/kHz	.07	.0018	.039
Density	g/cm^3	1.961	1.554	2.320

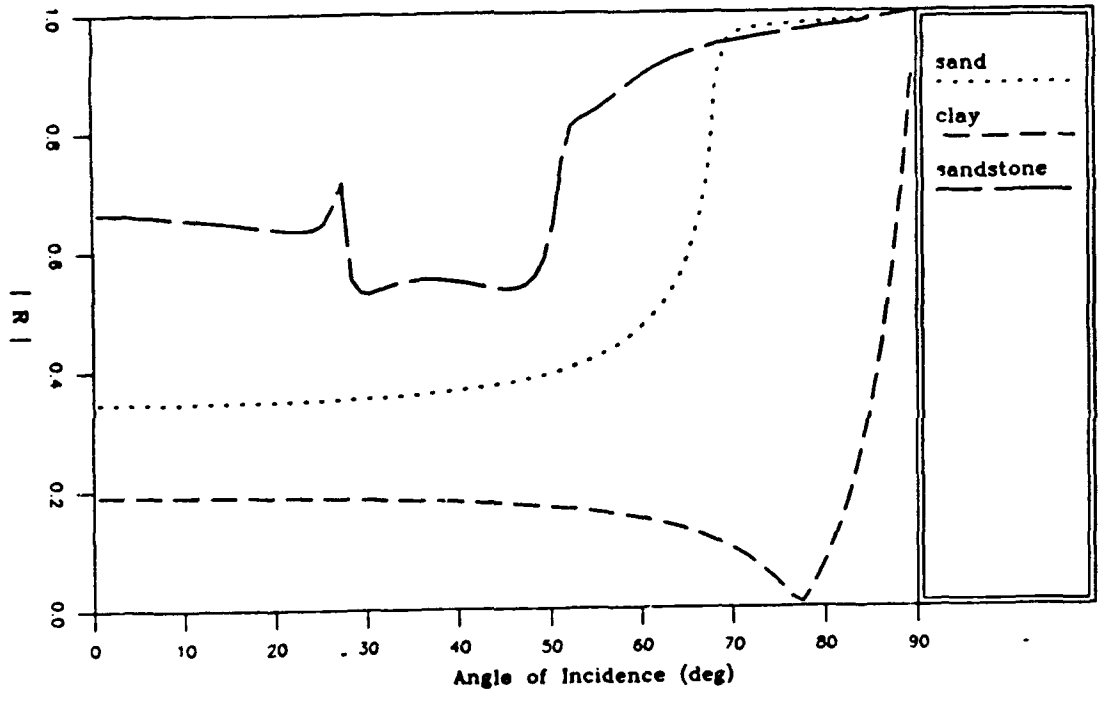

Figure 3.2 Plane wave reflection coefficients at a fluid-viscoelastic boundary

Table 3.2 Geoacoustic Parameters for the Single-Phase Solid Model

Property	Units	Sand	Silty-Clay	Sandstone
Compressional velocity	m/s	1638.52	1478.22	3331.52
Compressional attenuation	dB/m/kHz	.070	.0018	.039
Shear velocity	m/s	121.83	22.5	1949.65
Shear attenuation	dB/m/kHz	4.474	38.83	.239
Density	g/cm^3	1.961	1.554	2.320

3.1.2 Two-Phase Porous Media

For a fluid-poro-viscoelastic interface, the plane wave reflection and transmission coefficients are related to the reflection and transmission factors in Eq. (2.70) by

$$\bar{\mathcal{R}} = \mathcal{R}\, e^{i\alpha h} \tag{3.8}$$

$$\bar{\mathcal{T}}_p = \mathcal{T}_p\, e^{i\alpha h}$$

$$\bar{\mathcal{T}}_2 = \mathcal{T}_2\, e^{i\alpha h}$$

$$\bar{\mathcal{T}}_s = \mathcal{T}_s\, e^{i\alpha h}$$

Substituting these definitions in Eq. (2.70), the factor $e^{i\alpha h}$ drops out and the plane wave coefficients depend solely on material properties and not on source height.

3.1.2.1 Sand: $V_p > V_o$, $V_s < V_o$

Figure 3.3 shows the plane wave reflection coefficient of the amplitude of the displacement potential for the marine sand given in Table 2.1. There are three important differences between the reflectivity from porous material and reflectivity from a single phase fluid or solid material. First, note that reflectivity from a poro-viscoelastic medium is frequency dependent. In particular the p-c angle is a function of frequency and decreases monotonically with increasing frequency (from roughly 82° at 10 Hz to 70° at 10 kHz). It is clear that the decrease in the p-c angle arises from the increase in the phase velocity of the Type I wave (which is the only wave type that meets the criterion $\mathrm{Re}\{k_o\} > \mathrm{Re}\{k_1\}$). Figure 3.4 shows the frequency dependence of the p-c angle based on Eq. (3.2) for the marine sand parameters in Table 2.1.

The second feature of importance in Figure 3.3 is the dependence of the reflection coefficient on frequency above the critical angle. In this angular regime, the reflection coefficient is inversely proportional to the attenuation per cycle. The minimum of the reflection coefficient occurs at the peak of the attenuation (see Figure 2.5) between 100 Hz and 1000 Hz.

The third feature of interest is the reflectivity at normal incidence. For a single phase fluid, the reflection coefficient at normal incidence is

$$\bar{R}_{ff}(\theta_o = 0) = \frac{\rho_1 V_1 - \rho_o V_o}{\rho_1 V_1 + \rho_o V_o} \tag{3.9}$$

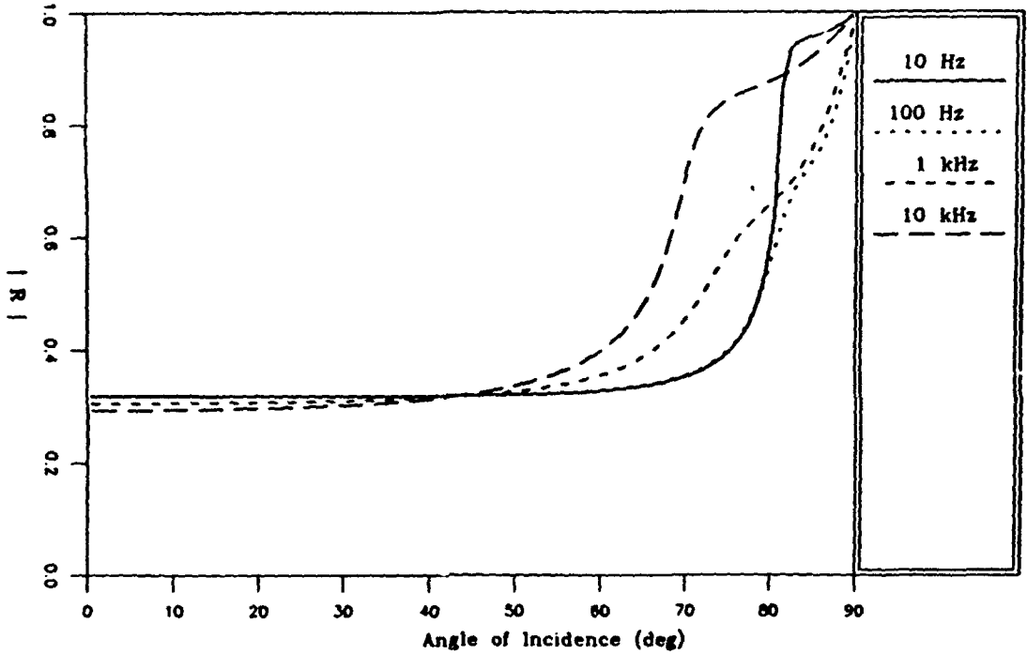

Figure 3.3 Plane wave reflection coefficients at a fluid-poro-viscoelastic boundary. The sediment is sand.

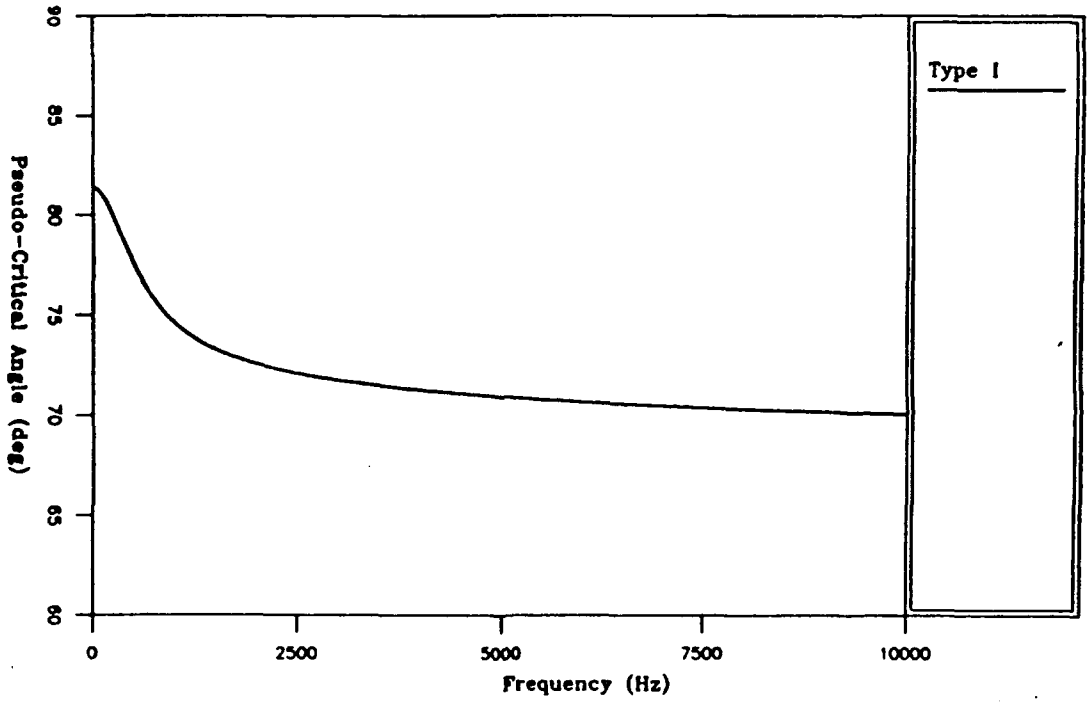

Figure 3.4 Pseudo-critical angle for a poro-viscoelastic sand from Biot theory

which increases as V_1 increases. Since we have seen (e.g. Figure 2.3) that for porous media V_1 increases as a function of frequency we might guess that normal incidence reflectivity increases as a function of frequency. From Figure 3.3, however, reflectivity decreases as a function of frequency. This is due to the excitation of Type II waves in the porous medium as frequency increases as shown in Figure 3.5.

3.1.2.2 Silty Clay: $V_p < V_o$, $V_s < V_o$

Figure 3.6 shows the reflectivity from a fluid-silty clay interface where the parameters for the silty clay are given in Table 2.1. Over this frequency band the sediment has a negligible velocity dispersion (see Figure 2.8) and a nearly linear dependence of attenuation (see Figure 2.10) on frequency, thus the reflectivity is also nearly independent of frequency. Also, the shear wave and Type II wave in the clay have a low velocity with respect to that of the incoming wave so that the reflectivity is negligibly influenced by these wave types.

3.1.2.3 Sandstone: $V_p > V_o$, $V_s > V_o$

Figure 3.7 shows the reflection coefficient for the sandstone parameters given in Table 2.1. The critical angle for the compressional wave (26°) and the shear wave (50°) are both apparent. Reflectivity decreases with frequency monotonically at all angles of incidence due to the increasing transmissivity of the Type II wave (see Figure 3.8). The p-c angle for the Type I wave is nearly independent of frequency since the ratio Vp/Vo changes less than .2% over this frequency band. The p-c angle for the shear wave, however, appears to decrease with increasing frequency. The shear velocity is indeed dispersive, but increases with frequency so that from Eq. (3.7) we would expect the p-c

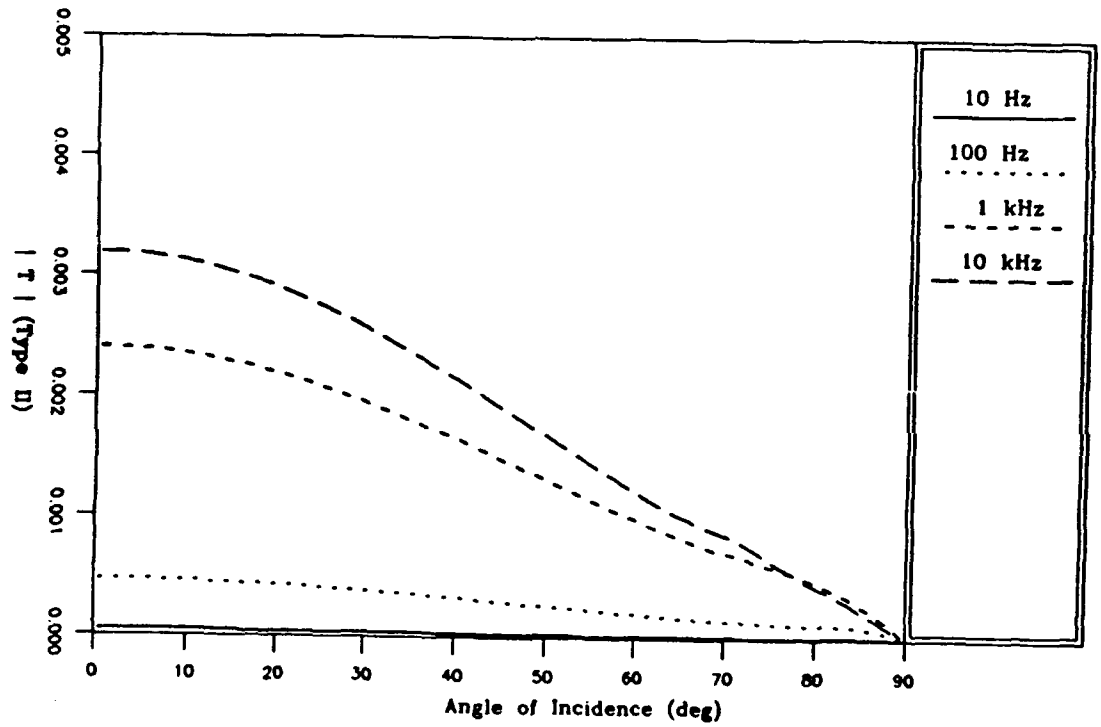

Figure 3.5 Type II wave transmissivity for poro-viscoelastic sand

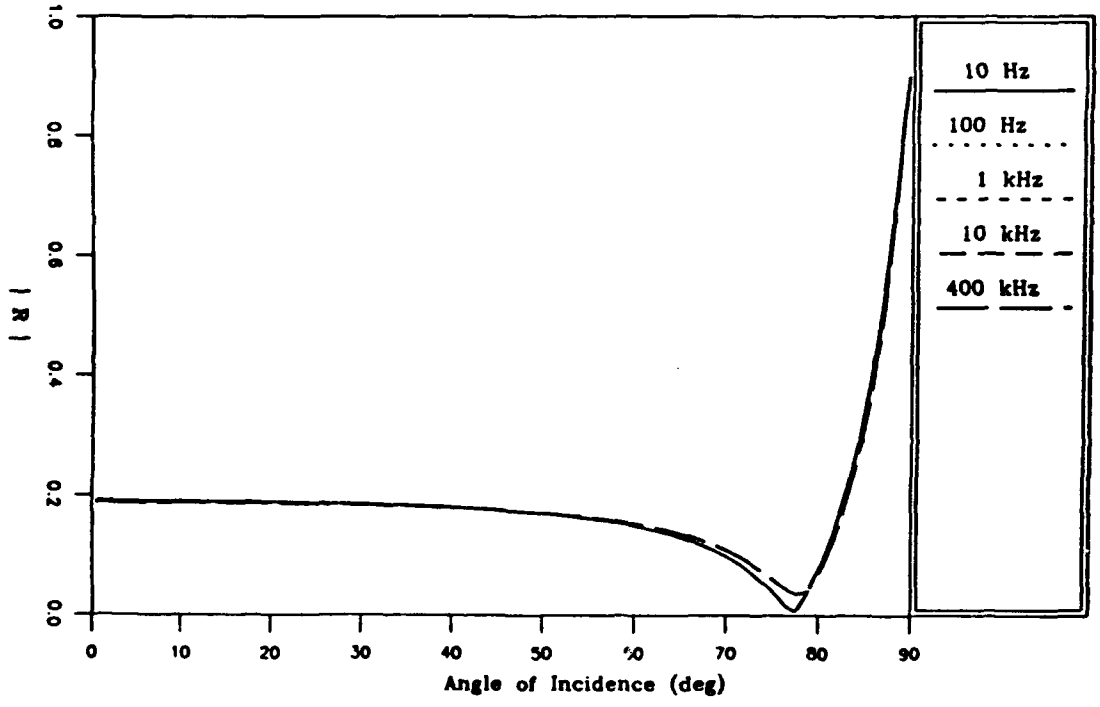

Figure 3.6 Plane wave reflection coefficients at a fluid-poro-viscoelastic boundary. The sediment is silty-clay.

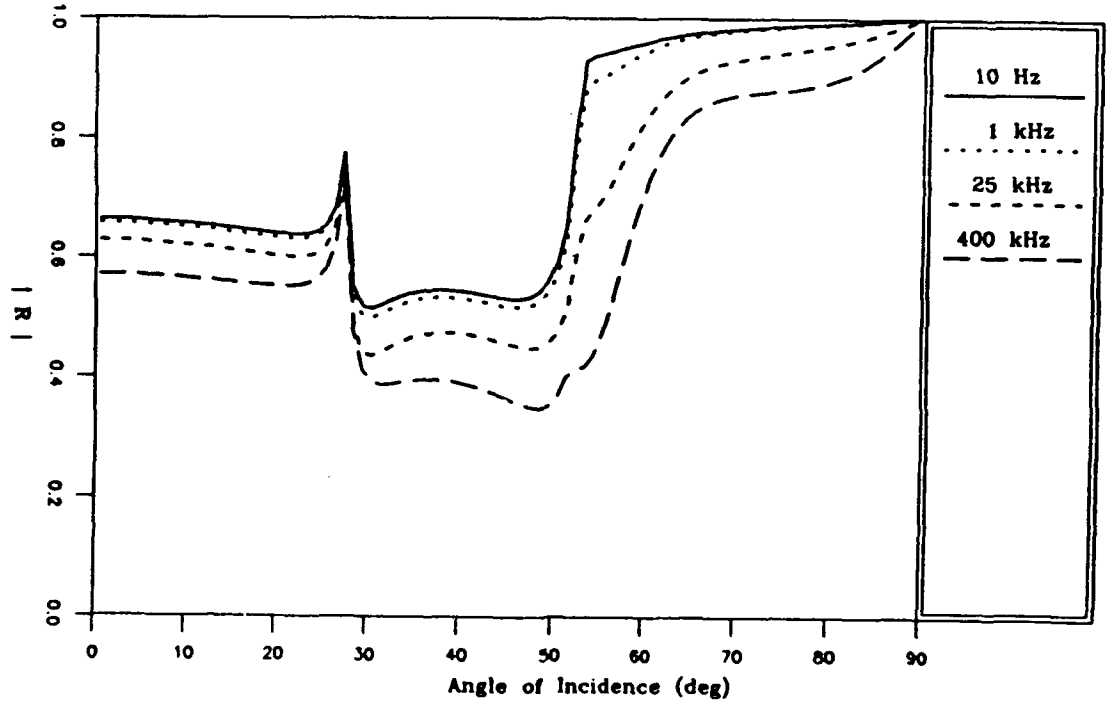

Figure 3.7 Plane wave reflection coefficients at a fluid-poro-viscoelastic boundary. The sediment is sandstone.

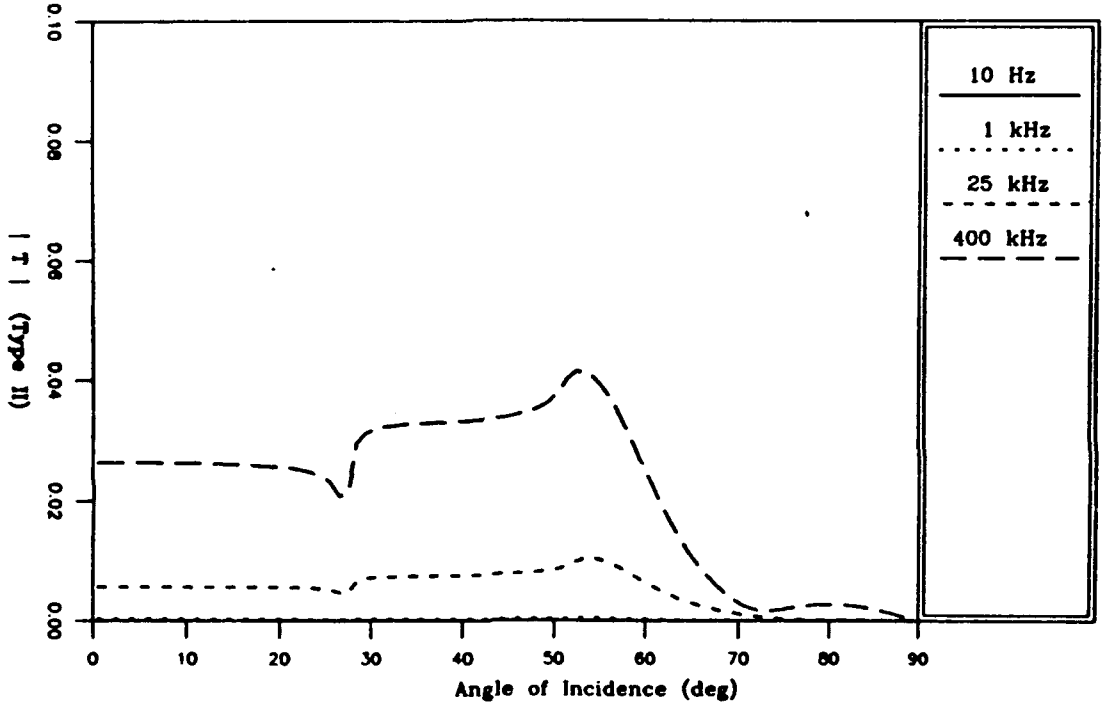

Figure 3.8 Plane wave transmission coefficients for the Type II wave at a fluid-poro-viscoelastic boundary. The sediment is sandstone.

angle to increase slightly with angle. The decrease in reflectivity around the shear p-c angle (which manifests itself as an apparent shift in p-c angle) is due instead to the increase of transmissivity of the Type II wave near this angle (see Figure 3.8).

3.2 Implications for Acoustic Propagation Predictions

In support of acoustic propagation experiments, sediment cores are commonly taken to obtain measurements of compressional velocity (occasionally also shear velocity) and attenuation. Recently, techniques have been developed to measure these quantities *in situ*. Typical frequencies for either lab or *in situ* measurements are in the hundreds of kilohertz. In developing a low frequency geoacoustic model, the velocity is generally assumed independent of frequency and the attenuation is assumed linearly dependent on frequency and extrapolated down to the frequency of interest. In this section the effects of this oversimplified extrapolation are demonstrated, by comparing reflectivity predicted by current methodology, as outlined above, and Biot theory.

3.2.1 Sand: $V_p > V_o$, $V_s < V_o$

Figure 3.9 shows the reflectivity from a poro-viscoelastic solid as a function of frequency along with the prediction of a fluid geoacoustic model that has been extrapolated. (The velocity and attenuation of the fluid approximation to the sediment were calculated from Biot theory at 400 kHz where measurements of these properties are most commonly taken). The differences between the fluid sediment model and porous sediment model are striking. For long-range propagation in shallow water the reflectivity at high angles tends to determine the characteristics of the transmission loss: the location of the p-c angle governs the number of modes that will propagate and the reflectivity above the p-c angle

governs the modal attenuation coefficient. The extrapolated fluid model thus overpredicts the number of propagating modes and underpredicts the modal attenuation coefficient for propagation between 100 Hz and several kHz. The results for extrapolating a solid model from 400 kHz would be essentially identical to that of the fluid shown in Figure 3.9.

3.2.2 Silty Clay: $V_p < V_0$, $V_s < V_0$

Figure 3.10 shows the reflectivity from a poro-viscoelastic silty clay as a function of frequency along with the prediction of the extrapolated fluid model (predictions of the extrapolated fluid and extrapolated solid model were identical to within the width of a plotted line). The complex velocity for the extrapolated model was obtained from Biot theory at 400 kHz as in the sand case. The predictions of reflectivity using the single-phase fluid approximation are quite comparable to the full Biot predictions except near the angle of intromission, where the full theory predicts a lower reflectivity. At the angle of intromission, the reflection coefficient is proportional to the compressional attenuation per wavelength; Biot theory predicts a non-linear frequency dependence on attenuation between 400 kHz and the kilohertz regime (see Figure 2.10). Thus, the attenuation for the extrapolated model is too high.

Seafloor reflection experiments confirm that measurements of compressional wave attenuation at 400 kHz cannot be linearly extrapolated down to the 50 Hz - 1500 Hz band. In this band the strongest arrival from an explosive source impinging on the seafloor at low grazing angles comes from paths that refract through the sediment accumulating a loss proportional to sediment attenuation. Estimates of effective attenuation from these paths range from .001 dB/m/kHz - .03 dB/m/kHz (including measurements at roughly 200 deep-ocean sites in the North Atlantic, Pacific, Mediterranean and Indian Ocean (C.W. Spofford, personal communication)). Measured intrinsic attenuation in the hundreds of kHz across a core barrel for deep sea sediment types, however, has been in the

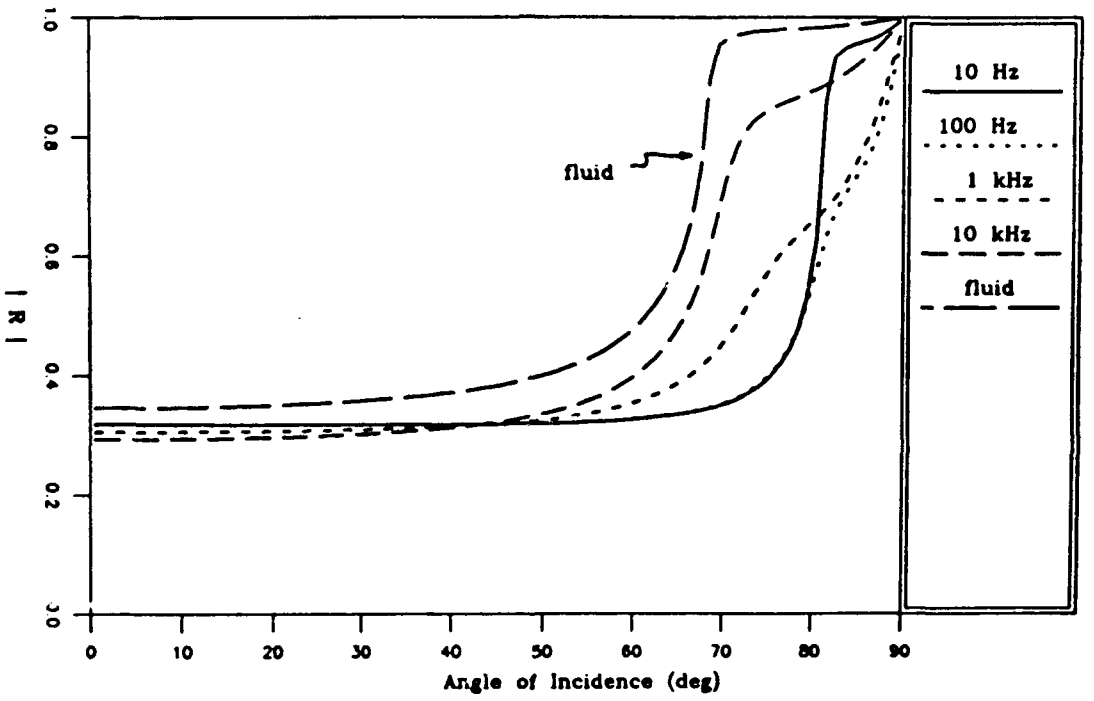

Figure 3.9 Comparison of reflectivity from a commonly used geoacoustic extrapolation technique with Biot theory. The sediment is sand.

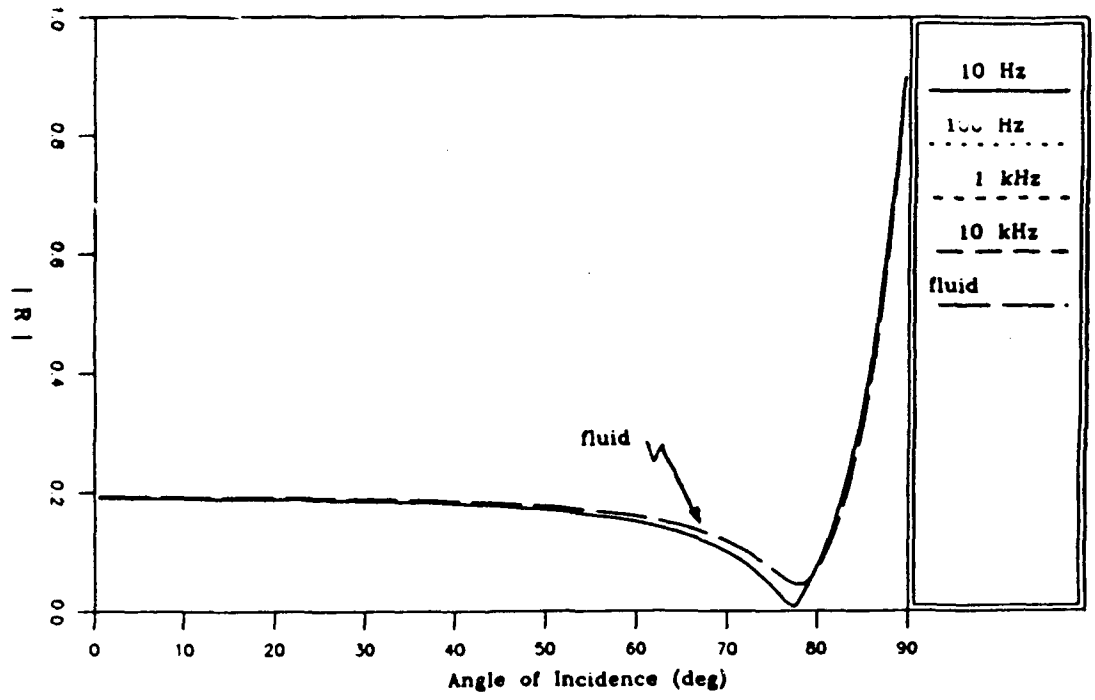

Figure 3.10 Comparison of reflectivity from a commonly used geoacoustic extrapolation technique with Biot theory. The sediment is silty clay.

range .03 dB/m/kHz - .10 dB/m/kHz. (see Hamilton (1980)). Since effective attenuation must be greater than or equal to intrinsic attenuation it is clear that the experimental evidence points to a non-linear frequency dependence of attenuation over the band 50 Hz - 400 kHz.

3.2.3 Sandstone: $V_p > V_o$, $V_s > V_o$

Figure 3.11 shows the reflectivity from a poro-viscoelastic sandstone as a function of frequency along with the prediction of the extrapolated solid and extrapolated fluid model. Again, the complex velocities for the extrapolated models were obtained at 400 kHz. As expected, the fluid model gives a very poor approximation to the poro-viscoelastic results since no shear wave p-c angle is predicted. The extrapolated solid model predictions are tolerable at the low-frequencies (less than 10 kHz) but at high frequencies the transmissivity of the Type II wave can reduce reflectivity by as much as 50%.

3.3 Approximate Models

Several attempts have been made to use Biot theory in a simplified "Biot fluid" formulation for unconsolidated sediments. This should be a reasonable approximation at low frequencies since the Type II wave has a negligible influence (at least at a single boundary) and the role of the sediment rigidity also is negligible. One such reflection model might be Eq. (3.1) with a frequency-dependent, complex velocity obtained from Biot predictions for the Type I wave. Likewise a "Biot solid" approximation model might be Eq (3.6) with the velocities obtained from Biot predictions for the Type I wave and the shear wave. Figure 3.12 contains such predictions compared with the full theory. In Figure 3.12, the "Biot fluid" approximation to the carbonate sand is quite good at low frequencies for all angles of incidence. The reflectivity under the approximate model, however, increases with increasing frequency near and at normal incidence; the full theory predicts a decreasing reflectivity with increasing frequency due to increased coupling to the Type II wave. At low frequencies (below 100 Hz) the results of the full and approximate

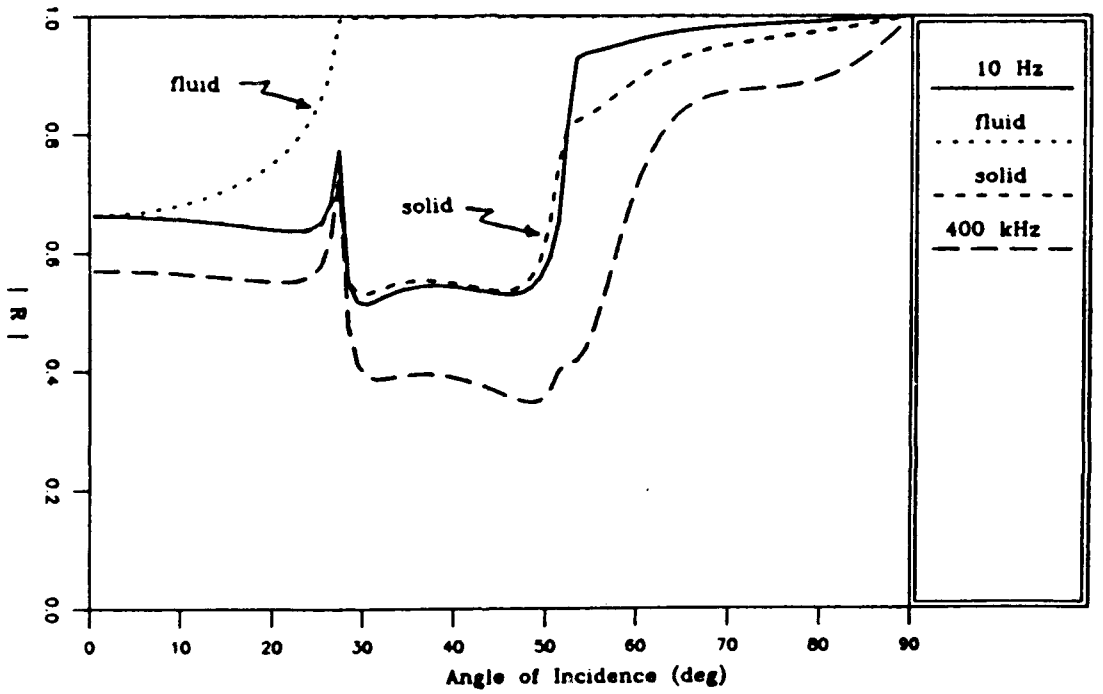

Figure 3.11 Comparison of reflectivity from a commonly used geoacoustic extrapolation technique with Biot theory. The sediment is sandstone.

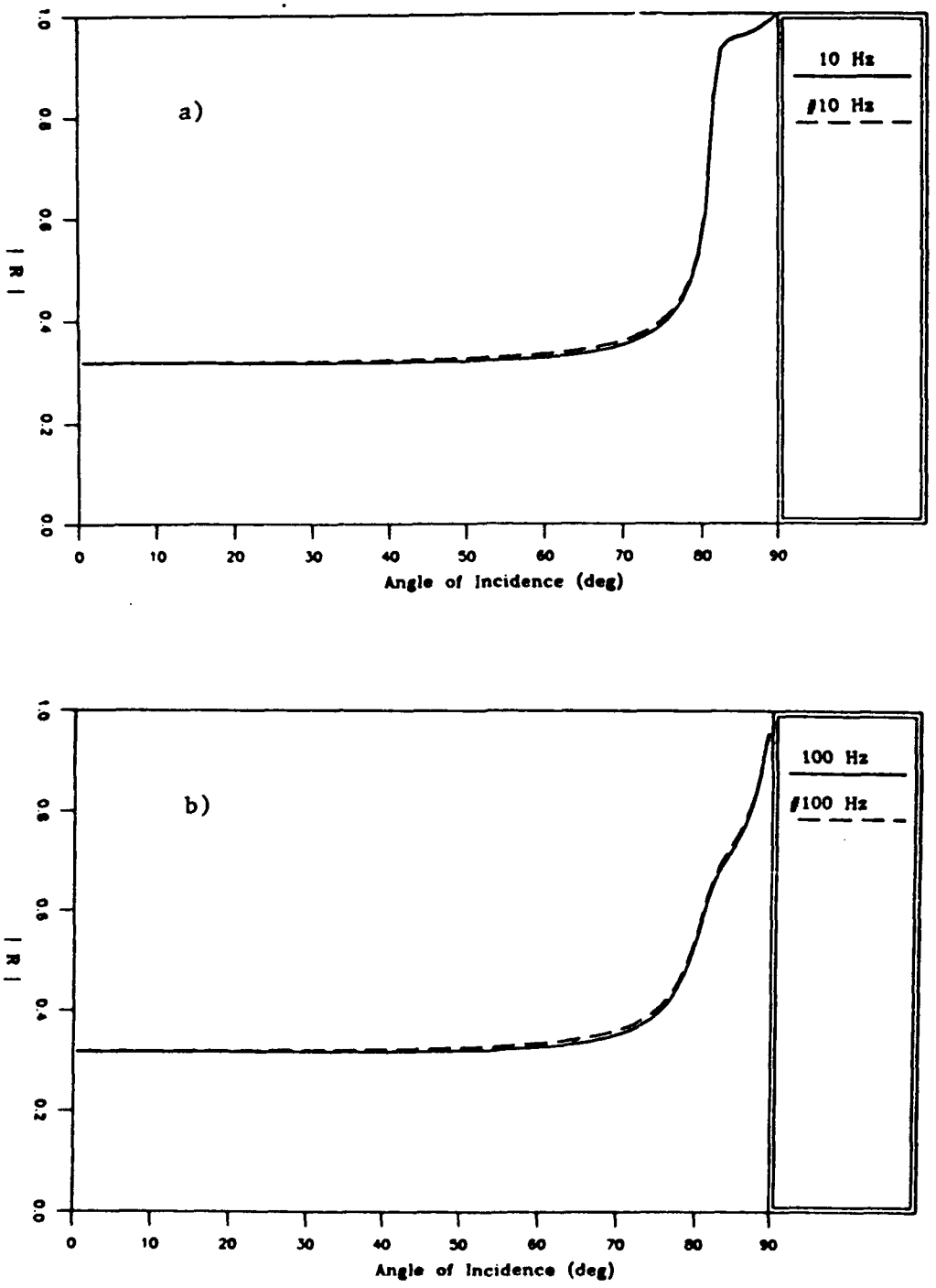

Figure 3.12a,b Comparison of Biot theory with an approximate model (#). The sediment is sand, the frequency is: a) 10 Hz; b) 100 Hz.

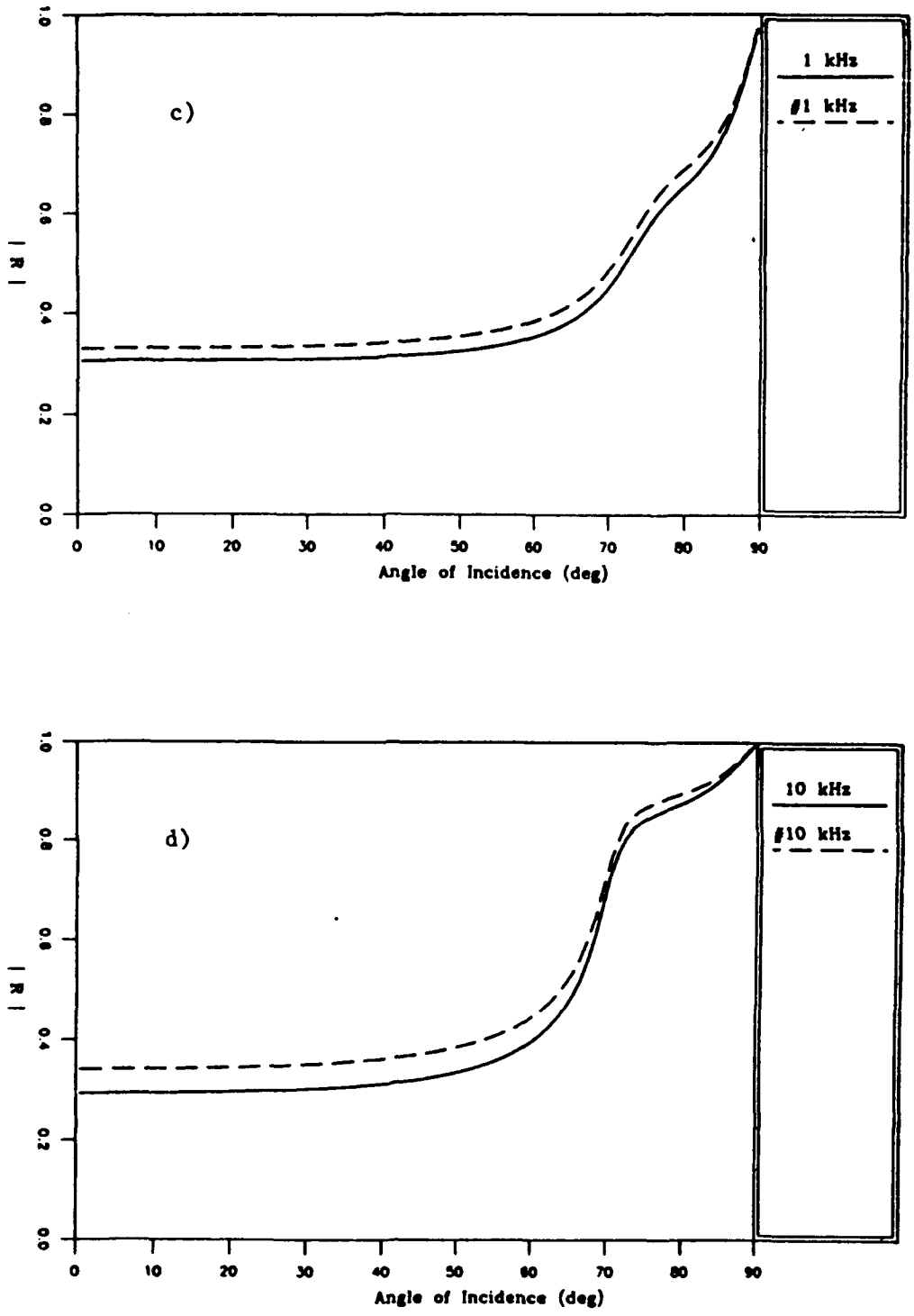

Figure 3.12c,d Comparison of Biot theory with an approximate model (#). The sediment is sand, the frequency is: c) 1 kHz; d) 10 kHz.

model are essentially identical near normal incidence. At 10 kHz, the approximate model predicts reflectivity about 15% higher than the full theory near normal incidence. In Figure 3.13, the "Biot solid" approximation to the sandstone is quite good at low frequencies (below 1 kHz). At higher frequencies, the Type II wave goes from diffusive to propagatory and more energy is transmitted to this wave type. Therefore, the approximate model that does not include this wave type is no longer applicable, and the full theory is required.

Beebe (1981) proposed an even simpler model, where the "Biot fluid" is modeled as having a constant phase velocity and an attenuation where the frequency exponent is calculated by Biot theory over the band of interest (in this case 50 Hz - 1000 Hz). The U.S. Navy standard low frequency bottom loss data base later employed a similar sediment model, where the frequency exponent is obtained by inversion of TL data rather than Biot theory. It is crucial, in this approximate model, that the constant phase velocity is obtained in the frequency band of interest. For example, in Beebe's study the velocities were obtained by dispersion analysis in the same frequency band in which the mode attenuation coefficients were measured resulting in ideal conditions for the approximate model to produce good results. A similar condition is obtained synthetically in Figure 3.14 by using a constant velocity (as predicted by Biot theory in the middle of the band of interest (50 Hz - 1000 Hz). Figure 3.14 compares the approximate model with the full theory (for the sand) where, in the approximate model, the imaginary part of the phase velocity comes from Biot theory and the real part is a constant value commensurate with the center of the band. The results are quite reasonable although the approximate model breaks down with increasing frequency as the assumed velocity becomes a poorer approximation of the true velocity.

Figure 3.15 shows the same comparison if the approximate model were developed using velocity data from core analysis. That is, the velocity used in the approximate

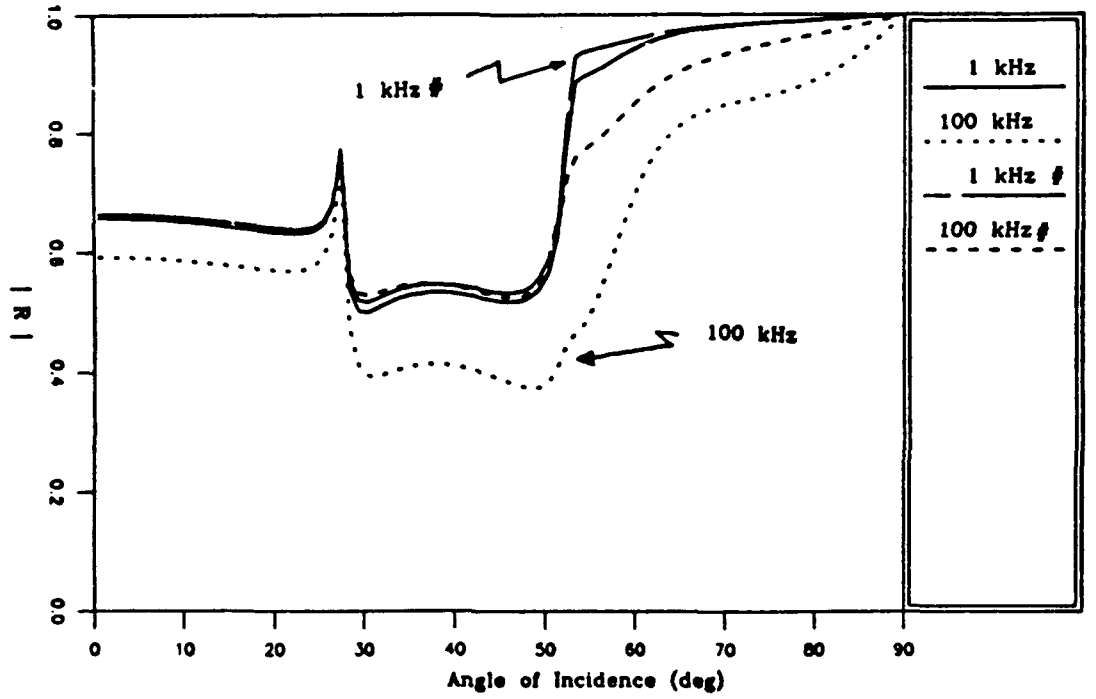

Figure 3.13 Comparison of Biot theory with an approximate model (#). The sediment is sandstone.

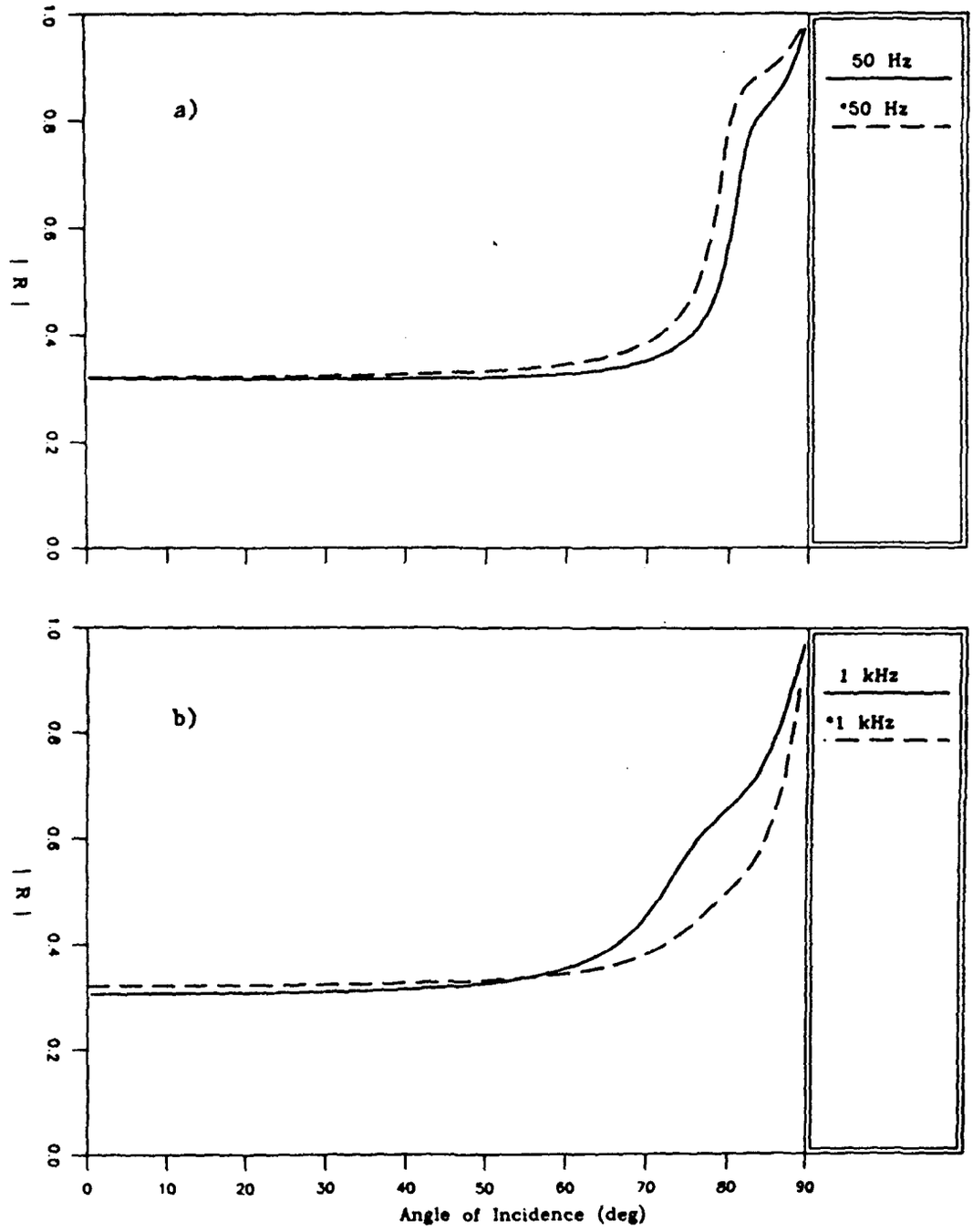

Figure 3.14 Comparison of Biot theory with the constant phase velocity approximate model (*). The constant phase velocity was derived within the 50 Hz - 1000 Hz band. Frequency is: a) 50 Hz; b) 1000 Hz.

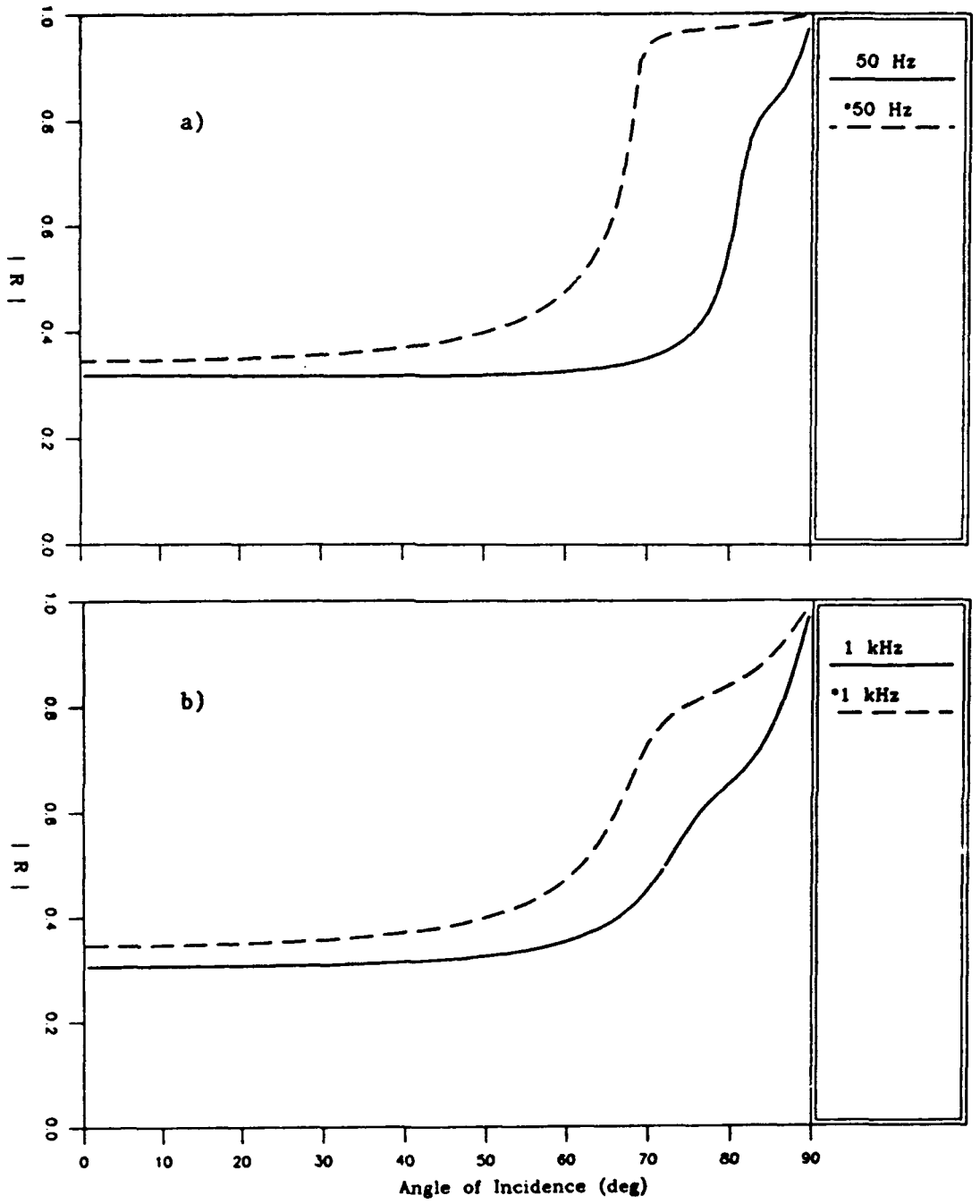

Figure 3.15 Comparison of Biot theory with the constant phase velocity approximate model (*). The constant phase velocity is derived at 400 kHz commensurate with velocity measurements on sediment cores. Frequency is: a) 50 Hz; b) 1000 Hz.

model here was obtained at 400 kHz from Biot theory. It is clear that using core data for input to the approximate model yields very poor results.

3.4 Interface Waves

Before proceeding to the inverse transform we consider the interface waves at a fluid-poro-viscoelastic boundary, the properties of which may be ascertained from the same set of simultaneous equations that govern the plane wave reflection and transmission coefficients. Various researchers have investigated related surface waves; however, it appears that the general case of surface waves at a fluid-poro-viscoelastic boundary (with complex wave speeds) has not been addressed. Deresewicz (1964) derived the secular equation without accounting for losses due to friction at the grain-to-grain contacts and Feng and Johnson (1983a and 1983b) considered the high frequency limit to the Biot theory where the viscous attenuation is zero.

The dispersion relation for these waves can be obtained by setting the denominator of the plane wave reflection and transmission coefficients to zero. From Cramers Rule, and Eq. (2.70) we have that

$$\mathrm{Det}\begin{bmatrix} \alpha & \alpha_p(1-G_p) & \alpha_2(1-G_2) & -k_x(1-G_s) \\ \rho_o & \dfrac{CG_p-H}{V_p^2}+\dfrac{2\mu k_x^2}{\omega^2} & \dfrac{CG_2-H}{V_2^2}+\dfrac{2\mu k_x^2}{\omega^2} & \dfrac{2k_x\alpha_s\mu}{\omega^2} \\ 0 & \alpha_p & \alpha_2 & \dfrac{\omega^2}{2V_s^2k_x}-k_x \\ -\rho_o & \dfrac{C-MG_p}{V_p^2} & \dfrac{C-MG_2}{V_2^2} & 0 \end{bmatrix}=0 \tag{3.10}$$

where the surface wave velocity, $V_{surf} = \omega/k_x$. Three kinds of surface waves can occur in the solution: a true surface wave that travels slower than all the wave speeds, a pseudo-Scholte wave that travels between the shear wave velocity and the Type II wave velocity (that leaks energy to the slower Type II wave), and a pseudo-Rayleigh wave that occurs when the surface wave velocity exceeds the velocity of the overlying water column.

Mathematically, the pseudo-Rayleigh wave arises from a pole on the lower Reimann sheet where $\mathrm{Im}\{\alpha\} > 0$ and $\mathrm{Im}\{\alpha_2\} > 0$. The true surface wave is located on the top Reimann sheet where $\mathrm{Im}\{\alpha_i\} < 0$, and the amplitude decays exponentially away from the boundary. The pseudo-Rayleigh wave amplitude actually increases away from the boundary (in the fluid) and this occurs because the wave radiates into the fluid at its trace velocity so that in a given plane perpendicular to the boundary, the points closer to the boundary in the fluid receive contributions from the wave further along the boundary (which are less energetic). This behavior of the received amplitude of the pseudo-Rayleigh wave is entirely commensurate with the behavior of a lateral wave.

The complex surface wave velocity from a single-phase solid will be calculated in order to compare with the results from poro-viscoelastic theory. The secular equation is given by Brekovskikh (1980) as:

$$\alpha \frac{\rho_T}{\rho_o}\left[4k_x^2\,\alpha_p\,\alpha_s + \left(\frac{\omega^2}{V_s^2} - 2k_x^2\right)\right] + \alpha_p \frac{\omega^4}{V_s^4} = 0 \qquad (3.11)$$

3.4.1 Sand: $V_p > V_o$, $V_s < V_o$

For the same sand case considered previously, the surface wave velocity as a function of frequency is plotted in Figure 3.16 along with the phase velocity of the Type II and shear wave. Note that the surface wave changes continuously from a pseudo-Scholte wave to a true surface wave at about 700 Hz[1]. Also plotted in Figure 3.16 is the surface wave velocity in the single phase solid approximation, where the complex phase velocities used to calculate the surface wave velocity were taken from Biot theory at 400 kHz. The single phase approximation to the surface wave velocity is roughly 10% higher than the full poro-viscoelastic predictions over this frequency band. The attenuation of the poro-viscoelastic surface wave shows a similar frequency dependence to the Type I and shear wave (Figure 3.17). The single-phase solid approximation to the surface wave attenuation is in general too conservative.

3.4.2 Silty Clay: $V_p < V_o$, $V_s < V_o$

The surface wave velocity for the silty clay changes continuously from a pseudo-Scholte wave to a true surface wave at 167 kHz (see Figure 3.18). The velocity dispersion of the surface wave is small so that the surface wave velocity under the single-phase solid approximation is quite good for this case. The single-phase approximation to the attenuation (Figure 3.19), however, is very poor.

---

1. The surface wave velocity and attenuation at 4.5 Hz (101 m/s and 25 dB/km) is coincidentally comparable to that measured by Shirmer (1980) (111 m/s and 7 dB/km) on a sandy bottom (of unknown material parameters) in the North Sea.

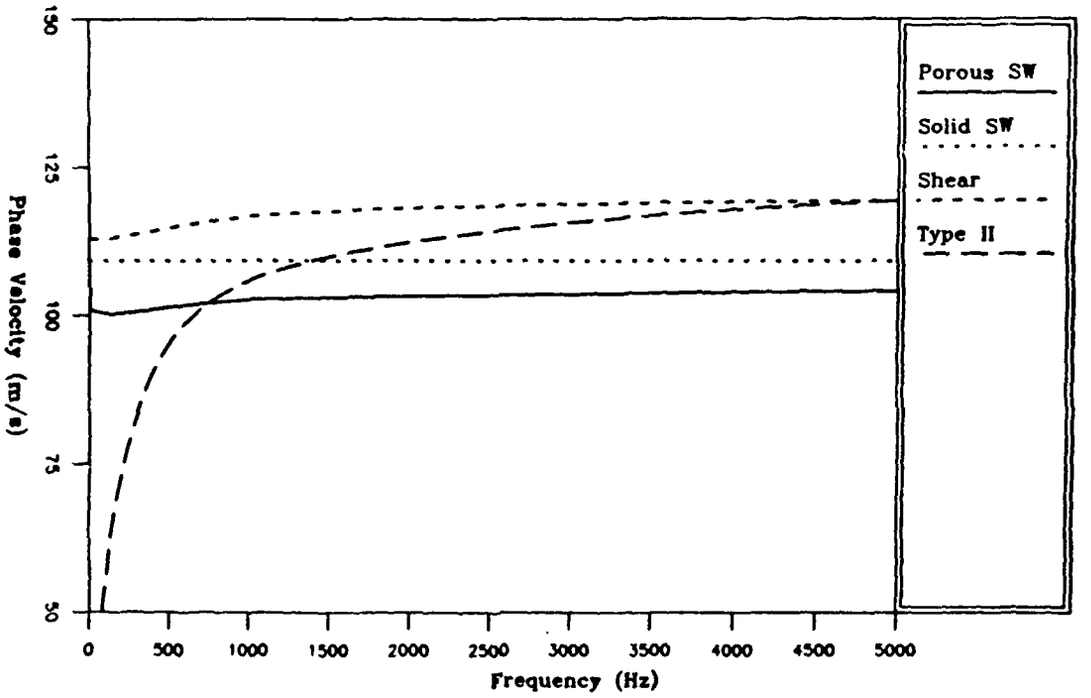

Figure 3.16 Phase velocity of various wave types in carbonate sand; pseudo-Scholte wave at a fluid-poro-viscoelastic boundary (porous SW); pseudo-Scholte wave at a fluid-viscoelastic boundary (solid SW); shear wave in a poro-viscoelastic sediment (shear); and Type II wave in a poro-viscoelastic sediment (Type II).

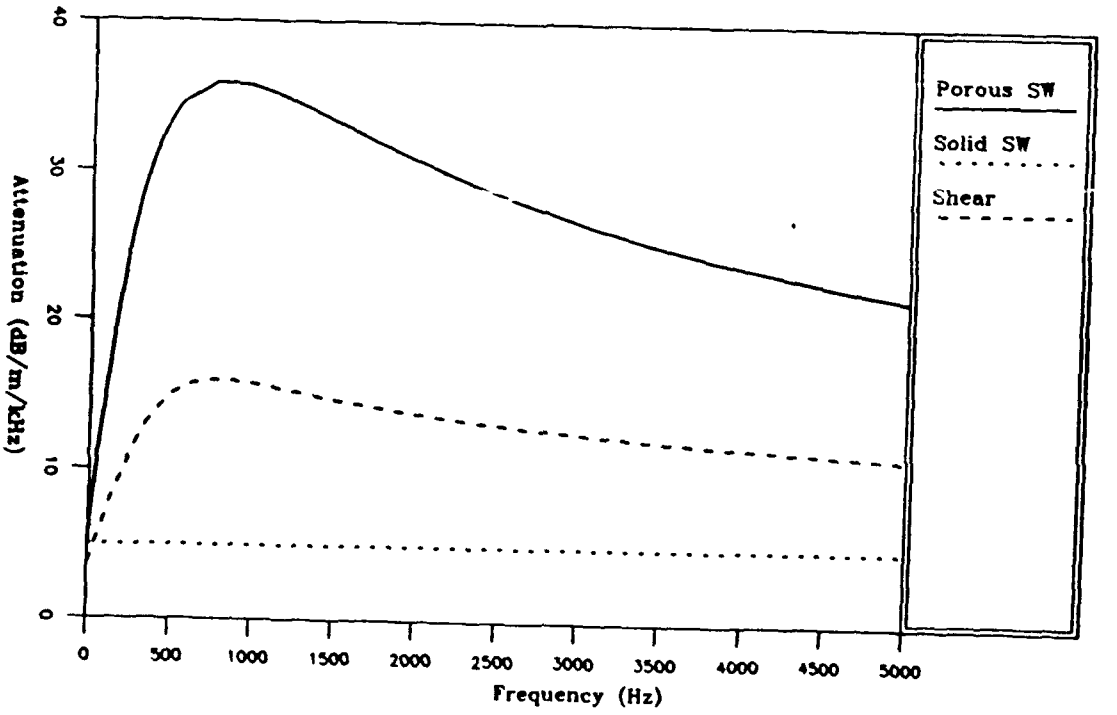

Figure 3.17 Attenuation of various wave types in carbonate sand; pseudo-Scholte wave at a fluid-poro-viscoelastic boundary (porous SW); pseudo-Scholte wave at a fluid-viscoelastic boundary (solid SW); and shear wave in a poro-viscoelastic sediment (shear).

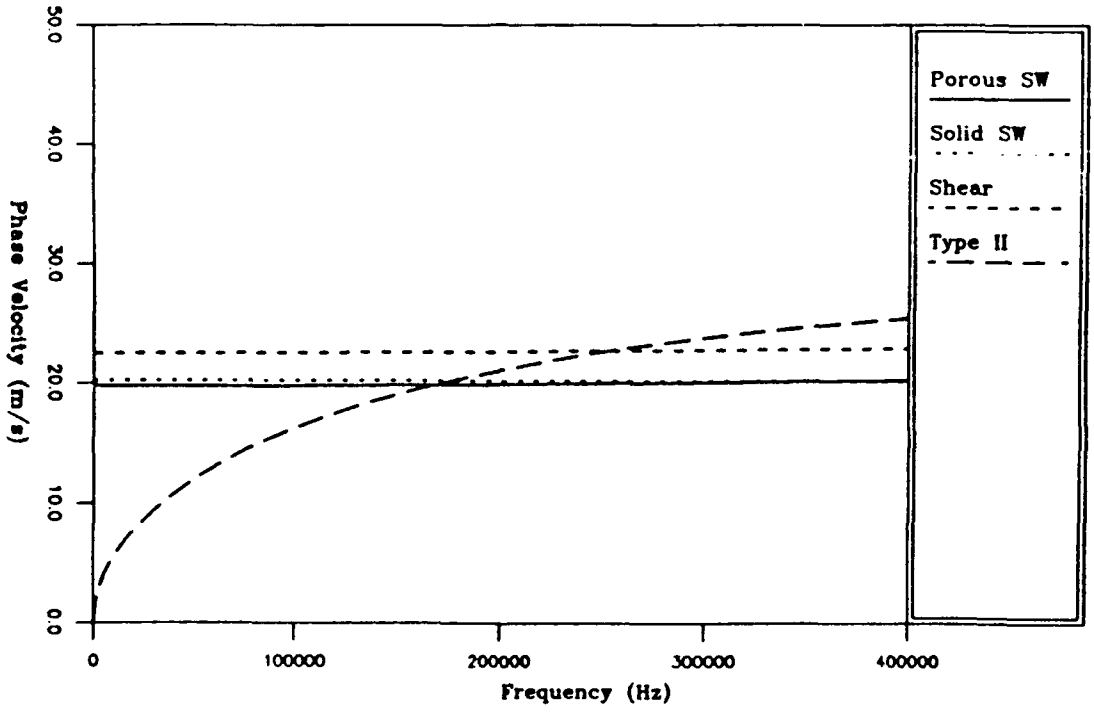

Figure 3.18 Phase velocity of various wave types in silty clay; pseudo-Scholte wave at a fluid-poro-viscoelastic boundary (porous SW); pseudo-Scholte wave at a fluid-viscoelastic boundary (solid SW); shear wave in a poro-viscoelastic sediment (shear); and Type II wave in a poro-viscoelastic sediment (Type II).

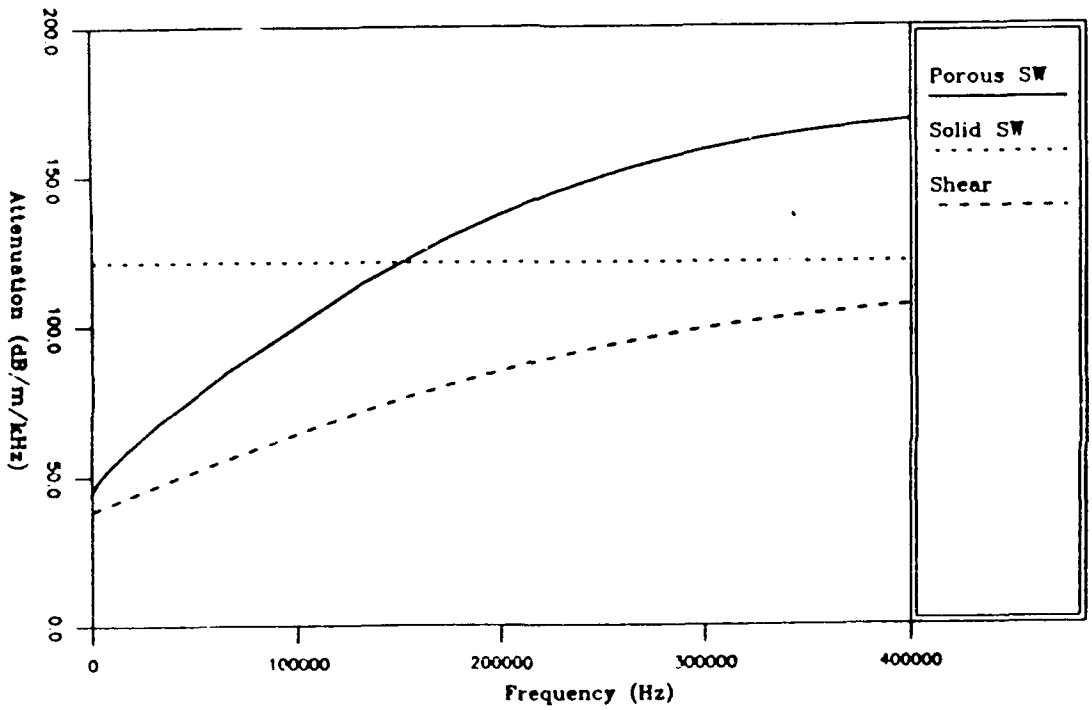

Figure 3.19 Attenuation of various wave types in silty clay; pseudo-Scholte wave at a fluid-poro-viscoelastic boundary (porous SW); pseudo-Scholte wave at a fluid-viscoelastic boundary (solid SW); and shear wave in a poro-viscoelastic sediment (shear).

3.4.3 Sandstone: $V_p > V_o$, $V_s > V_o$

For this sediment ($V_s > V_o$), both the pseudo-Scholte wave and the pseudo-Rayleigh wave exist. For both the pseudo-Scholte (Figures 3.20 and 3.21) and the pseudo-Rayleigh (Figures 3.22 and 3.23) surface wave types, the single-phase approximation is reasonable for the velocity but quite poor for the attenuation.

There is some difficulty associated with assigning a wave speed and attenuation to the pseudo-Rayleigh wave. Consider two studies of a fluid-solid boundary with surface waves excited from an impulsive source. Van der Hijden (1984) states that "from a mathematical point of view it is not appropriate to associate with [V_{surf}] a pseudo-Rayleigh wave speed because there is no wave front associated with this phenomenon." He considers the possibility of using the true Rayleigh wave speed (calculated as if a vacuum replaced the fluid) to describe the velocity of a pulse and attributing the change in shape of the pulse to some dispersive property. He opts instead to use V_{surf} as the "pseudo-Rayleigh travel speed" which describes the speed of the pulse maximum. Roever et al. (1959) on the other hand demonstrate experimentally and theoretically that the zero-crossing of a pseudo-Rayleigh wave does travel along the boundary at precisely the Rayleigh wave velocity; that is independent of the fluid properties! Roever et al. (1959) indicate, however, that the zero crossing of a pseudo-Rayleigh wave excited by a time harmonic source does travel at V_{surf} (i.e., is influenced by the properties of the upper halfspace). Since this study considers the response of the boundary of a time harmonic source, Figures 3.22 and 3.23 represent solutions to the secular equation accounting for the properties of the upper halfspace.

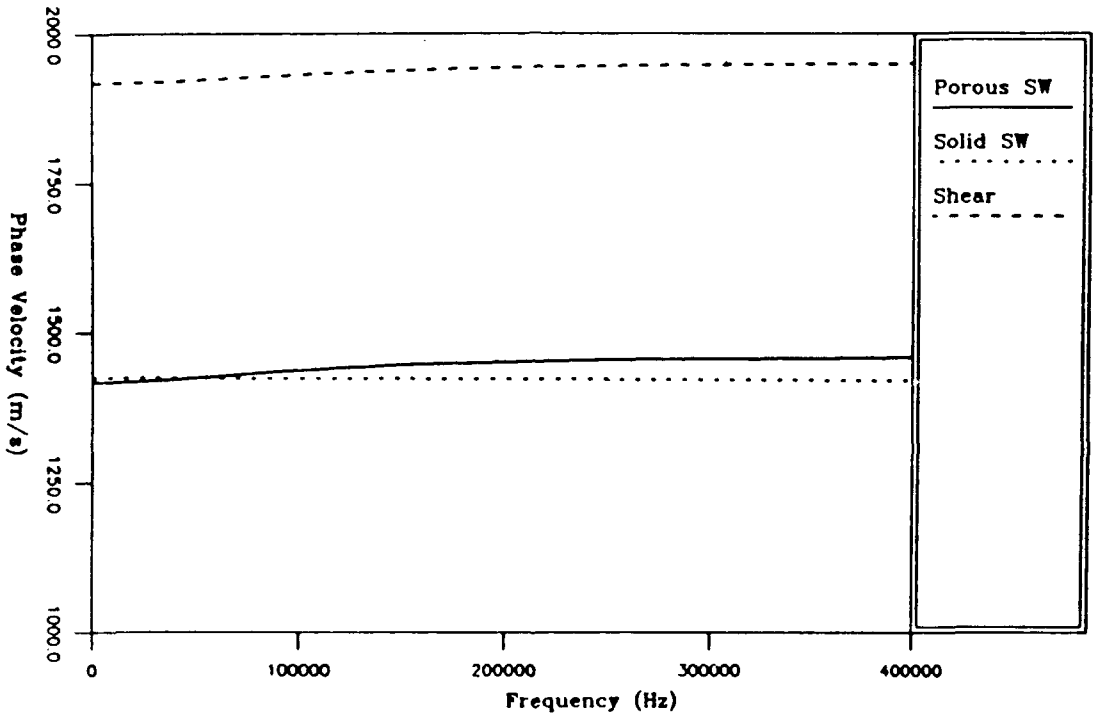

Figure 3.20 Phase velocity of various wave types in sandstone. Pseudo-Scholte wave at a fluid-poro-viscoelastic boundary (porous SW); pseudo-Scholte wave at a fluid-viscoelastic boundary (solid SW); and shear wave in a poro-viscoelastic sediment (shear).

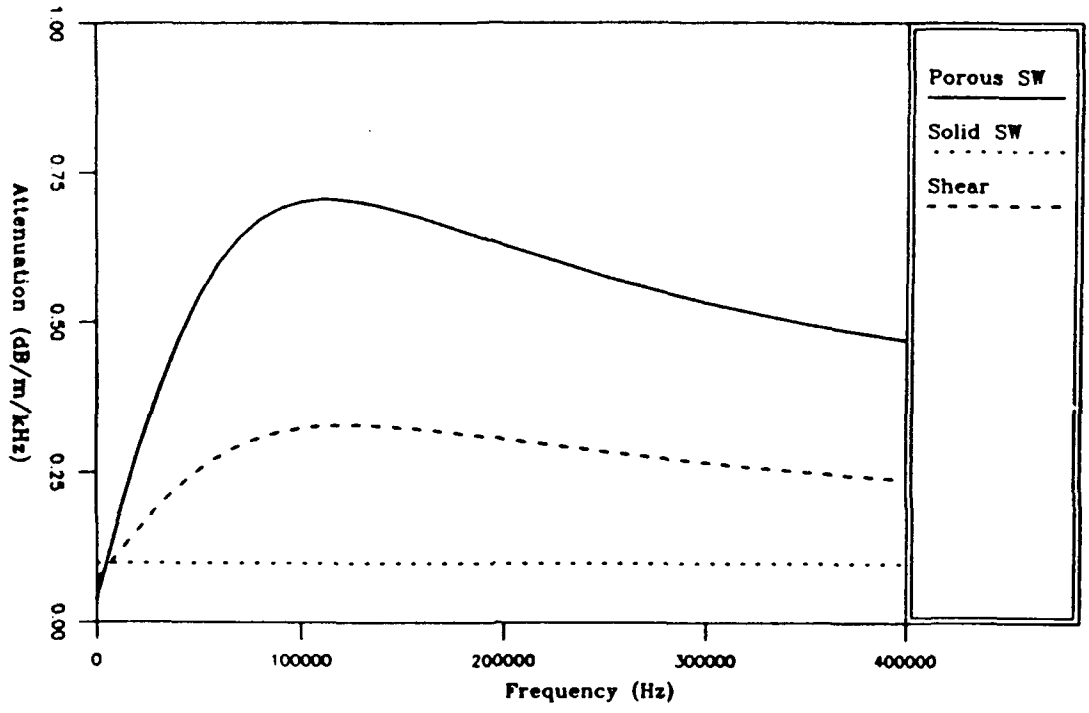

Figure 3.21 Attenuation of various wave types in sandstone; pseudo-Scholte wave at a fluid-poro-viscoelastic boundary (porous SW); pseudo-Scholte wave at a fluid-viscoelastic boundary (solid SW); and shear wave in a poro-viscoelastic sediment (shear).

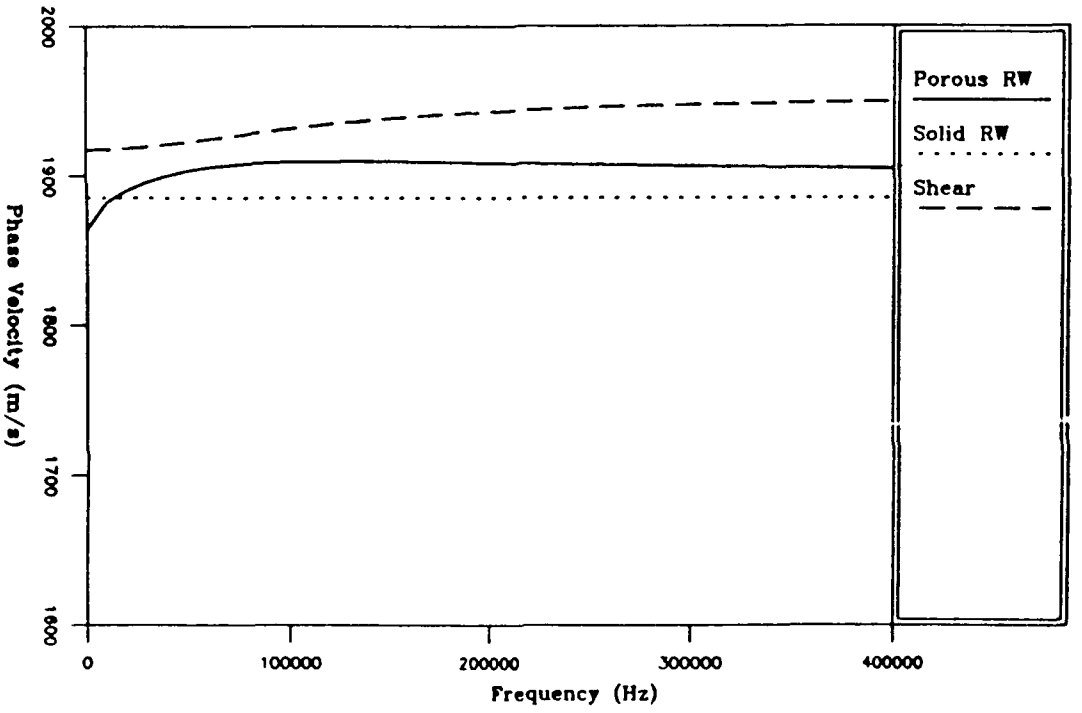

Figure 3.22 Phase velocity of various wave types in sandstone. Pseudo-Rayleigh wave at a fluid-poro-viscoelastic boundary (porous RW); pseudo-Rayleigh wave at a fluid-viscoelastic boundary (solid RW); and shear wave in a poro-viscoelastic sediment (shear).

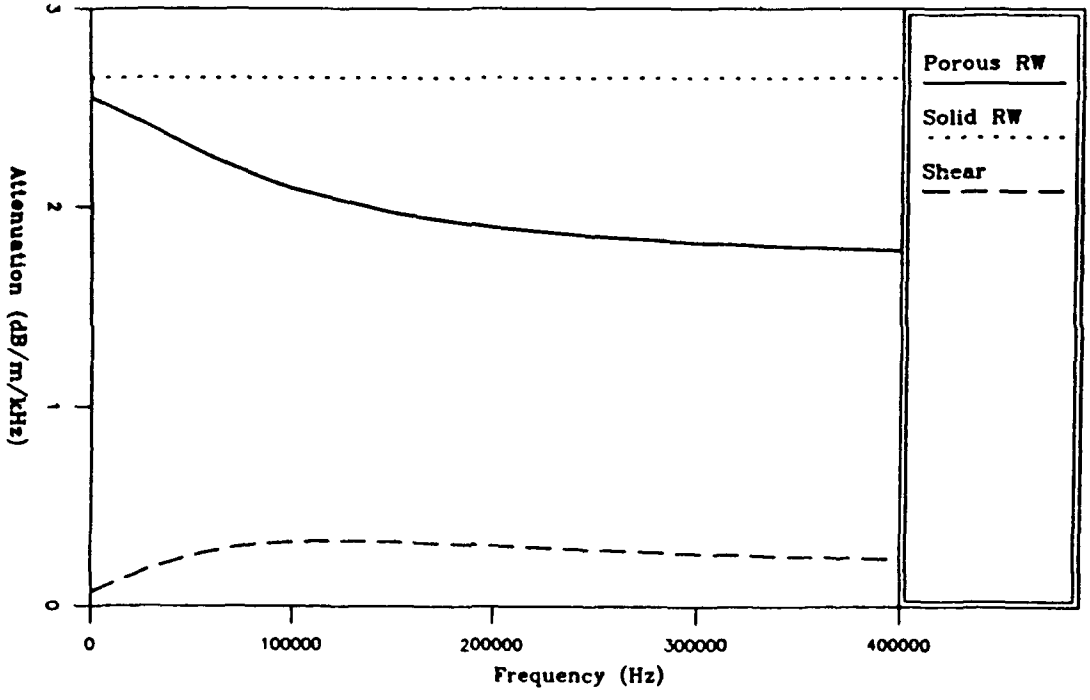

Figure 3.23 Attenuation of various wave types in sandstone; pseudo-Rayleigh wave at a fluid-poro-viscoelastic boundary (porous RW); pseudo-Rayleigh wave at a fluid-viscoelastic boundary (solid RW); and shear wave in a poro-viscoelastic sediment (shear).

3.5 Summary and Conclusions

In this chapter, plane wave coefficients for fluid-fluid, fluid-viscoelastic, and fluid-poro-viscoelastic boundaries were compared. Biot theory predicts frequency dependent plane wave reflection (and transmission) coefficients as compared with the frequency independent coefficients predicted using single-phase fluid or viscoelastic theories.

For the sand case the critical frequency (Eq. 2.67) was low enough to be in the frequency range of interest. Therefore, the velocity and attenuation of each wave type (especially the Type I wave which is the most important wave influencing reflectivity for this sediment type) varied non-linearly over the band of interest leading to the frequency dependent plane wave coefficients. For the silty clay case the critical frequency was high enough that the velocity of the Type I wave (the only wave participating strongly in the reflection and transmission process) was nearly constant with frequency and the attenuation was slightly non-linear with frequency. The reflection coefficient was independent of frequency over the 10 Hz - 10 kHz band. For the sandstone case, the velocities of the Type I and shear waves were only weakly dispersive. From previous results this suggests that the plane wave coefficients should exhibit only a weak frequency dependence. In this case, however, the velocity dispersion of the Type II significantly influenced the plane wave coefficients at high frequency.

In attempting then to specify criteria for when the single-phase models may be substituted for the full theory, two factors must be taken into account: 1) the frequency dependence of the plane wave coefficients (arising from the frequency dependence of the complex wave velocities) and 2) the role of the Type II waves.

First consider the frequency dependence. It is the critical frequency that determines whether or not the full Biot theory is required for predicting energy balance at the seafloor. If the critical frequency for a particular sediment type is well outside the frequency band of interest, then a single phase model will give a good approximation to the reflection

coefficient. If the critical frequency (Eq. (2.67)) is near the frequency band of interest, however, the complex wave velocities will vary substantially across that band and the full Biot theory will be required. This last conclusion presupposes that the reflection equation will be sensitive to the frequency dependence of at least one of the three wave speeds predicted by Biot theory. While this may not be true for an arbitrary fluid- porous material interface, it is expected to be true for the ranges of interface types found at the seafloor. A word is in order here regarding the phrase: "frequency band of interest". Certainly it refers to the frequencies over which the acoustic measurements were taken. However, if geoacoustic properties were measured on core samples at high frequencies, the "frequency band of interest" referred to in the above criterion must be expanded to include these frequencies. It was shown that the traditional extrapolation of geoacoustic properties from core data can lead to erroneous results (at least with respect to Biot theory) when the critical frequency is between the measurement bands of the acoustic data and the geoacoustic data.

The second factor: the role of the Type II wave is somewhat simpler. The Type II waves are only important to reflection/transmission at high frequencies where they are propagatory: "high frequencies" roughly corresponds to frequencies above the critical frequency.

The surface waves arising at a fluid-poro-viscoelastic boundary were also examined and compared with the classical single-phase solid approximation. The single phase solid approximation provided a reasonable approximation to the surface wave phase velocity (as predicted by Biot theory) for all three sediment types, however, in all cases neither the magnitude nor the frequency dependence of the attenuation was adequately predicted.

Chapter 4

THEORY II - INVERSE TRANSFORM

In this chapter the integral expressions for the field quantities in the upper and lower halfspace are evaluated by a "mixed" approach, a numerical integration and by the Fast Fourier Transform (FFT). The mixed approach consists of breaking the field into components representing, for example, contributions from the direct wave, the reflected/transmitted geometrical optics wave, and the various head and surface waves. Results from the mixed approach and the FFT are compared to examine the bounds of applicability for each.

4.1 Mixed Approach

4.1.1. Field in Upper Halfspace

The expression for the pressure field in the upper halfspace is obtained by Fourier Transforming Eq. (2.17):

$$p(x,z\geq 0) = -\frac{i\rho_0\omega^2}{4\pi}\int_{-\infty}^{\infty}\left\{e^{-i\alpha|z-h|}+\Re e^{-i\alpha z}\right\}\alpha^{-1}e^{-ik_x x}dk_x \tag{4.1}$$

where the first term corresponds to the direct field and the second term to the reflected field. The reflected field can be conveniently decomposed into (1) a contribution from plane waves reflected at the interface near angles predicted by Snell's law (the geometrical ray term); (2) a contribution from head waves (arising from branch points in the reflection factor $\Re$); and (3) a contribution from surface waves (arising from poles in $\Re$) . Each of these contributions will be considered separately in the following sections.

4.1.1.1 The Direct Field

The integral expression for the direct field can be solved exactly:

$$p_d(x,z\geq 0)=\frac{1}{4}\rho_o\omega^2 H_o^{(2)}\left(k_o\left[x^2+(z-h)^2\right]^{1/2}\right) \tag{4.2}$$

which represents an outgoing cylindrical wave radiated from the line source.

4.1.1.2 Reflected Field (Geometrical Ray Path)

The integral expression for the reflected field is

$$p_r(x,z\geq 0)=\frac{-i\rho_o\omega^2}{4\pi}\int_{-\infty}^{\infty}\Re e^{-i\left(k_o^2-k_x^2\right)^{1/2}(z+h)}\left(k_o^2-k_x^2\right)^{-1/2}e^{-ik_x x}dk_x \tag{4.3}$$

where the plane wave reflection coefficient has been substituted for the reflection factor using Eq. (3.8). Making the transformation, $k_x = k_o \sin\theta$, and employing the coordinate system (see Figure 4.1): $x = s \sin\theta_o$ and $z+h = s \cos\theta_o$, Eq. (4.3) can be written:

$$p_r(x,z\geq 0)=\frac{-i\rho_o\omega^2}{4\pi}\int_{\frac{-\pi}{2}-i\infty}^{\frac{\pi}{2}+i\infty}\Re e^{-ik_o s\cos(\theta-\theta_o)}d\theta \tag{4.4}$$

The method of steepest descent is employed to evaluate this integral. The method considers integrals of the form

$$I=\int_c F(\theta)e^{\rho f(\theta)}d\theta \tag{4.5}$$

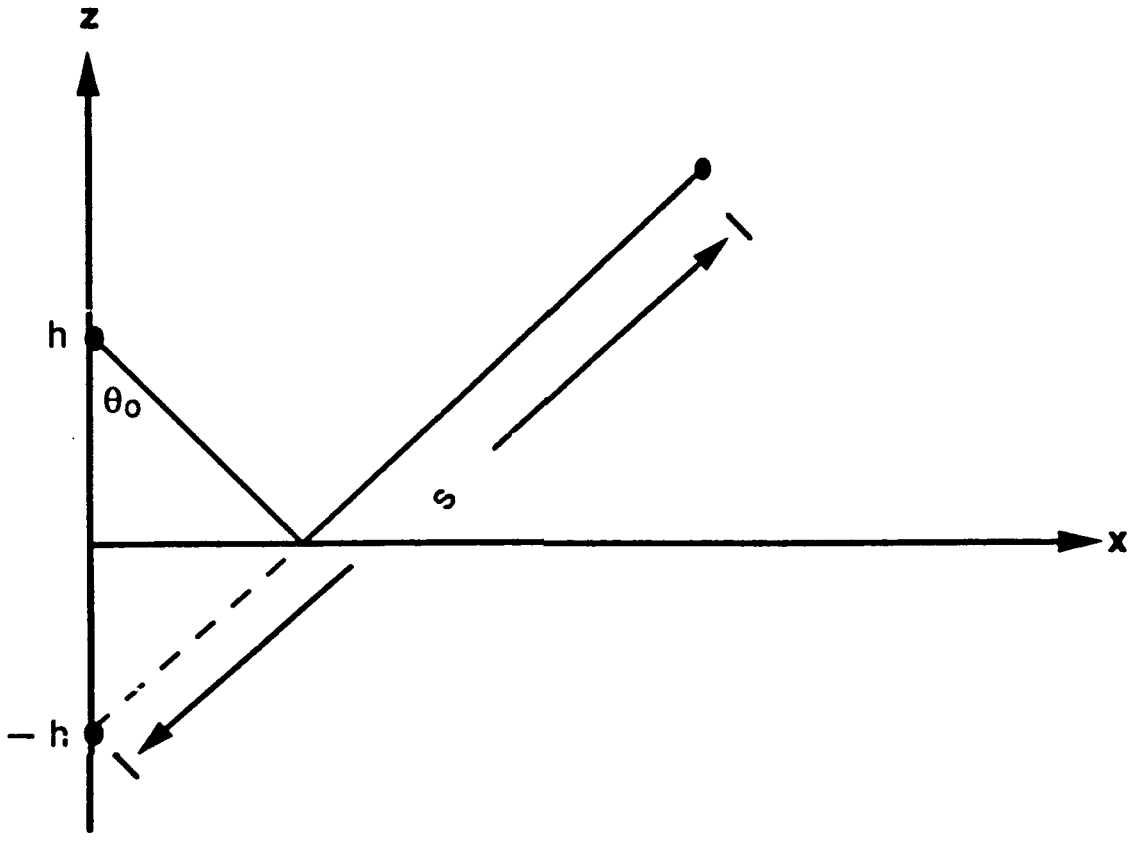

Figure 4.1 Coordinate system for the reflected field,'h' is the source height.

in the complex plane, where $F(\theta)$ must be a slowly varying function of θ. The technique consists of finding the saddle point of the function $f(\theta)$ and the path along which the function decreases most rapidly. The original path of integration is then deformed along that path and the integrand is expanded in a Taylor series around the saddle point. Since most of the contribution to the integral comes from near the saddle point, the function can be approximated by a few terms and the integral is evaluated term by term.

Letting $F(\theta) = \overline{\Re}$, $\rho = k_o s$, and $f(\theta) = -i \cos(\theta - \theta_o)$, the saddle point, θ_{sp}, is defined at $f'(\theta) = 0$ which gives

$$\theta_{sp} = \theta_o \tag{4.6}$$

Thus, the saddle point is simply located at the angle of incidence corresponding to the geometrical ray path and is real for real velocity V_o, varying from 0 to $\pi/2$ radians. The path of steepest descent is defined where the imaginary part of $f(\theta)$ is constant,

$$\mathrm{Im}\{f(\theta)\} = \mathrm{Im}\{f(\theta_{sp})\} \tag{4.7}$$

or

$$\mathrm{Re}\{\cos\theta\cos\theta_o + \sin\theta\sin\theta_o\} = 1 \tag{4.8}$$

Letting $\theta = \theta^R + i\theta^I$ the path of steepest descent is defined by,

$$\cosh\theta^I \cos(\theta^R - \theta_o) = 1 \tag{4.9}$$

In Figure 4.2, the complex θ plane is shown with the original path of integration, the saddle point, the steepest descent path, and the branch cuts associated with each wave type. Note that there is no fluid wave branch cut because of the choice of transformation; that is, $\alpha = k_0 \cos\theta$ and is no longer discontinuous. The branch cuts are placed for the marine sand case ($V_p > V_0$, $V_s < V_0$, $V_2 < V_0$). By Cauchy's theorem the path of integration in the complex plane may be deformed arbitrarily without changing the value of the integral provided that the end points are not deformed and no singularities are crossed from one path to the other. Taking the first term of the Taylor series (Brekovskikh (1980), Eq. 27.9) we have

$$p_r(\theta_0) \simeq \frac{-i}{4} \rho_0 \omega^2 \left[\frac{2}{\pi k_0 s}\right]^{1/2} e^{-i\left(k_0 s - \pi/4\right)} \overline{\mathfrak{R}}(\theta_0) \tag{4.10}$$

Since the Taylor series is expanded in orders, $1/k_0 s$, Eq (4.10) is a high-frequency, far-field approximation, and is valid for $k_0 s >> 1$. The region of validity is also restricted by the approximation of a slowly varying $\overline{\mathfrak{R}}(\theta_0)$, so that Eq (4.10) will not be valid near pseudo-critical angles or angles of pseudo-intromission. Writing the asymptotic representation of the Hankel function as

$$H_0^{(2)}(k_0 s) \equiv \left[\frac{2}{\pi k_0 s}\right]^{1/2} e^{-i\left(k_0 s - \frac{\pi}{4}\right)} \left(1 + \frac{i}{8 k_0 s} + \ldots\right) \tag{4.11}$$

the expression in Eq (4.10) for the reflected pressure can be considered to represent an outgoing cylindrical wave at the image source, modified by the plane wave reflection coefficient, to first order.

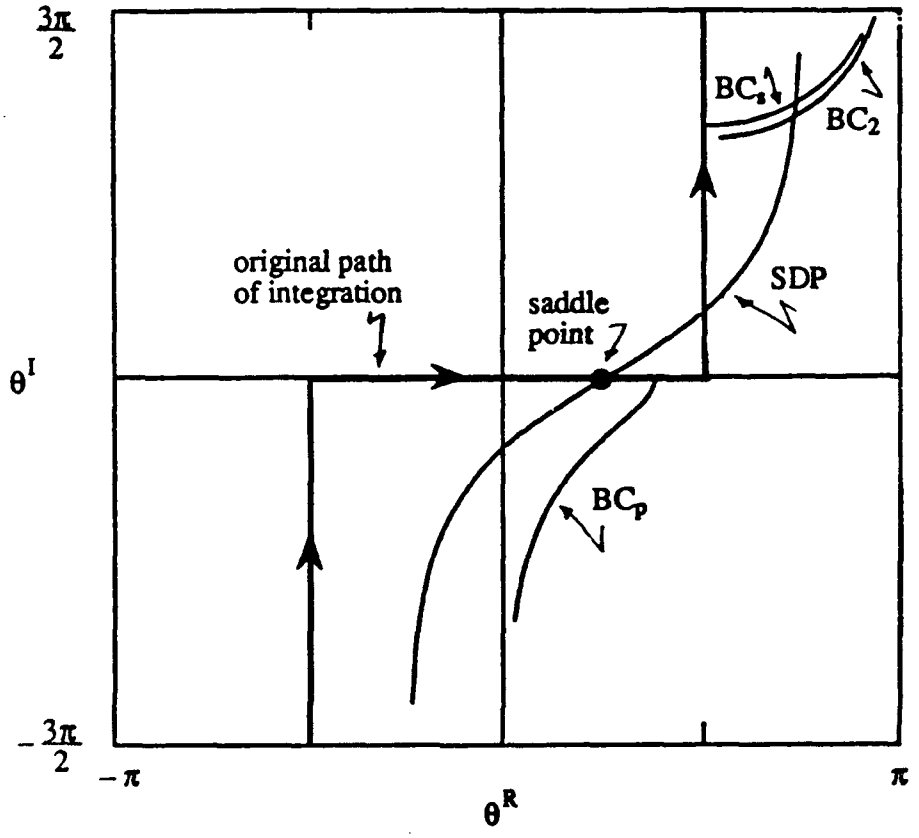

Figure 4.2 Complex θ plane for the reflected field showing the original contour; the saddle point ;the steepest descent path (SDP); and the Type I, Type II, and shear wave branch cuts (BC_p, BC_2, and BC_s respectively).

4.1.1.3 Reflected Field (Head Waves)

When the angle of incidence becomes such that the steepest descent path crosses over a branch point, the path starts and ends on different Reimann sheets. Cauchy's theorem for deforming paths is then violated since at one end point the original end point is on the upper sheet and the steepest descent path is on the lower sheet. In order to remedy this situation the path of steepest descent may be deformed as in Figure 4.3 following Brekovskikh (1980) where the path around the branch cut gives the head wave contribution and the rest of the path yields the reflected field approximated by Eq (4.10).

1. Type I Waves

Considering just the contribution from the head wave field arising from the Type I wave branch point we have that

$$p_{hp}(x,z\geq 0)=\frac{-i\rho_o\omega^2}{4\pi}\left[\int_{-i\infty}^{\theta_{pc}}\overline{\Re_{p+}}\,e^{-ik_o s\cos(\theta-\theta_o)}d\theta+\int_{\theta_{pc}}^{-i\infty}\overline{\Re_{p-}}\,e^{-ik_o s\cos(\theta-\theta_o)}d\theta\right] \tag{4.12}$$

where $\overline{\Re}_{p+}$ is the reflection coefficient on the left edge of the cut where the real part of $(k^2_p - k_x^2)^{1/2}$ is positive and the $\overline{\Re}_{p-}$ is the reflection coefficient on the right side where the real part of the root is negative. Along the branch cut, $\mathrm{Im}\{(k_p^2 - k_x^2)^{1/2}\} = 0$. Combining the limits of integration

$$p_{hp}(x,z\geq 0)=\frac{-i\rho_o\omega^2}{4\pi}\int_{-i\infty}^{\theta_{pc}}\left(\overline{\Re}_{p+}-\overline{\Re}_{p-}\right)e^{-ik_o s\cos(\theta-\theta_o)}d\theta \tag{4.13}$$

This expression can be evaluated by numerical integration and the simplest way of numerically treating the contour is to transform the equation back to the k_x plane such that the path of integration becomes a straight line;

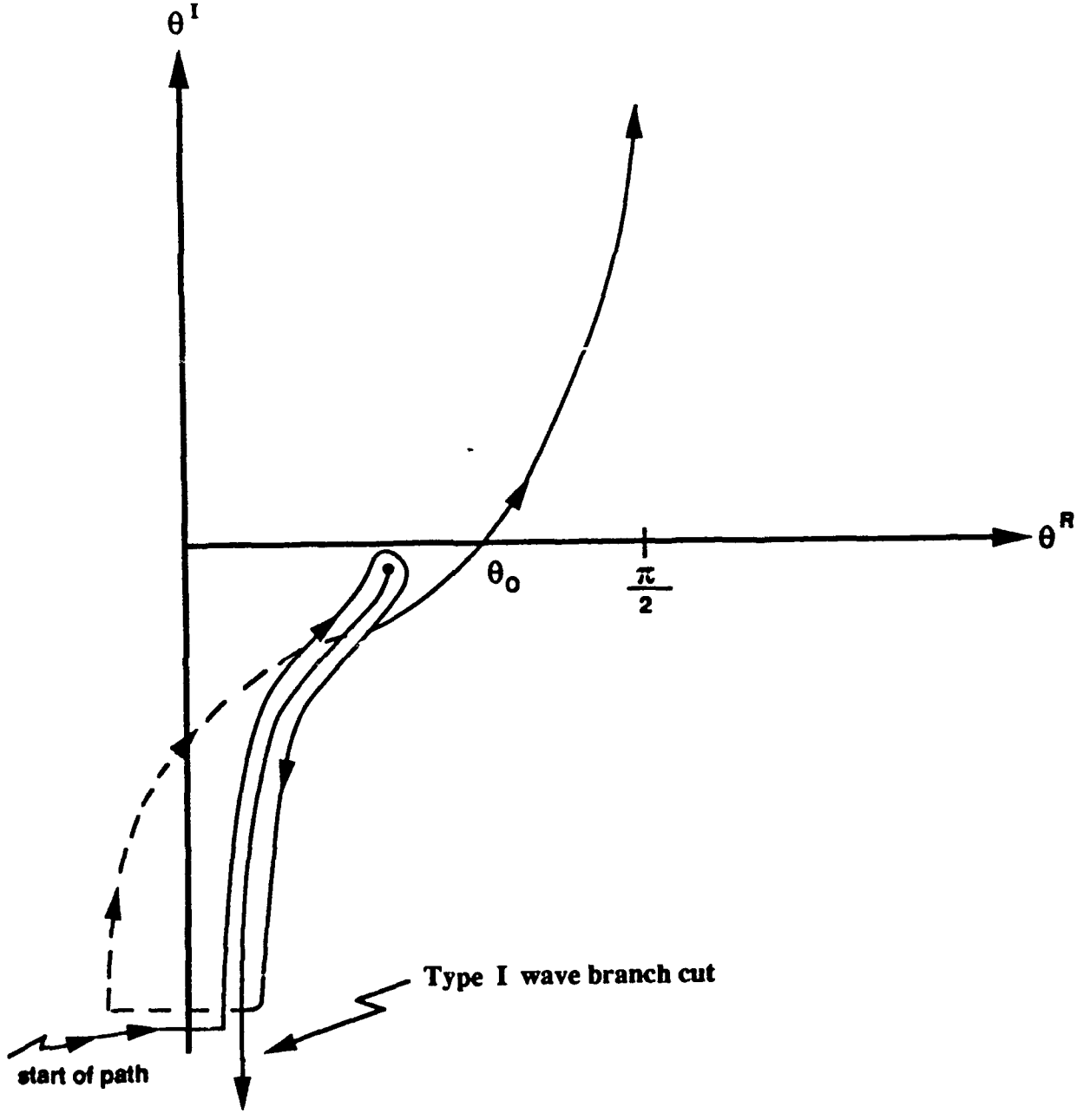

Figure 4.3 Deformation of steepest descent path around the Type I wave branch cut. The dotted portion of the path is on the lower Reimann sheet.

$$p_{hp}(x,z\geq 0)=\frac{-i\rho_o\omega^2}{4\pi}\int_{-i\infty+k_p}^{k_p}\left(\overline{\Re}_{p+}-\overline{\Re}_{p-}\right)e^{-i\left(k_o^2-k_x^2\right)^{1/2}(z+h)}\left(k_o^2-k_x^2\right)^{-1/2}e^{-ik_x x}dk_x \tag{4.14}$$

Thus far, the generation of head waves for the case where the Type I wave velocity is greater than the upper halfspace velocity has been considered ($V_p > V_o$). This is the wave used in seismic refraction methods to estimate sub-seafloor layer velocities (see, for example, Clay and Medwin (1977)). We now consider the case $V_p < V_o$ which results in moving the branch point (and cut) from the fourth to the second quadrant of the complex θ plane. When the path of steepest descent crosses the branch cut, the path can be deformed as before around the cut, and the head wave contribution is again obtained by Eq (4.13). For this case the head wave is exponentially damped away from the boundary. The pseudo-critical angle is complex and greater than $\pi/2$ when $V_p < V_o$ and is obtained by Eq. (3.3).

2. Type II and Shear Waves

There is also a Type II head wave for both cases: $V_2 > V_o$, and $V_2 < V_o$. The derivation of the field is entirely analogous to the derivation for compressional waves so that

$$p_{h2}(x,z\geq 0)=\frac{-i\rho_o\omega^2}{4\pi}\int_{-i\infty+k_2}^{k_2}\left(\overline{\Re}_{2+}-\overline{\Re}_{2-}\right)e^{-i\left(k_o^2-k_x^2\right)^{1/2}(z+h)}\left(k_o^2-k_x^2\right)^{1/2}e^{-ik_x x}dk_x \tag{4.15}$$

and the steepest descent path first crosses the Type II wave branch cut at $\cosh\theta^I_{pc2}\cos(\theta^R_{pc2}-\theta_o)=1$, where

$$\theta_{pc2}=\sin^{-1}\left[\frac{\mathrm{Re}\{k_2\}}{\mathrm{Re}\{k_o\}}\right].$$

The contribution from the shear wave is likewise given for both $V_s > V_o$ and $V_s < V_o$ as

$$p_{hs}(x,z \geq 0) = \frac{-i\rho_o\omega^2}{4\pi} \int_{-i\infty+k_s}^{k_s} \left(\overline{\mathfrak{R}}_{s+} - \overline{\mathfrak{R}}_{s-}\right) e^{-i\left(k_o^2-k_x^2\right)^{1/2}(z+h)} \left(k_o^2 - k_x^2\right)^{-1/2} e^{-ik_x x} dk_x \tag{4.16}$$

and the steepest descent path first crosses the shear wave branch cut at $\cosh \theta^I_{pcs} \cos(\theta^R_{pcs} - \theta_o) = 1$ where θ_{pcs} is given in Eq (3.7). The shear and Type II head waves decay exponentially away from the boundary when the velocity is less than the upper halfspace.

4.1.1.4 Reflected Field (Surface Waves)

When the angle of incidence becomes such that the steepest descent path crosses over a pole (or poles) of the integrand Cauchy's theorem requires that the sum of the residues of the pole(s) (times $2\pi\ i$) be added to the field. The physical meaning of this contribution is the phenomenon of surface waves. The poles arise from the denominator of the reflection coefficient. The surface wave field can be written for a single pole as:

$$p_{surf}(\theta_o) = \frac{\rho_o\omega^2}{2} \text{res}\left\{\overline{\mathfrak{R}}(\theta)\right\} \left[e^{-ik_o s\cos(\theta-\theta_o)} \Big|_{\theta=\theta_{pole}} \right] \tag{4.17}$$

or in terms of Cartesian coordinates

$$p_{surf}(x,z) = \frac{\rho_o\omega^2}{2} \text{res}\left\{\overline{\mathfrak{R}}(k_x)\right\} \left[\frac{e^{-i\left(k_o^2-k_x^2\right)^{1/2}(z+h)}}{\left(k_o^2-k_x^2\right)^{1/2}} \right] e^{-ik_x x} \Big|_{k_x=k_{pole}} \tag{4.18}$$

where

$$\mathrm{res}\left\{\overline{\Re}(\theta)\right\} = \mathrm{res}\left\{\overline{\Re}(k_x)\right\}\left(k_o^2 - k_x^2\right)^{-1/2}$$

and the spatial dependence of the field is contained within the square brackets. For a simple pole

$$\mathrm{res}\left\{\overline{\Re}(\theta)\right\} = \frac{A_-(\theta)}{A_+'(\theta)}, \text{ where } \overline{\Re}(\theta) = \frac{A_-(\theta)}{A_+(\theta)} \tag{4.19}$$

and the prime denotes a derivative with respect to the argument. There is no loss due to geometrical spreading expressed in Eq (4.17, 4.18) since the solution is confined to one horizontal dimension (surface waves spread in two horizontal dimensions). The intrinsic absorption in the horizontal dimension is given by the term $\exp(k^I x)$ where k^I is the imaginary part of the surface wave wavenumber.

The location of the surface wave poles as a function of frequency for sand, silty clay, and sandstone is shown in Figures 4.4 - 4.6, respectively. For each sediment type the pole is located close to 90° on the real axis and the position on the imaginary axis is strongly a function of sediment type. From Figure 4.2 we see that the path of steepest descent will cross the silty clay surface wave pole even for modest angles of incidence. A larger angle of incidence is required for the sand surface wave pole to be crossed and yet larger for the sandstone surface wave pole.

4.1.2 Field in Lower Halfspace

For the field in the lower halfspace we must first choose the quantity of interest. The most common measuring device used in the seafloor is a geophone (that measures displacement) and recently in the underwater acoustics community several experimenters have employed a hydrophone (that measures the pressure field).

The pressure field in the interstitial fluid is given by Eq. (2.25). Using the expression for **u** and **w** in Eq. (2.65) and Eq. (2.66)

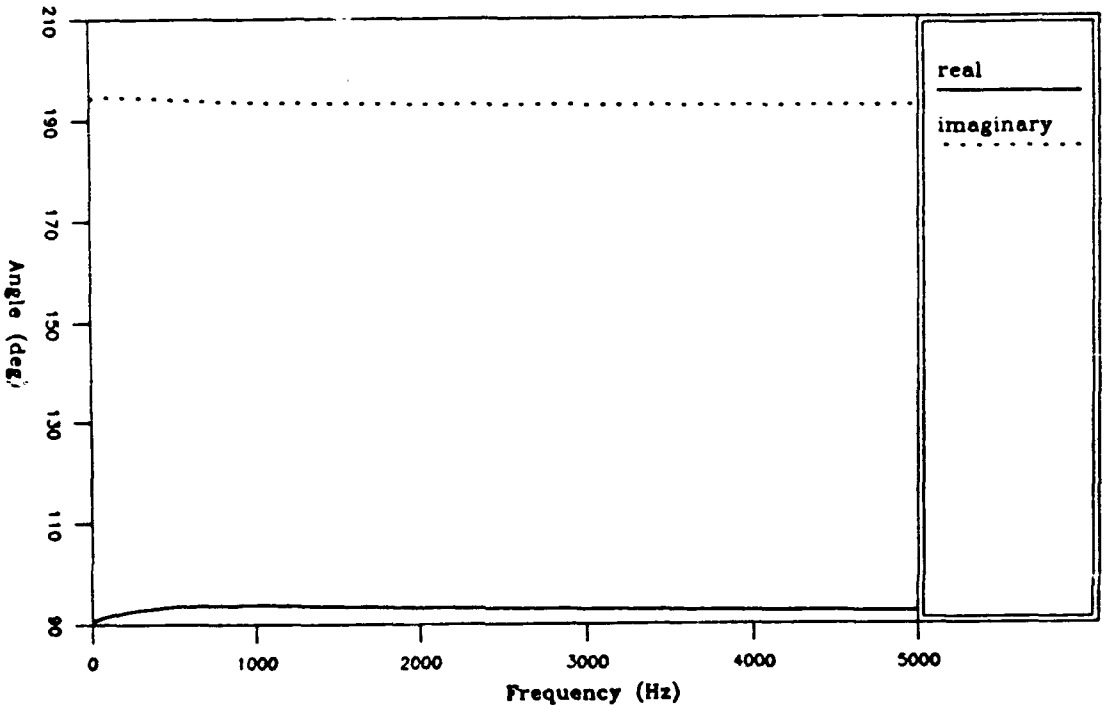

Figure 4.4 Pseudo-Scholte wave pole location in the Complex Angle Plane for Sand.

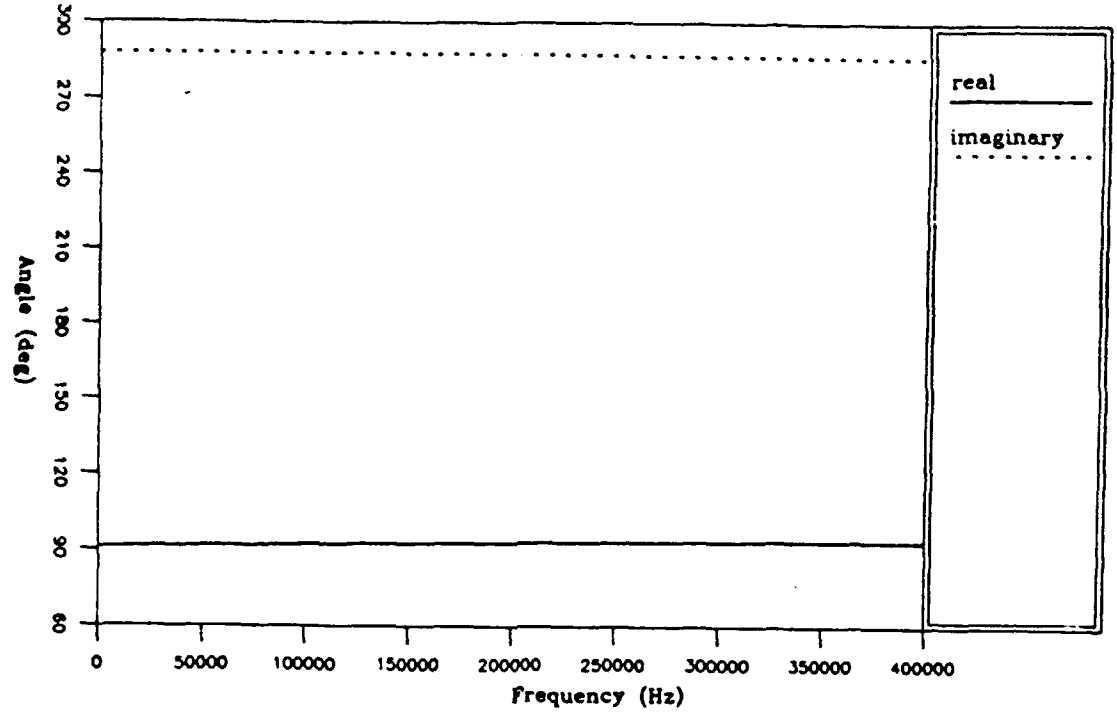

Figure 4.5 Pseudo-Scholte wave pole location in the Complex Angle Plane for Silty Clay.

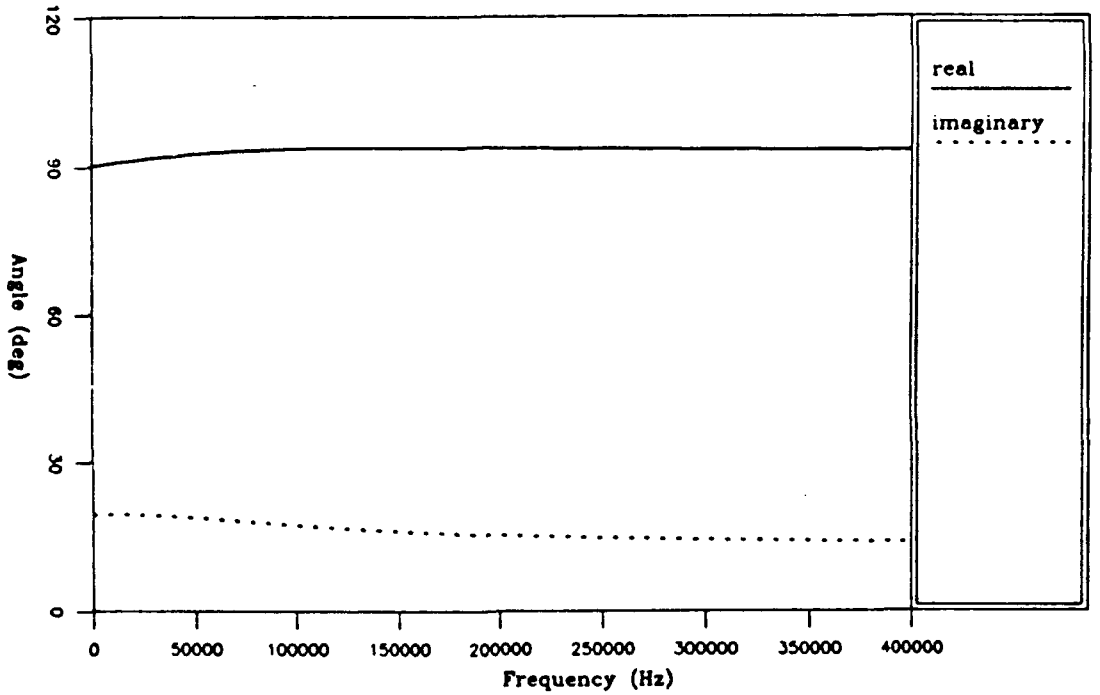

Figure 4.6 Pseudo-Scholte wave pole location in the Complex Angle Plane for Sandstone.

$$p(x,z\le 0)=\frac{i}{4\pi}\int_{-\infty}^{\infty}\left[k_p^2\left(MG_p-C\right)\bar{T}_p e^{i\alpha_p z}+k_2^2\left(MG_2-C\right)\bar{T}_2 e^{i\alpha_2 z}\right]\frac{e^{-i(\alpha h+k_x x)}}{\alpha}dk_x$$

(4.20)

The total displacement field **D** is given by $\mathbf{D}=\mathbf{u}+\mathbf{U}=2\,\mathbf{u}-\mathbf{w}/\beta$ or :

$$\mathbf{D}=\frac{1}{4\pi}\int_{-\infty}^{\infty}\Big|a_1\left\{k_x\bar{T}_p e^{i\alpha_p z}\left(2-G_p/\beta\right)+k_x\bar{T}_2 e^{i\alpha_2 z}\left(2-G_2/\beta\right)+\alpha_s\bar{T}_s e^{i\alpha_s z}\left(2-G_s/\beta\right)\right\}+$$

$$a_3\left\{\alpha_p\bar{T}_p e^{i\alpha_p z}\left(-2+G_p/\beta\right)+\alpha_2\bar{T}_2 e^{i\alpha_2 z}\left(-2+G_2/\beta\right)+k_x\bar{T}_s e^{i\alpha_s z}\left(2-G_s/\beta\right)\right\}\Big]\times$$

$$\frac{e^{-i(\alpha h+k_x x)}}{\alpha}dk_x$$

(4.21)

The integral expressions for the transmitted pressure and displacement field will be evaluated in like manner as the reflected field by considering the contribution of each wave type separately including the geometrical ray path, the various head waves, and the surface waves.

4.1.2.1. Transmitted Field (Geometrical Ray Path)

In order to obtain the first-order contribution to the geometrical ray path, we proceed (as with the reflected field) to transform the integral to the complex θ plane. In the integral representation for the transmitted field consider the two square roots, $(k_o^2 - k_x^2)^{1/2}$

and $(k_p^2 - k_x^2)^{1/2}$ in the exponential. The latter square root suggests a complex angle transformation $k_x = k_p \sin\theta$. This transformation (by proper choice of coordinate system) will lead to an integrand commensurate with that for the reflected field except for a square root in the denominator $(k_o^2 - k_p^2 \sin\theta)^{1/2}$ giving rise to a pole (collocated with a branch point) in addition to the poles from the transmission coefficient $T_p(\theta)$. In order to avoid this singularity, the transformation $k_x = k_o \sin\theta$ is chosen. The next step is the choice of a suitable coordinate system, because the coordinate system influences the robustness of the asymptotic approximation. Candel and Crance (1981) show how the choice of a coordinate system centered at the source (as was done for the reflected field) yields a poor approximation to the transmitted field for geometrical ray paths near and above the critical angle. They suggest rather a system centered at a virtual source depicted in Figure 4.7 and defined by

$$x - x_p = s_p \sin\theta_p \tag{4.22}$$

$$z - z_p = -s_p \cos\theta_p$$

$$s_p = \left[(x - x_p)^2 + (z - z_p)^2 \right]^{1/2}$$

$$\theta_p = \sin^{-1}\left(\frac{V_p}{V_o} \sin\theta_o \right)$$

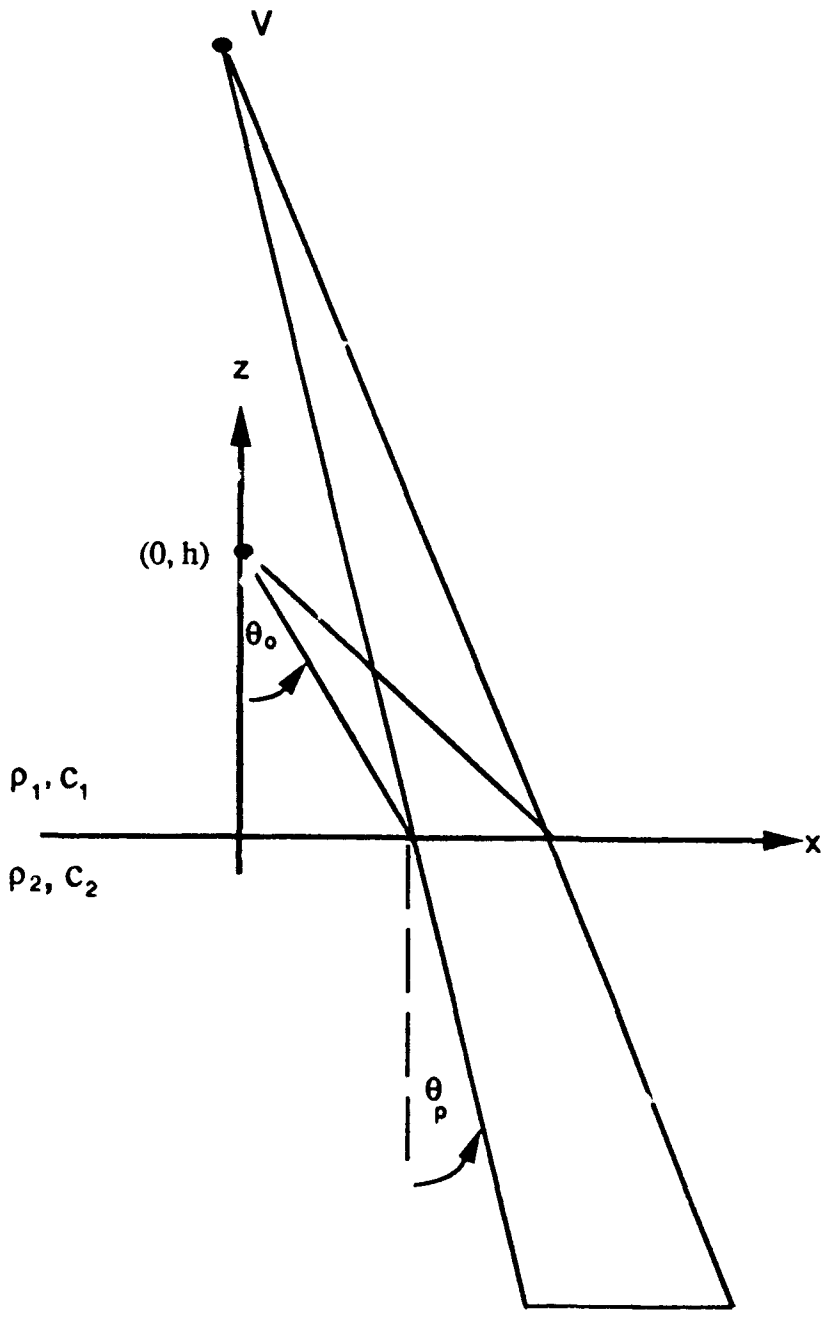

Figure 4.7 Coordinate system for the transmitted field. The true source height is "h" and the virtual source location is "v". For lossy media the virtual source coordinates are complex.

This coordinate system will be employed in the following. Unlike the Candel and Crance example, however, the lower halfspace of interest in this work is lossy (i.e. V_p is complex) such that angle of refraction, θ_p, and the reference lengths s_p, x_p, and z_p are all complex (see Appendix C).

Rewriting the first term of Eq. (4.20) now with the transformation $k_x = k_o \sin\theta$ and the coordinate system above, we have that

$$I_1 = \frac{i}{4\pi} k_p^2 \left(MG_p - C\right) \int_{\frac{-\pi}{2}-i\infty}^{\frac{\pi}{2}+i\infty} \overline{\mathcal{T}}_p(\theta) e^{i\left(k_p^2 - k_o^2 \sin^2\theta\right)^{1/2}\left(z_p - s_p\cos\theta_p\right)} \times$$

$$e^{-ik_o h\cos\theta} e^{-ik_o \sin\theta\left(s_p \sin\theta_p + x_p\right)} d\theta \qquad (4.23)$$

For the method of steepest descent let

$$\rho = k_o s_p$$

$$f(\theta) = -i\left\{\left(\frac{V_o^2}{V_p^2} - \sin^2\theta\right)^{1/2} \cos\theta_p + \sin\theta \sin\theta_p\right\}$$

$$F(\theta) = \overline{\mathcal{T}}_p(\theta)\, e^{i\left(k_p^2 - k_o^2 \sin^2\theta\right)^{1/2} z_p} e^{-ik_o\left(h\cos\theta + x_p \sin\theta\right)} \qquad (4.24)$$

The saddle point is then defined at

$$f'(\theta)\Big|_{\theta=\theta_{sp}} = 0 = \cos\theta\sin\theta_p - \sin\theta\cos\theta\left[\frac{V_o^2}{V_p^2} - \sin^2\theta\right]^{-1/2} \tag{4.25}$$

and with the relation (Snell's law) $\sin\theta_p = \frac{V_p}{V_o}\sin\theta_o$ the saddle point is

$$\theta_{sp} = \theta_o \,. \tag{4.26}$$

The saddle point for the transmitted field in this coordinate system is simply the angle of incidence corresponding to the geometrical ray path. There is a subtlety, however, that bears explication. The geometrical ray path (as shown in Figure 4.7) connects a ray in the upper medium traveling at real angle θ_o with a ray in the lower medium at real angle θ_{lp}. The real angle of transmission for a lossy medium is the angle associated with the real part of the wavevector which points perpendicular to the wavefronts and is given by

$$\theta_{lp} = \tan^{-1}\left[\sin\theta_o \Big/ \left(V_o\,\mathrm{Re}\left\{\left[1 - \frac{V_p^2}{V_o^2}\sin^2\theta_o\right]^{1/2} \Big/ V_p\right\}\right)\right] \tag{4.27}$$

while the angle of transmission, θ_p, associated with the virtual source in Eq. (4.22) is complex and given by Snell's law.

Now the steepest descent path is given by

$$\mathrm{Im}\{f(\theta)\}=\mathrm{Im}\left\{f\left(\theta_{sp}\right)\right\} \tag{4.28}$$

or

$$\mathrm{Re}\left\{\left(\frac{V_o^2}{V_p^2}-\sin^2\theta\right)^{1/2}\cos\theta_p+\sin\theta\sin\theta_p\right\}=\mathrm{Re}\left\{\frac{1}{V_p}\right\}V_o\,.$$

and at the saddle point,

$$f(\theta_o)=i\,V_o/V_p \tag{4.29}$$

$$f''(\theta_o)=i\frac{V_p\cos^2\theta_o}{V_o\cos^2\theta_p}\,. \tag{4.30}$$

therefore

$$I_1\cong\frac{i}{4\pi}k_p^2\left(MG_p-C\right)\sqrt{\frac{2\pi i V_o}{k_o s_p V_p}}\frac{\cos\theta_p}{\cos\theta_o}\bar{T}_p(\theta_o)e^{-ik_p\left(s_p-z_p\cos\theta_p\right)}e^{-ik_o\left(h\cos\theta_o+x_p\sin\theta_o\right)} \tag{4.31}$$

Thus from Eq. (4.20) we can write

$$p(x,z<0)=\frac{i}{4\pi}\left[k_p^2\left(MG_p-C\right)\sqrt{\frac{2\pi i V_o}{k_o s_p V_p}}\frac{\cos\theta_p}{\cos\theta_{op}}\bar{T}_p\left(\theta_{op}\right)e^{-i\psi_p}+\right.$$
$$\left.k_2^2\left(MG_2-C\right)\sqrt{\frac{2\pi i V_o}{k_o s_2 V_2}}\frac{\cos\theta_2}{\cos\theta_{o2}}\bar{T}_2\left(\theta_{o2}\right)e^{-i\psi_2}\right] \tag{4.32}$$

where

$$\theta_{op} = \sin^{-1}\left(\frac{V_o}{V_p}\sin\theta_p\right)$$

$$\theta_{o2} = \sin^{-1}\left(\frac{V_o}{V_2}\sin\theta_2\right)$$

$$\psi_i = k_i(s_i - z_i\cos\theta_i) + k_o(h\cos\theta_{oi} + x_i\sin\theta_{oi}) \qquad ; \quad i = p,2$$

Note that the two terms in Eq(4.32) represent two ray paths at two distinct angles. Thus for a porous medium, the first order predictions consist of two contributions as compared with the one contribution predicted by single phase theories.

For the displacement field:

$$\mathbf{D} = -\frac{1}{4\pi}a_1\Big\{(2-G_p/\beta)k_o\tan\theta_{op}\sqrt{\frac{2\pi i V_o}{k_o s_p V_p}}\cos\theta_{op}\,\overline{\tau}_p(\theta_{op})e^{-i\psi_p} +$$

$$(2-G_2/\beta)k_o\tan\theta_{o2}\sqrt{\frac{2\pi i V_o}{k_o s_2 V_2}}\cos\theta_2\,\overline{\tau}_2(\theta_{o2})e^{-i\psi_2} +$$

$$(2-G_s/\beta)k_s\cos\theta_s\sqrt{\frac{2\pi i V_o}{k_o s_s V_s}}\frac{\cos\theta_s}{\cos\theta_{os}}\overline{\tau}_s(\theta_{os})e^{-i\psi_s}\ \Big\} -$$

$$a_3\Big\{(2-G_p/\beta)k_p\cos\theta_p\sqrt{\frac{2\pi i V_o}{k_o s_p V_p}}\frac{\cos\theta_p}{\cos\theta_{op}}\overline{\tau}_p(\theta_{op})e^{-i\psi_p} +$$

$$(2-G_p/\beta)k_2\cos\theta_2\sqrt{\frac{2\pi i V_o}{k_o s_2 V_2}}\frac{\cos\theta_2}{\cos\theta_{o2}}\overline{\tau}_2(\theta_{o2})e^{-i\psi_2} -$$

$$(2-G_s/\beta)k_o\tan\theta_{os}\sqrt{\frac{2\pi i V_o}{k_o s_s V_s}}\cos\theta_s\,\overline{\tau}_s(\theta_{os})e^{-i\psi_s}\ \Big\}\Big] \qquad (4.33)$$

4.1.2.2 Transmitted Field (Head Waves)

As in the reflected field, the head wave contributions come from an integration around the branch cuts and are given by

(4.34)

$$p_{hp}(x,z\le 0)=\frac{i\rho_o\omega^2}{4\pi}\int_{-i\infty+k_p}^{k_p}\left[\frac{MG_p-C}{\rho_o V_p^2}\left(\bar{T}_{p_{p+}}e^{i\alpha_p z}-\bar{T}_{p_{p-}}e^{-i\alpha_p z}\right)+\frac{MG_2-C}{\rho_o V_2^2}\left(\bar{T}_{2_{p+}}-\bar{T}_{2_{p-}}\right)e^{i\alpha_2 z}\right]\frac{e^{-i(\alpha h+k_x x)}}{\alpha}\,dk_x$$

$$p_{h2}(x,z\le 0)=\frac{i\rho_o\omega^2}{4\pi}\int_{-i\infty+k_2}^{k_2}\left[\frac{MG_p-C}{\rho_o V_p^2}\left(\bar{T}_{p_{2+}}-\bar{T}_{p_{2-}}\right)e^{i\alpha_p z}+\frac{MG_2-C}{\rho_o V_2^2}\left(\bar{T}_{2_{2+}}e^{i\alpha_2 z}-\bar{T}_{2_{2-}}e^{-i\alpha_2 z}\right)\right]\frac{e^{-i(\alpha h+k_x x)}}{\alpha}\,dk_x \qquad (4.35)$$

$$p_{hs}(x,z\le 0)=\frac{i\rho_o\omega^2}{4\pi}\int_{-i\infty+k_s}^{k_s}\left[\frac{MG_p-C}{\rho_o V_p^2}\left(\bar{T}_{p_{s+}}-\bar{T}_{p_{s-}}\right)e^{i\alpha_p z}+\frac{MG_2-C}{\rho_o V_2^2}\left(\bar{T}_{2_{s+}}-\bar{T}_{2_{s-}}\right)e^{i\alpha_2 z}\right]\frac{e^{-i(\alpha h+k_x x)}}{\alpha}\,dk_x$$

(4.36)

The sub-subscripts refer to the sign of the vertical wavenumbers (α_p, α_2, α_s) which are real on their respective branch cuts; for example $\bar{T}_{p_{p+}}$ is the transmission coefficient for the Type I wave evaluated on the left-hand side of the Type I wave branch cut.

4.1.2.3 Transmitted Field (Surface Waves)

As in the reflected field, the transmitted field due to a surface wave can be written in terms of the residues of the simple poles of the plane wave coefficients. The poles for the transmitted field are identical (co-located) to those of the reflected field. For the pressure field we have:

$$p_{surf}(\theta_{pole}) = -\frac{1}{2}\Big[k_p^2(MG_p - C)\mathrm{res}\{\overline{T}_p(\theta)\}e^{i\left(k_p^2 - k_o^2\sin^2\theta\right)^{1/2}(z_p - s_p\cos_p)} \times$$

$$e^{-ik_o\left(h\cos\theta + \sin\theta(s_p\sin\theta_p + x_p)\right)} +$$

$$k_2^2(MG_2 - C)\mathrm{res}\{\overline{T}_2(\theta)\}e^{i\left(k_2^2 - k_o^2\sin^2\theta\right)^{1/2}(z_2 - s_2\cos\theta_2)} \times$$

$$e^{-ik_o\left(h\cos\theta + \sin\theta(s_2\sin\theta_2 + x_2)\right)}\Big]_{\theta=\theta_{pole}} \tag{4.37}$$

4.2 FFT Evaluation of Field Integrals

The expressions for the reflected and transmitted field are in the form of Fourier integrals such that the Fast Fourier Transform (FFT) method can be used for numerical solution of the field quantities. For example, the integral in Eq (4.3) can be approximated by a finite Reimann sum

$$p(x,z) = \frac{-i\rho_o\omega^2}{4\pi}\sum_{n=0}^{N-1}\frac{\overline{\mathfrak{R}}(k_{x_n})}{\left(k_o^2 - k_{x_n}^2\right)^{1/2}}e^{-i\left(k_o^2 - k_{x_n}^2\right)^{1/2}(z+h)}e^{-k_{x_n}x}dk_x \tag{4.38}$$

With the following conditions on x, k_x and spatial resolution Δx:

$$x_m = m\Delta x \quad m = 0,\ldots,N-1$$

$$k_{x_n} = n\Delta k_x \quad n = 0,\ldots,N-1$$

$$\Delta x = 2\pi / \Delta k_x N \tag{4.39}$$

we have that

$$p(x_m,z) = \frac{-i\rho_o\omega^2}{4\pi}\sum_{n=0}^{N-1}\left\{\frac{\overline{\Re}(n\Delta k_x)}{\left(k_o^2 - n^2\Delta k_x^2\right)^{1/2}}e^{-i\left(k_o^2-n^2\Delta k_x^2\right)^{1/2}(z+h)}\right\}e^{-i2\pi nm/N}\Delta k_x \tag{4.40}$$

This expression is a discrete Fourier transform of the function in curly brackets and may be calculated as an FFT.

In order to avoid spectral aliasing the sampling frequency $k_s = \Delta k_x N$ must be at least twice that of the highest frequency to be transformed. The local oscillation frequency, however, of Eq (4.3) is

$$\frac{d}{dk_x}\left\{-\left(k_o^2 - k_x^2\right)^{1/2}(z+h)\right\} = \frac{k_x(z+h)}{\left(k_o^2 - k_x^2\right)^{1/2}} \tag{4.41}$$

which tends to infinity as k_x approaches k_o, so that some aliasing will occur. In practice k_s is chosen a few times greater than (k(z+h)) max.

Another problem arises due to the denominator in Eq (4.3) which goes to zero when $k_x = \pm k_o$. This integral can be interpreted as Cauchy principal values [Candel and Crance (1981)] and k_o should divide a sampling interval in equal halves such that

$$k_0 = (J + 1/2)\,\Delta k_x \tag{4.42}$$

where J is an integer less than N/4. The spatial window of the transformed result will be

$$L = N\Delta\ \lambda = (J + 1/2)\,\lambda_0\,. \tag{4.43}$$

In the following, N is chosen to be 2048 and J is 200, therefore $\Delta\lambda/\lambda \sim 10$ so that spatial wavenumbers up to 5 k_0 will not be aliased.

4.3 Comparison of Two Approaches

In this section, the results from the mixed approach are compared with the FFT results in both the upper and lower halfspace.

4.3.1. Upper Halfspace

The comparison explicitly stated for the upper halfspace is

$$\mathcal{F}^{-1}\left\{\left(1+\overline{\Re}\right)\frac{e^{-i\alpha(z+h)}}{i\alpha}\right\}\Delta k_x \Rightarrow -i\pi\left(1+\overline{\Re}(\theta_0)\right)H_0^{(2)}\left(k_0 s\right) + \sum_{j=1}^{3}\int_{-i\infty+k_j}^{k_j}\left(\overline{\Re}_{j-}-\overline{\Re}_{j+}\right)\frac{e^{-i\alpha(z+h)}}{i\alpha}e^{-ik_x x}dk_x + 2\pi\sum \mathrm{res}\left\{\frac{\overline{\Re}}{\alpha}e^{-i\alpha(z+h)}e^{-ik_x x}\right\} \tag{4.44}$$

where $\mathcal{F}^{-1}$ indicates inverse Fourier Transform, Δk_x is the sampling interval in the FFT, and the index "j" on the head wave summation (second term) refers to the three wave types: Type I, Type II, and shear wave. The plane wave reflection coefficient also has the subscript "j" in this term to indicate that along the path of integration (i.e. the branch cut)

the vertical wave number associated with each wave type is real, and is positive on the left side of the cut and negative on the right side. The terms on the RHS of Eq (4.43) represent, in order, the geometrical ray path contribution, the contributions from the three head waves and the contributions from surface wave(s). The quantity $(1 + \Re)$ was chosen for comparisons because it is functionally less complicated than $\Re$ and was consequently more stable in the FFT calculations.

Figure 4.8 shows the comparison at 100 Hz between the "exact" (numerical integration) solution, the FFT result, and geometrical ray path for source and receiver height of 50 meters (about 3 wavelengths) above a silty-clay poro-viscoelastic halfspace. For this geometry and sediment type the contribution of surface and head waves are negligible. In addition, the first order geometrical ray approximation quite adequately predicts the field. For Figures 4.8 - 4.11, the horizontal distance is expressed in wavelengths in the water.

Figure 4.9 shows a comparison at 100 Hz of the FFT, the geometrical ray path, and the "exact" solution for a source and receiver heights of 20 meters (about 1 wavelength) above a poro-viscoelastic sand interface. For this geometry and sediment type the contribution of surface and head waves are negligible. The geometrical ray approximation is adequate out to about 10 wavelengths. At this range the angle of incidence approaches the critical angle and the assumption that $\Re(\theta)$ is slowly varying breaks down.

Figure 4.10 shows a comparison at 10 Hz of the FFT, the surface wave, and the two head waves for a source and receiver on the boundary of a poro-viscoelastic sand halfspace. For this geometry the contribution of $(1+\Re)$ in the geometrical ray theory limit is zero. The difference between the "exact" result and the summation of surface and head waves is due to the fact that the condition of a slowly varying $\Re(\theta)$ is violated at all ranges since the geometrical angle of incidence is 90 degrees. At 90 degrees the function $\Re(\theta)$ is even more rapidly changing than at the critical angle. Thus, many terms in the expansion of $\Re(\theta)$ are required.

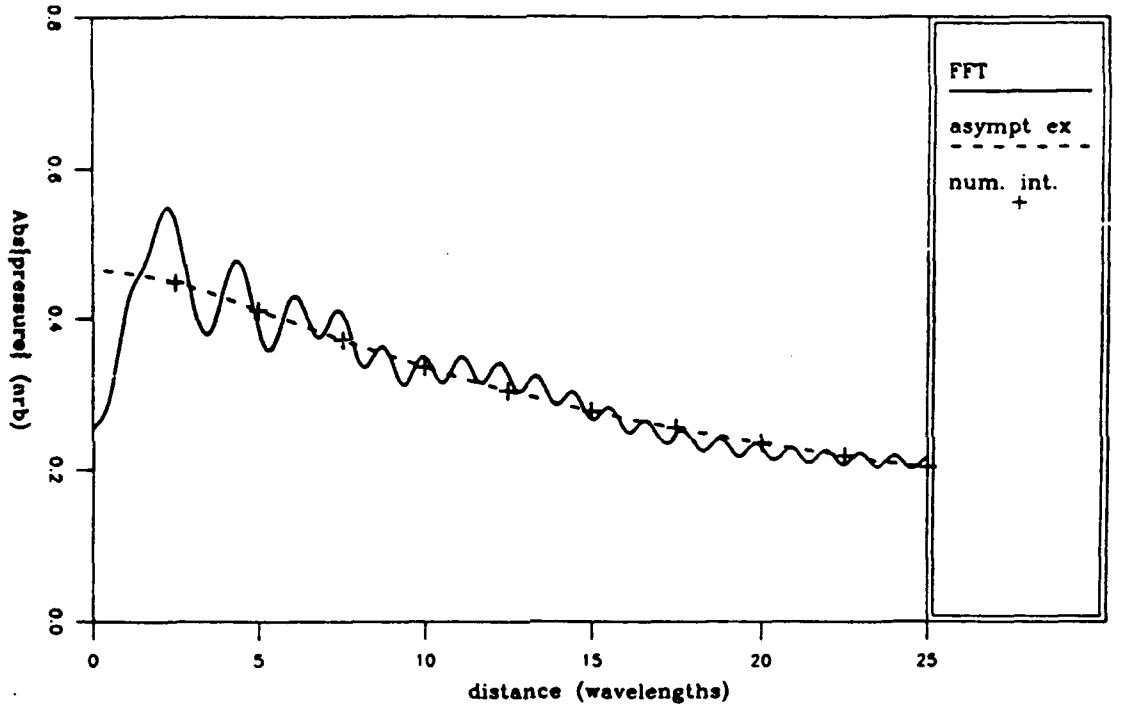

Figure 4.8 - Reflected plus image source field at 100 Hz calculated by FFT, numerical integration, and asymptotic expansion. The source and receiver are 50 m above a poro-viscoelastic silty clay halfspace.

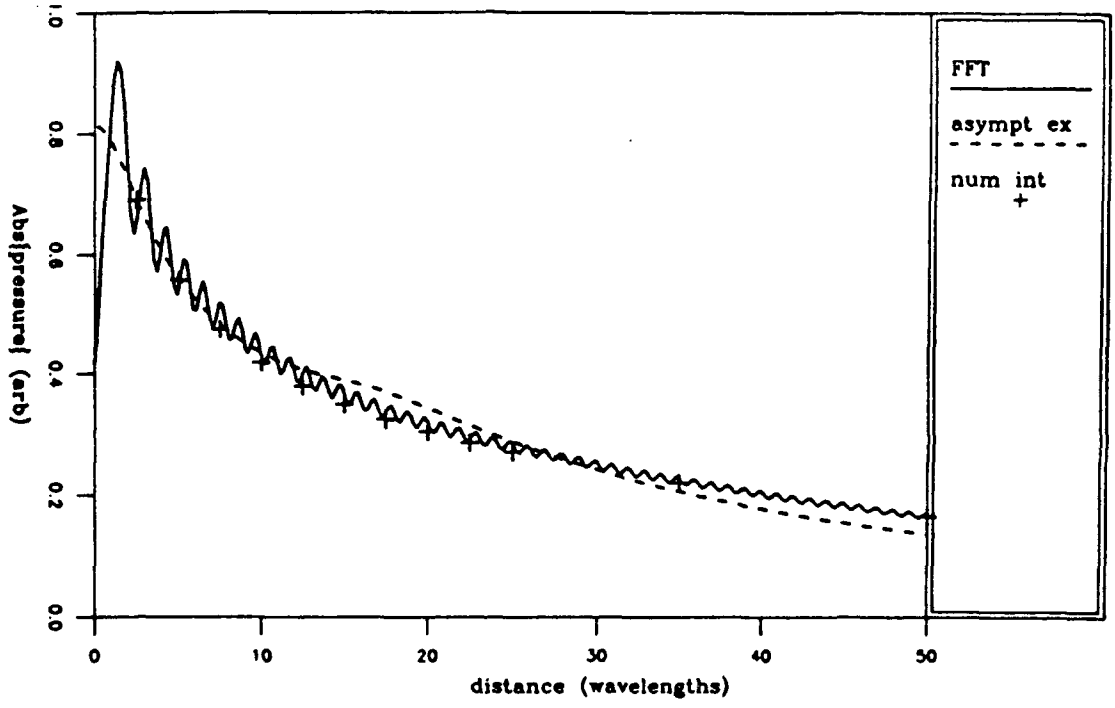

Figure 4.9 - Reflected plus image source field at 100 Hz calculated by FFT, numerical integration, and asymptotic expansion. The source and receiver are 20 m above a poro-viscoelastic sand halfspace.

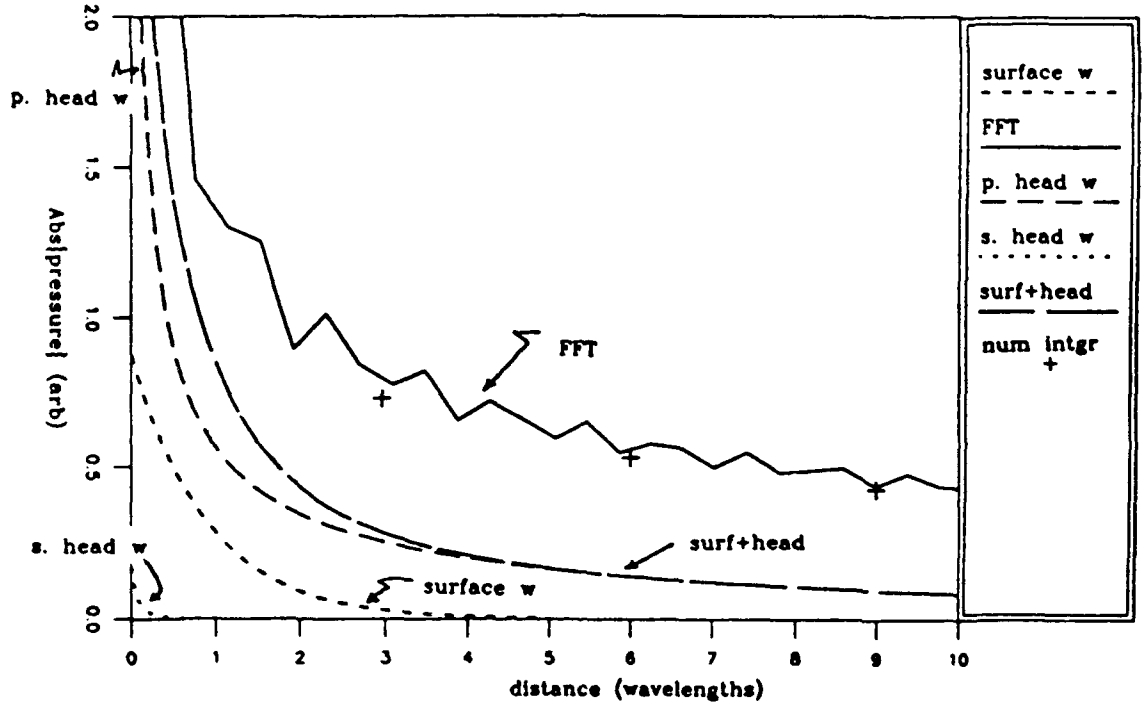

Figure 4.10 - Reflected plus image source field at 10 Hz calculated by FFT and numerical integration. The source and receiver are on the boundary of a poro-viscoelastic sand halfspace.

4.3.2 Lower Halfspace

Figure 4.11 shows a comparison at 100 Hz of the FFT, the geometrical ray path, and the "exact" solution. Here the source and receiver are 20 m (about 1 wavelength) above and below a poro-viscoelastic sand interface, respectively. For this geometry and sediment type the contribution of surface and head waves are negligible. In addition, the geometrical ray approximation quite adequately predicts the field.

Predictions for the transmitted field were also made on the boundary for the sand case as a test to make sure that the boundary conditions were met numerically. The pressure field predictions for the transmitted field were in fact virtually identical with the sum of the incident and reflected field results on the interface.

4.4 Summary and Conclusions

In this chapter, the integral expressions for the field from a line source above a poro-viscoelastic halfspace were evaluated: by a decomposition of the field into various wave types (the "mixed" approach), and by FFT. The mixed approach results were compared with the exact solution and the FFT results in order to determine which wave types were contributing to the field for several examples. These results could have been compared with commensurate quantities using the single phase models, however, the differences would be entirely due to differences in the plane wave reflection and transmission coefficients. The poro-viscoelastic and single-phase models of plane wave coefficients were previously (in Chapter 3) compared in detail.

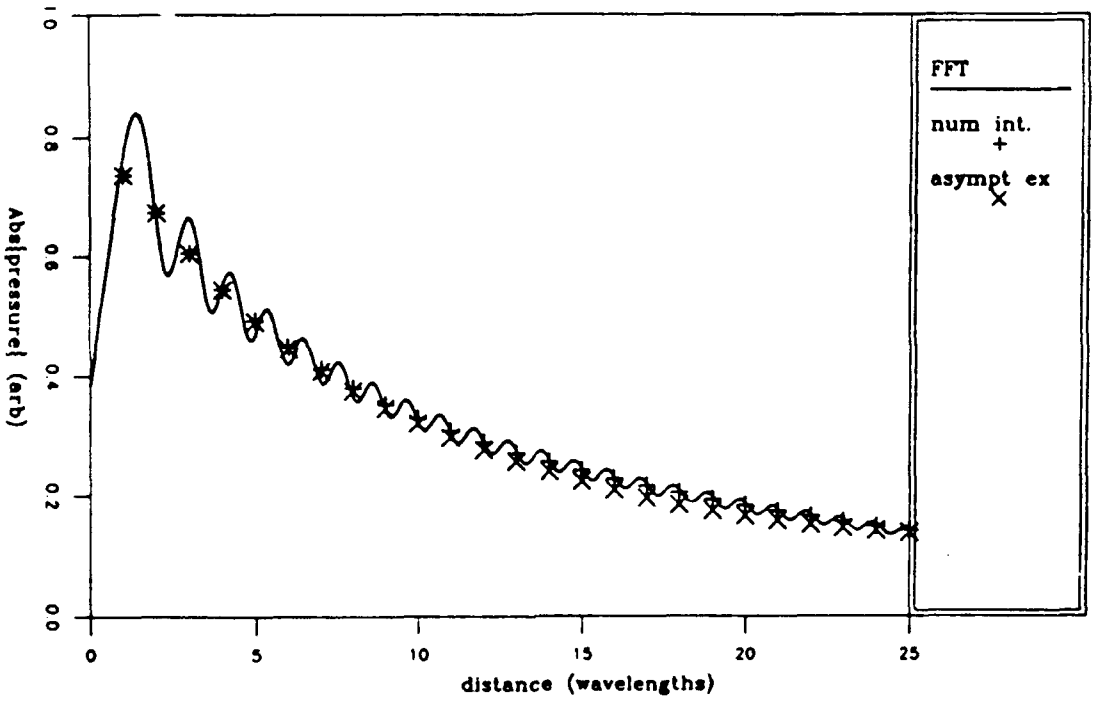

Figure 4.11 - Transmitted field at 100 Hz calculated by FFT, numerical integration, and asymptotic expansion. The source and receiver are respectively 20 m above and below a poro-viscoelastic sand halfspace.

Chapter 5

COMPARISONS WITH EXPERIMENTAL DATA

Recent experiments [Chotiros (1989), Satkowiak (1988), and Muir et al. (1979)] of acoustic interaction with the seafloor have indicated anomalous behavior of high-frequency transmission through the water-sediment interface when the surficial sediments are granular (sands). The unexplained results include anomalously high transmission near the critical angle, anomalously low phase speeds in the sediment (~1000 m/s), and angles of refraction in the sediment that appear not to obey Snell's law. The anomalies are defined as lack of agreement with classical, single-phase models of transmission at the interface between two semi-infinite halfspaces. By contrast, the experiments indicated good agreement with classical single-phase models when the sediment is clay-like.

One of the anomalous experimental data sets will be compared against the predictions for transmission through a poro-viscoelastic interface to determine whether whether the Type II wave plays a significant role in the transmission process and is the cause of the anomalies. The acoustic data set reported by Chotiros (1989) was chosen for analysis in this chapter because the accompanying, comprehensive sediment geophysical and geoacoustic measurements were more complete than for any of the other data sets.

A brief description of the experiment [Chotiros (1989)] follows. A three-dimensional array of 12 hydrophones was buried to record various aspects of a transmitted pulse. The hydrophones were arranged in two orthogonal vertical planes on two sides of a cube approximately 40 centimeters in length. The shallowest probe was set at 5 cm below the water-sediment interface at the intersection of the two planes. The source was mounted near the top of a tower (4.5 meters above the seafloor) that could be moved along the seafloor by divers to vary the angle of incidence of the impinging sound field from normal incidence to a nominal grazing angle of 22 degrees (see Figure 5.1). The frequencies used in the experiment were 5, 8, 15, 20, 30, 60, and 80 kHz and the associated beamwidths (at

the 3 dB down points) varied from 45 degrees vertical and 30 degrees horizontal at the lowest frequency to 3 degrees vertical and horizontal at the highest frequency. The raw acoustic data were processed for signal energy densities and relative arrival times using a cross-correlation technique and a homomorphic deconvolution method; plane wave front direction and group velocity using a least squares approach; and the transmitted sound pressure level (SPL) which required essentially no signal processing. The generated signals included various pulse shapes and lengths, however, for the data of interest to this chapter, no dependence on pulse shape or length was found. An extensive set of geoacoustic measurements were made at the experimental site (the particulars of the geoacoustic data are discussed in detail in the following section, section 5.1) and the buried hydrophone array data were compared with the SAFARI [Schmidt et al. (1985)] model using the measured sediment geoacoustic properties as inputs.

The receivers buried in the sediment were hydrophones and as such measured the transmitted pressure field. It will be assumed that the receiver was measuring the pressure field in the interstitial pore fluid (although it is not clear that the fluctuations of the solid sediment frame against the hydrophone diaphragm did not also contribute to the measured signal). The theoretical transmitted pressure field in the pore fluid was derived in Chapter IV and is given by Eq (4.20). The differences between the formulation in this work (Eq (4.20)) and the experimental data just described include:

Theoretical Model	Experimental Data
Continuous Wave	Pulse
Line Source	Beamed source with beamwidth a function of frequency

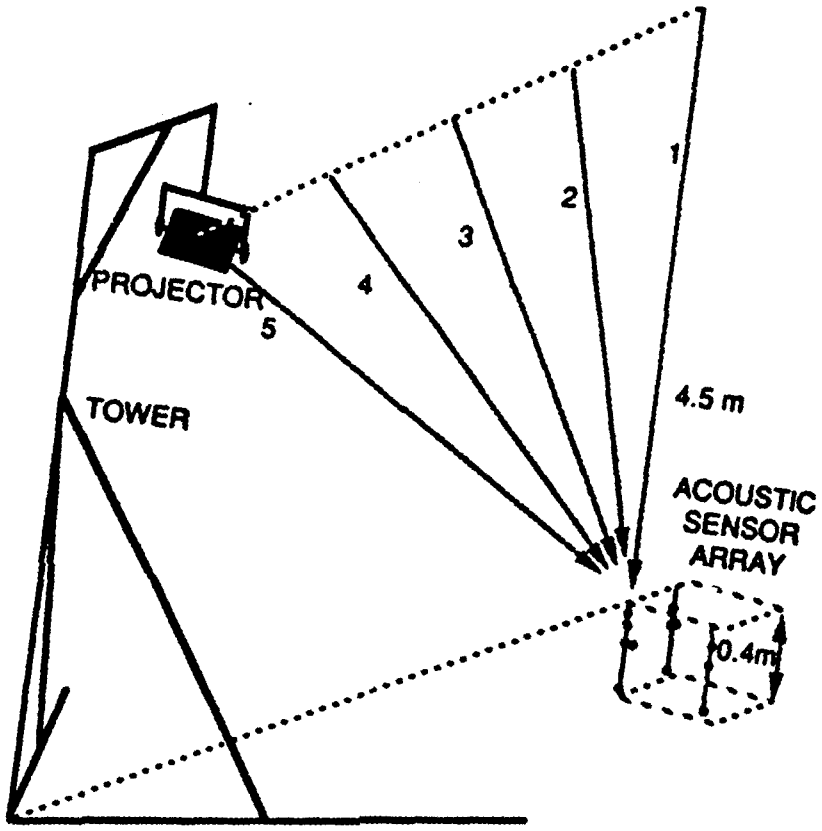

Figure 5.1 Layout of the experiment (Chotiros (1989))

Although Eq (4.20) could be modified to take into account the effects of a finite pulse and the aperture, the processing involved to make predictions directly comparable to the experimental data seemed fraught with difficulties, the resolution of which seemed beyond the scope of this work. Thus, the predictions of Eq (4.20) will be used to examine trends in the experimental data with the goal of determining how the two-phase nature of a granular sediment can influence transmissivity. The experimentally measured sound pressure level (SPL) will be focused on since this was a direct measurement. The other quantities (wave velocity, transmission coefficient, refraction angle, and absorption) were derived quantities (from several least-squares and deconvolution techniques) and not truly comparable to simple notions of these quantities because of the interference of the evanescent field. Comparison of these derived quantities with the theory herein would require using the ARL-UT processing programs on synthetically generated array data. This was not done.

The approach taken here in the data comparisons is to first derive the thirteen Biot geophysical parameters for the sediment at the experimental site. Some of the parameters were measured directly, some of the parameters can be obtained by empirical or semi-empirical methods, and the remaining parameters can be fitted using the measured acoustic data (compressional wave speed and attenuation) as guides. Biot theory is then used to calculate wave speeds and attenuation as a function of frequency over the band of interest (the experimental data were obtained at frequencies of 5 kHz - 80 kHz). These results will be compared with the geoacoustic model that was developed based on the core data and measurements of compressional and shear wave velocity and compressional wave attenuation across several cores. Finally, the anomalous transmitted SPL data near the critical angle will be examined.

5.1 The Sediment Model

In this section the 13 Biot input parameters are obtained for the sandy sediment at the experimental site.

The sediment geoacoustic properties that were measured included the compressional wave velocity and attenuation at 400 kHz and 120 kHz, and shear wave velocity at around 1 kHz. The measured sediment geophysical properties included porosity, permeability, and grain density (K. Briggs, personal communication). The grain bulk modulus was taken from the handbook value for quartz [Clark (1966)]. The properties of the interstitial pore fluid were determined by empirical equations based on the temperature and salinity at the laboratory conditions. The frame shear modulus was determined from the product of the square of the shear velocity and the density which is nearly an exact relation since the viscosity of seawater is small (see Eq(2.52)). These properties (porosity, permeability, grain and fluid properties, and shear modulus) are the most important parameters in the Biot theory for the prediction of wave speeds and attenuations; the remaining parameters were varied within reasonable bounds in an attempt to match the average measured wave compressional velocity. The variability in predicted compressional velocity with variability in these parameters was quite small, with predictions varying roughly 1825-1850 m/s at 400 kHz, confirming that the unknown parameters in this case are less significant than the parameters that were measured. However, no combination of the remaining parameters would produce predictions as low as the stated 1743 m/s (see Table 5.1). Thus, the remaining parameters were set to values that seemed most appropriate. The frame bulk modulus was obtained by the assumption of a frame Poisson's ratio of .2 [Hunter (1961)]. The pore size parameter was obtained by the relation [Hovem et al. (1981)]:

$$a = 2\,(5\,\chi/\beta)^{1/2} \quad . \tag{5.1}$$

The logarithmic decrements for both the frame shear and bulk moduli were chosen to be .05 which is roughly in the middle of the range suggested by Stoll (1980). Finally, the structure factor was chosen to be 1.25 based on Stoll (1974). The input parameters for Biot theory are given in Table 5.2 and the predicted velocities and attenuations are shown (along with the measured data) in Figures 5.2-5.7. The predicted Type I wave velocity is somewhat higher than that measured, the predicted Type I attenuation is substantially lower than that measured, and the predicted shear velocity is the mean of the measured data since the frame shear modulus was chosen from the mean of the shear velocity data.

It is believed that some, if not all, of the noted differences between Biot theory and the measured data are attributable to scattering in the core measurements. Theoretical and experimental evidence [Plona and Winkler (1985)] of multiple scattering in such media indicates that compressional velocity decreases monotonically with increasing scatter, and that attenuation increases with increasing scatter. A closer look at the measured geoacoustic properties, in fact, indicated that both of these trends exist in the data. As evidence of scattering in the measurements, consider Figure 5.8 which shows measured compressional velocity at 120 kHz and 400 kHz, and mean grain size as a function of depth in the core at the measurement site. First, in examining just the frequency dependence of the two velocity measurements, the negative velocity dispersion is clearly evident; that is, the 400 kHz velocity measurement is consistently lower than the 120 kHz data. Second, scattering is evident from the middle of the core. Between 20 and 40 cm there was a layer of shell hash which is evidenced by the increase in mean grain size. Note that the measured velocity at 400 kHz decreases sharply with increase in grain size.[3] For granular sediments, however, compressional velocity is theoretically (and empirically)

[3] Mean grain size can not be considered to be perfectly correlated with scattering since the scatter may be caused by a relatively small number of large grains that may not be well indicated in a mean grain size average.

Table 5.1 ARL-UT geoacoustic model

Property	Units	Value
Fluid density	g/cm^3	1.02
Fluid speed	m/s	1536
Sediment density	g/cm^3	2.06
Sediment compressional speed	m/s	1743
Sediment compressional attenuation	dB/m/kHz	0.5
Sediment shear speed	m/s	100
Sediment shear attenuation	dB/m/kHz	13.2

Table 5.2 Geophysical inputs to Biot theory

Property	Units	Value
Fluid density, (ρ_o)	g/cm^3	1.024
Fluid bulk modulus, (K_f)	$dyne/cm^2$	$2.396\ 10^{10}$
Fluid viscosity, (η)	poise	.0101
Grain density, (ρ_s)	g/cm^3	2.66
Grain bulk modulus, (K_s)	$dyne/cm^2$	$3.6\ 10^{11}$
Porosity, (β)		.3673
Permeability, (κ)	cm^2	$3.3\ 10^{-7}$
Structure factor, (c)		1.25
Pore size, (a)	cm	$4.2\ 10^{-3}$
Frame bulk modulus, (K_m)	$dyne/cm^2$	$2.27\ 10^8 + i\ 3.6\ 10^6$
Frame shear bulk modulus (μ)	$dyne/cm^2$	$1.7\ 10^8 + i\ 2.7\ 10^6$

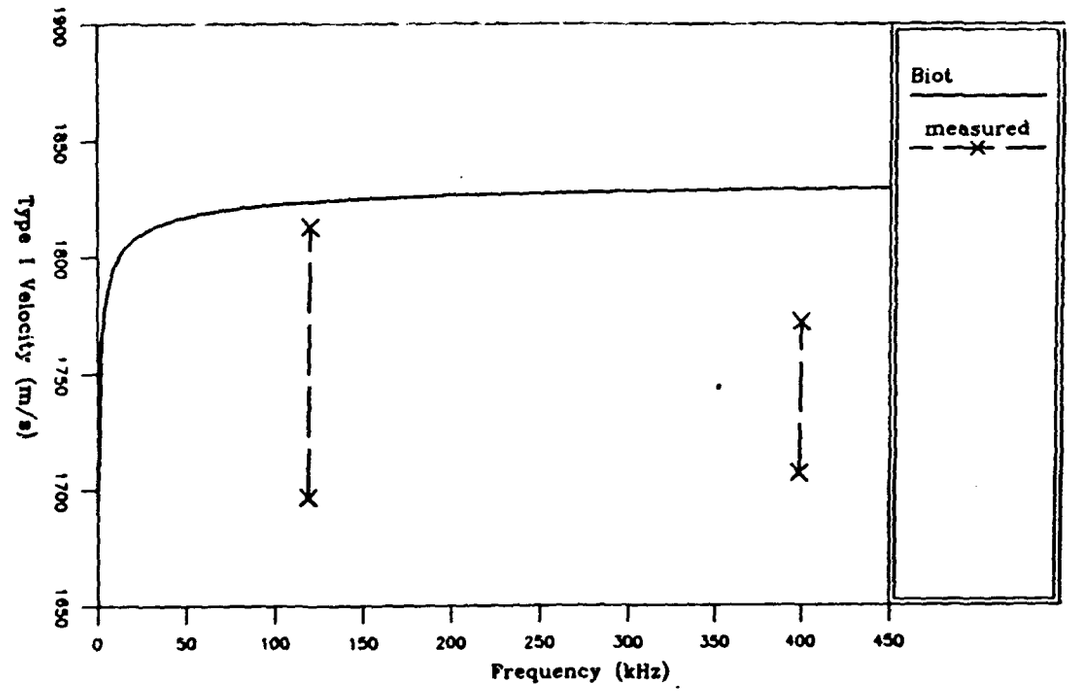

Figure 5.2 Type I Wave Velocity Predicted by Biot Theory from Table 5.2

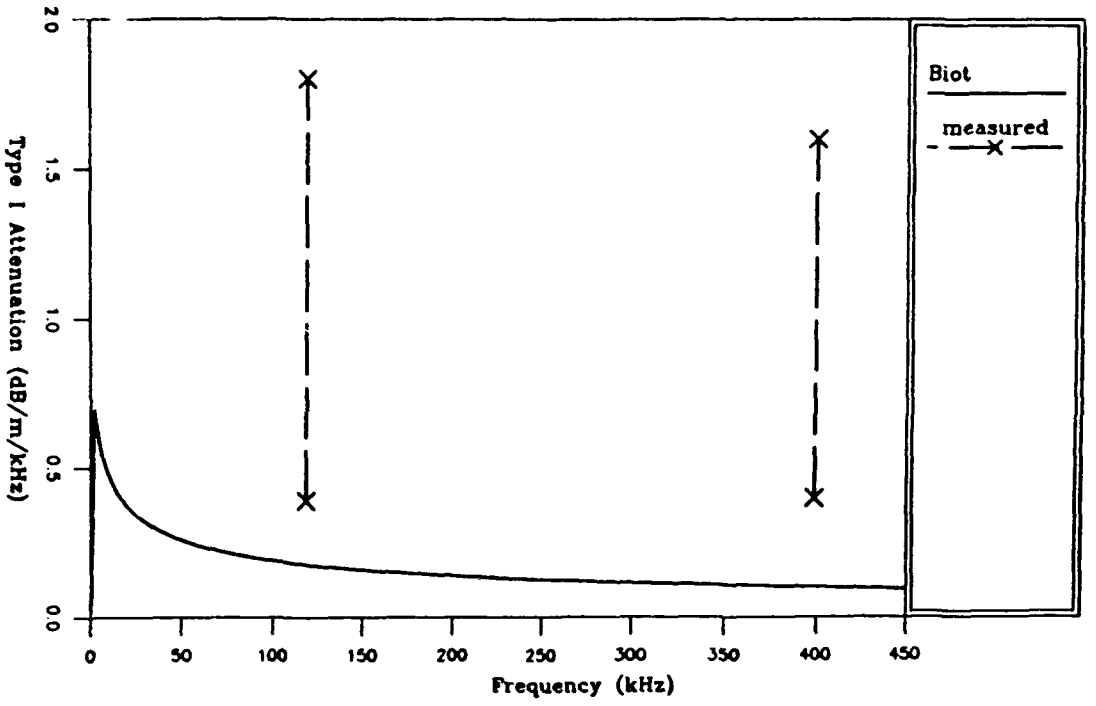

Figure 5.3 Type I Wave Attenuation Predicted by Biot Theory from Table 5.2

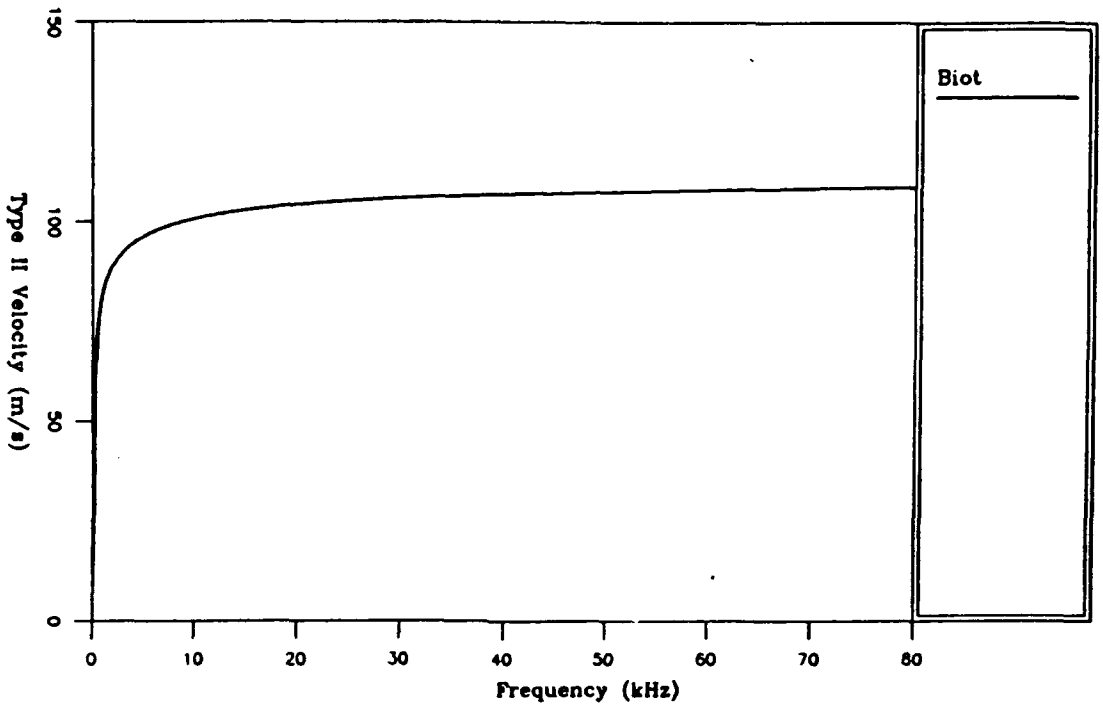

Figure 5.4 Type II Wave Velocity Predicted by Biot Theory from Table 5.2

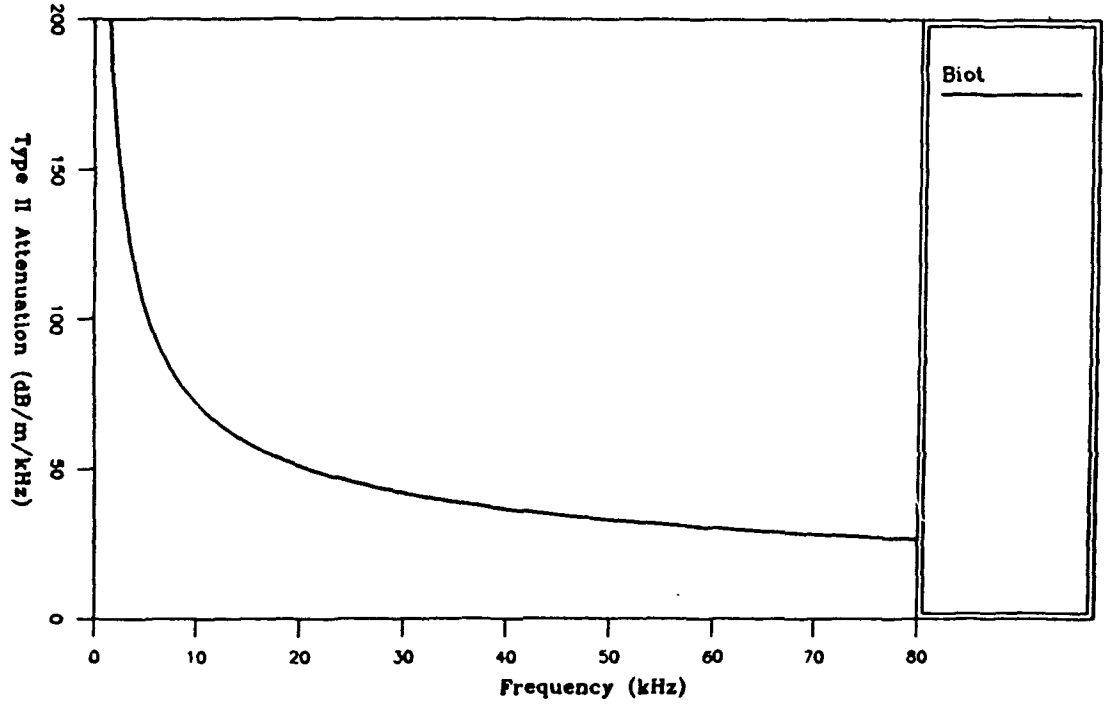

Figure 5.5 Type II Wave Attenuation Predicted by Biot Theory from Table 5.2

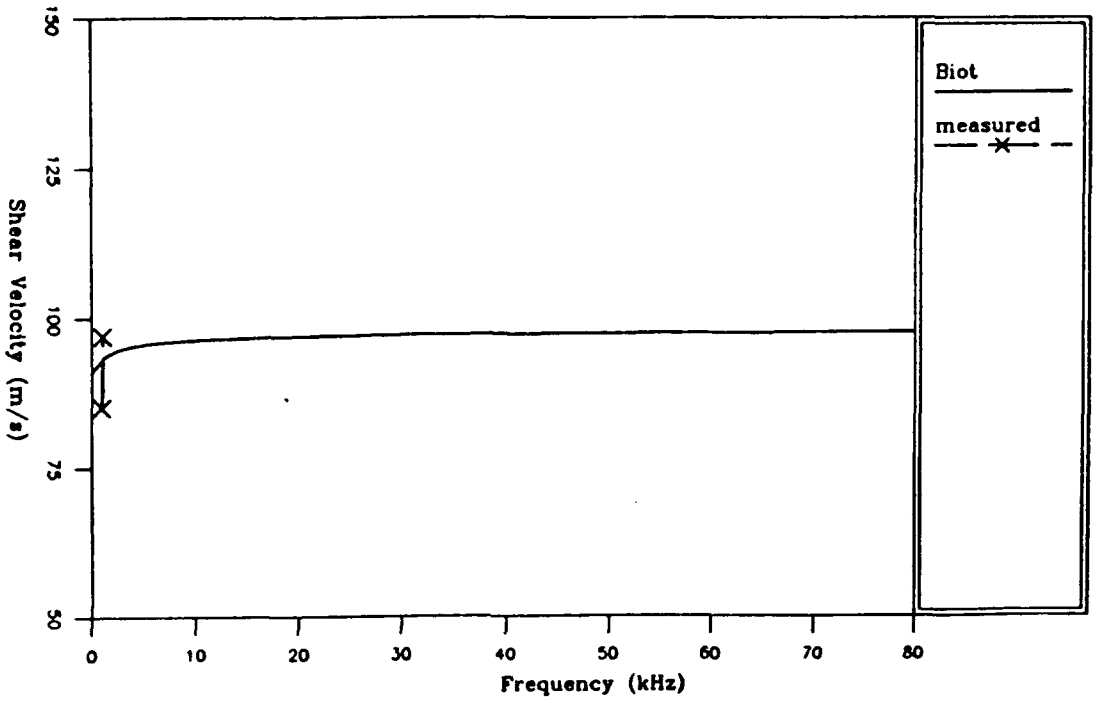

Figure 5.6 Shear Wave Velocity Predicted by Biot Theory from Table 5.2

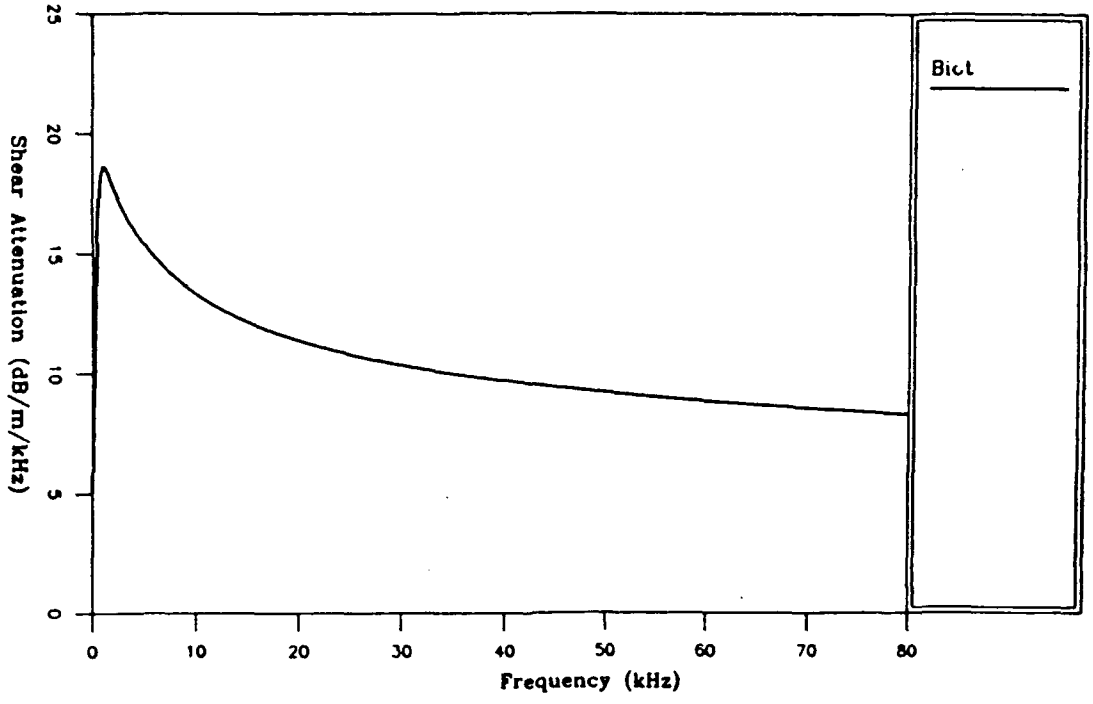

Figure 5.7 Shear Wave Attenuation Predicted by Biot Theory from Table 5.2

directly proportional to grain size. This negative velocity dispersion in the data strongly suggests scattering. Based on the data in Figure 5.8, it is clear that the average value of compressional wave velocity of 1743 m/s in the ARL-UT model (Table 5.1) was contaminated by scatter. Furthermore, it is postulated that since shell fragments were noted throughout the sediment column, all the velocities in Figure 5.7 are contaminated by scatter and the true velocity is somewhat higher, perhaps close to that predicted by Biot theory.

In Figure 5.9 the attenuation (in dB/m/kHz) is plotted against depth in the core along with the mean grain size. Consider first just the frequency dependence of the attenuation. The consistent increase in attenuation with frequency is again strongly indicative that the core measurements are contaminated by scatter (at least at 400 kHz). It is not clear without a lower frequency measurement whether the 120 kHz data is contaminated. Second, the large (and unrealistic) measured attenuations toward the middle of the core are almost certainly highly contaminated by scattering losses.

At this site, group velocities in the granular sediments were measured at about 1100 m/s. It was suggested by Chotiros (1989) that this may be a propagatory wave type not predicted by classical theory. The Biot theory in fact does predict another wave type (in addition to the classical compressional and shear velocity) that is a compressional wave and does travel at lower speeds than the classical compressional wave speed (at least in fluid-saturated marine sediments). It was of interest therefore to calculate its velocity to examine the possibility of whether or not the measured wave might be the Type II Biot wave. At 80 kHz the velocity of the Type II was predicted to be roughly 100 m/s and no reasonable combination of geophysical parameters could force predicted velocity as high as that observed.

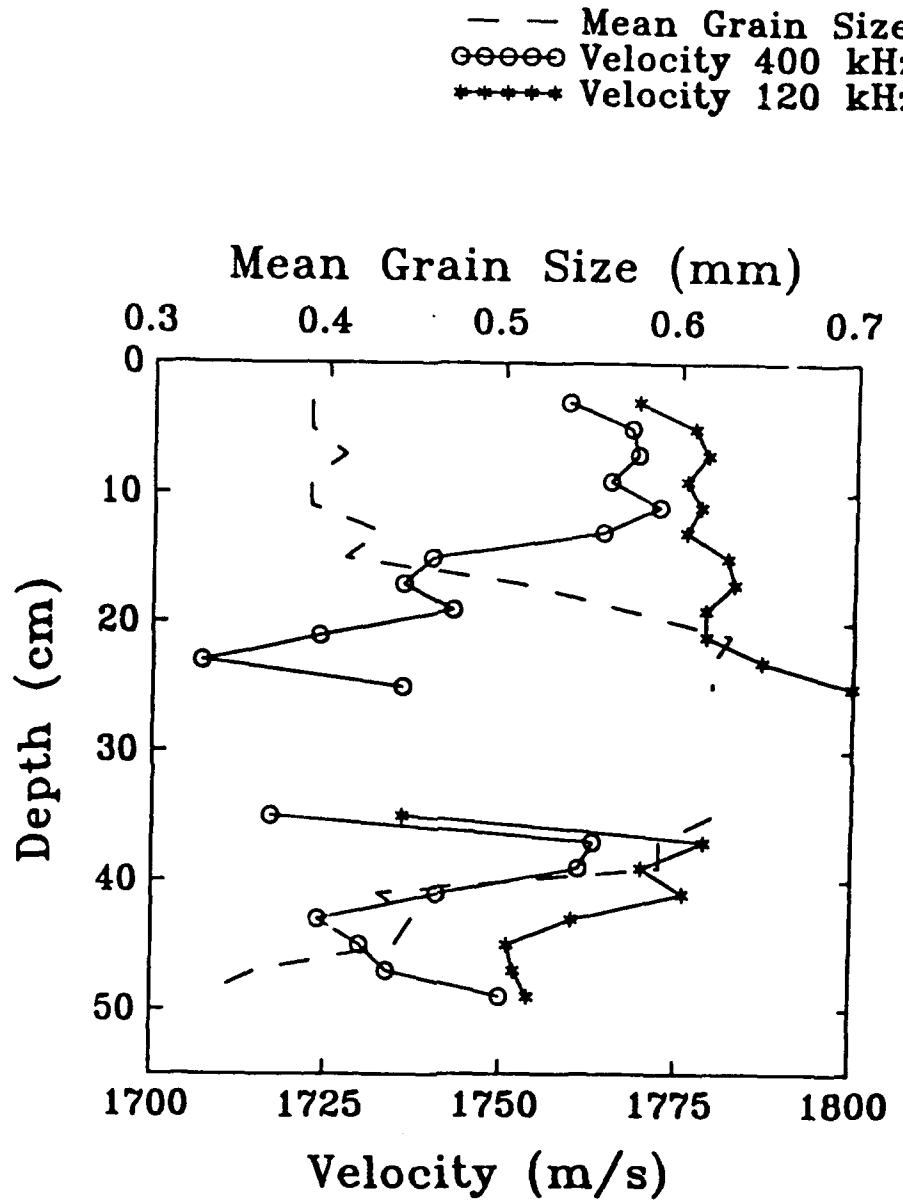

Figure 5.8 Measured velocity at 120 kHz and 400 kHz from core data taken at the buried array site with mean grain size

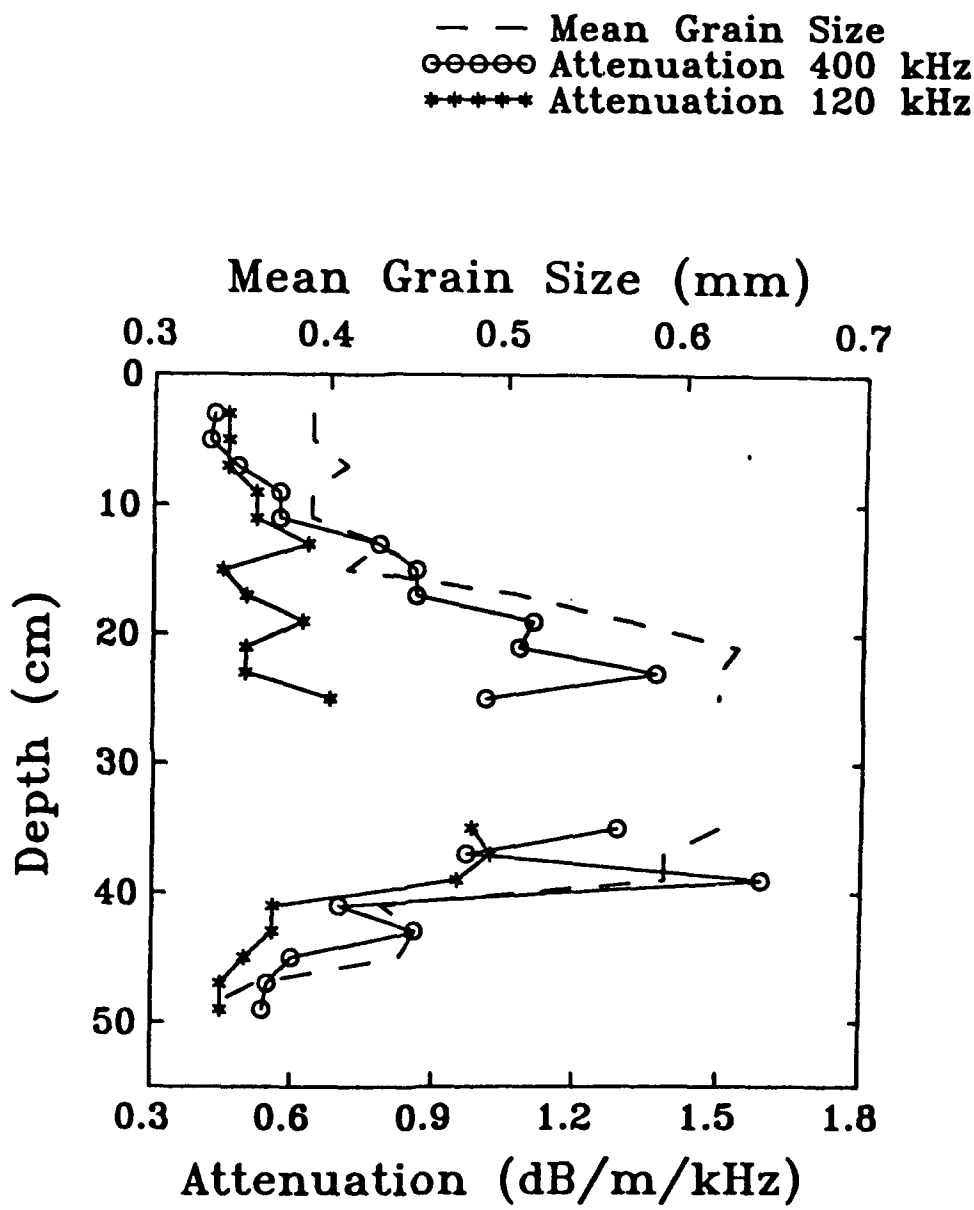

Figure 5.9 Measured attenuation at 120 kHz and 400 kHz from core data taken at the buried array site with mean grain size

5.2 Sound Pressure Level Comparisons

The experimental transmitted sound pressure levels (SPL) were compared [Chotiros(1989)] against a full wave model (SAFARI) that considers the sediment to be a solid. The geoacoustic inputs to the model were developed from the core data and are given in Table 5.1. The difference between the measured acoustic transmissivity and the SAFARI model predictions are plotted as excess SPL in Figure 5.10 for two tower positions (TP): TP 3 (corresponding roughly to a 39 degree grazing angle) and TP 5 (corresponding roughly to a 22 degree grazing angle). Positive differences in Figure 5.10 indicate that the model predictions are too low. Note that at TP 3, where the grazing angle is far from critical, the model predictions are in reasonable agreement with the data except at the highest frequency. At TP 5, however, the measured transmissivity is much greater than that predicted over most of the band. The standard deviations are over all the hydrophones in the array.

It is the purpose of this section to determine whether the Biot theory could provide a better explanation of the observed transmissivity. The approach taken was to difference the results of Eq(4.20) using the geoacoustic model predicted by Biot theory from Table 5.2 (this result represents the Biot theory prediction) with the results of the first term of Eq(4.20) using the ARL-UT geoacoustic model (Table 5.1) to calculate the moduli, the wavenumbers and the transmission coefficient (which represents the full-wave solution where the sediment is considered as a solid). The resulting excess SPL then can be compared with Figure 5.10.

In the results that follow, the properties of the water are chosen to be representative of *in situ* conditions (density= 1.02 g/cm^3 and bulk modulus= 2.4065 10^{10} dyne/cm^2). These are appropriate for comparisons with the acoustic data; they differ somewhat from the fluid properties at the laboratory conditions in Table 5.2, and are consistent with the fluid properties in the ARL-UT geoacoustic model (Table 5.1).

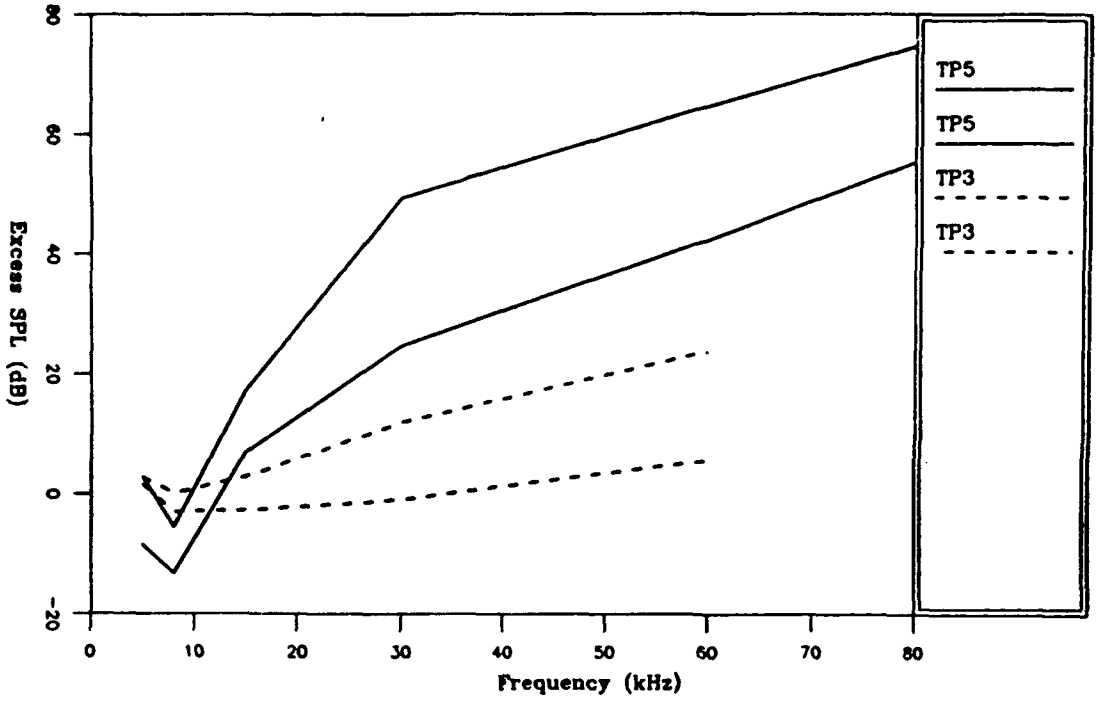

Figure 5.10 Measured minus predicted acoustic pressure levels in the sediment: mean values +- one standard deviation at tower positions 3 and 5 for all the hydrophones in the array

Comparisons were made between Eq (4.20) with the ARL-UT geoacoustic model and Eq (4.20) using Biot theory. For the comparisons, a receiver depth of .4 m was used. The ARL-UT model-to-Biot theory comparison results are shown in Figure 5.11 which compare favorably with the ARL-UT model-to-data comparison in Figure 5.10. The excess SPL in Figure 5.11 can be ascribed to one or a combination of the following effects on transmission to a buried receiver:

excitation of Type II waves,
surface wave contributions,
head wave contributions,
transmission across the water-sediment interface, or
attenuation along the path in the sediment.

In order to isolate which effect(s) caused the differences observed in Figure 5.10, each contribution was examined separately. The second term of Eq(4.20) was calculated to determine the contribution of Type II waves to buried receiver and was found to be negligible at all frequencies at both tower positions. Next, the surface and head wave contributions were calculated from Eq(4.37 and 4.34-4.36) respectively; the pressure field from these contributions was likewise negligible.

The plane wave transmission coefficient was calculated for Biot theory and the ARL-UT model. The magnitude of the plane wave transmission coefficients are shown in Figure 5.12 where at a given angle the Biot model predicts a somewhat lower transmissivity due to conversion of energy to the Type II wave. The conversion is stronger (hence lower transmissivity) with increasing frequency. Comparing the transmissivity between the Biot and the ARL-UT model it is clear that the differences in transmissivity between the two models accounts for only a few dB at all frequencies and at both sites. Thus, the transmission differences between the Biot and ARL-UT model are not enough to account for the excess SPL.

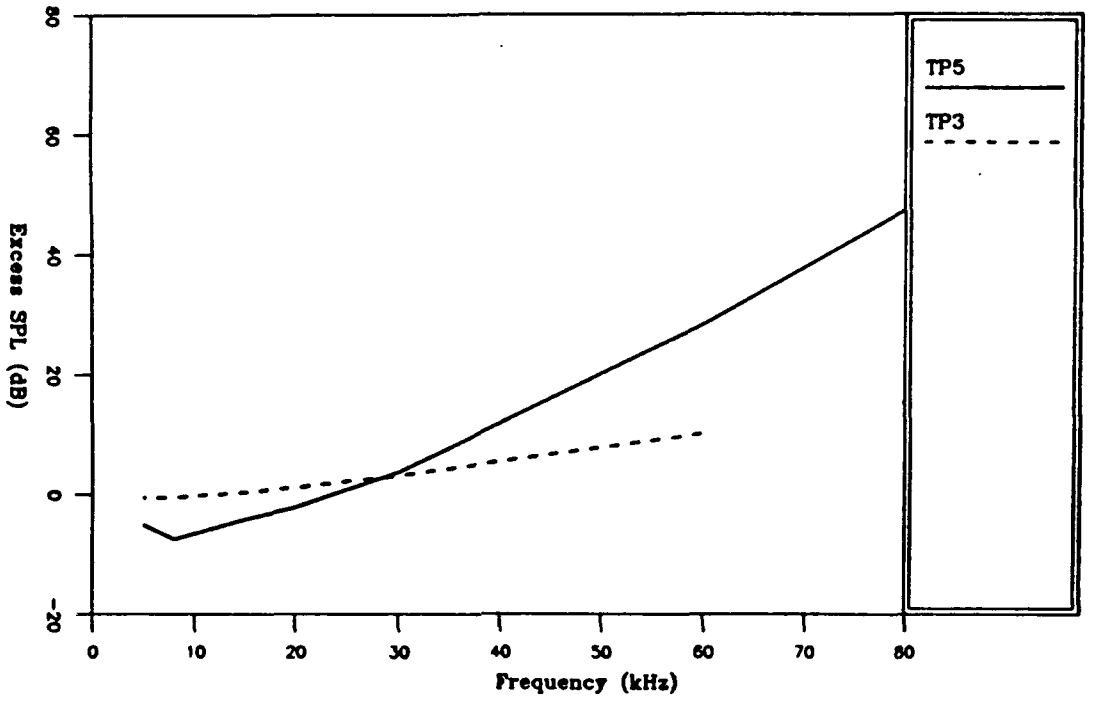

Figure 5.11 Biot Theory minus the ARL-UT geoacoustic model predictions of acoustic pressure levels in the sediment for a single hydrophone located near the bottom of the buried array (40 cm)

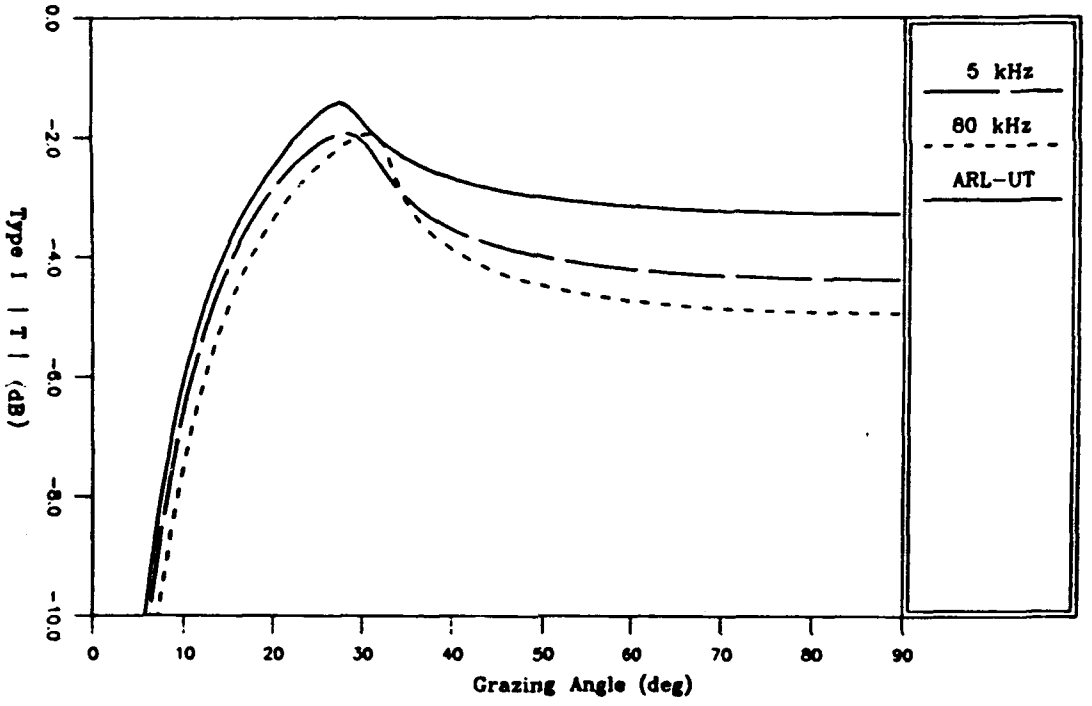

Figure 5.12 Plane wave transmission coefficient predicted by Biot theory and the ARL-UT geoacoustic model

The final possibility for the excess SPL in Figure 5.11 is differences in the product of sediment path length[4] and attenuation. Indeed, the non-linear attenuation predicted by Biot theory is quite different from the ARL-UT model (see Figure 5.13). At TP 3 the path lengths in the sediment are short and the effect of the attenuation is fairly small. Note, though, that the effect of attenuation increases with increasing frequency (since attenuation, in dB/m, increases with increasing frequency). At TP 5, the path length in the sediment is longer and the effect of the different attenuations is more pronounced (50 dB excess SPL at 80 kHz). At low frequencies, the excess SPL in Figure 5.11 shows a minimum at 8 kHz similar to that in the excess data SPL (Figure 5.10). The cause of the minimum in Figure 5.11 is the crossing of the Biot non-linear attenuation with the linear attenuation of the ARL-UT model between 8 kHz and 15 kHz as shown in Figure 5.13. That is, at 5 kHz and 8 kHz, the Biot attenuation is greater than the ARL-UT attenuation such that the slope of the SPL excess is negative; at 15 kHz and above the Biot attenuation is less than the ARL-UT model so that the slope of the SPL excess becomes positive.

5.3 Summary and Conclusions

Data were examined that exhibited anomalously high transmitted SPL (with respect to the single-phase model, SAFARI) in order to determine whether the anomalies were due to the Type II wave. Calculations indicated that the Type II contributions were negligible and were not the cause of the anomalies. This conclusion rests heavily on the constructed geophysical inputs to Biot theory for the sediment in question (Table 5.2) and the small (~ 100 m/s) Type II wave velocity predicted therefrom. The conclusion is robust, though, in that many of the geophysical inputs were measured and that varying the geophysical inputs

[4] The effects due to differences in the sediment path lengths predicted by Biot theory and the ARL-UT model are small compared with the effects of intrinsic attenuation.

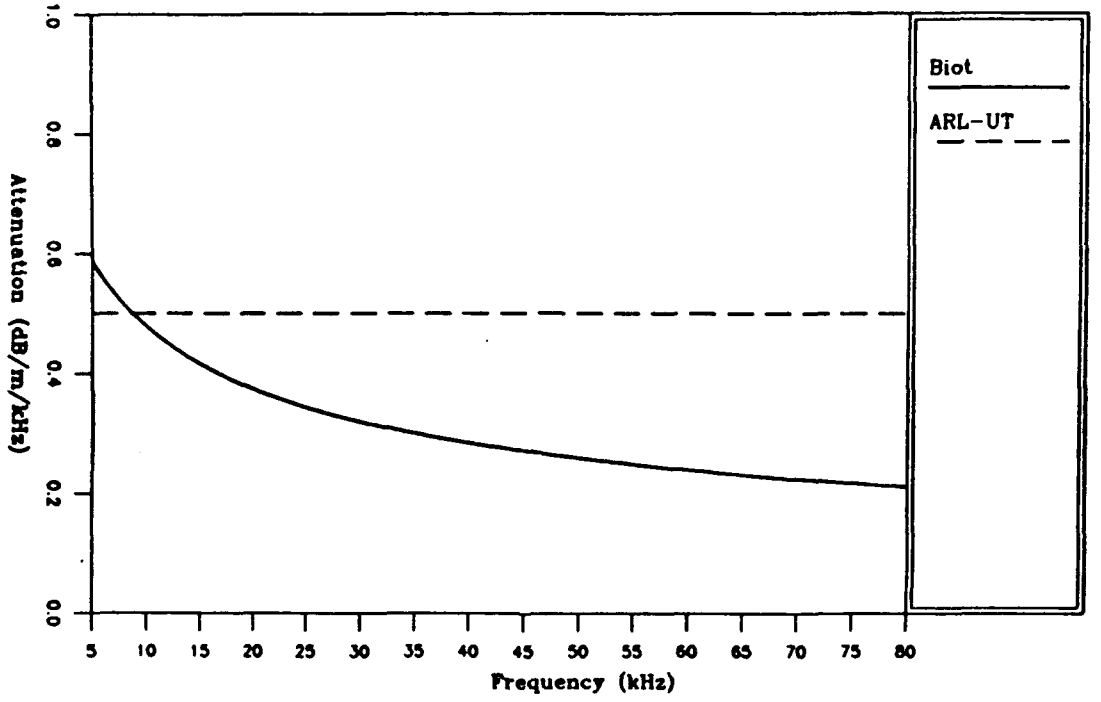

Figure 5.13 Comparison of attenuation per kHz

(within physically plausible limits) does not make the Type II wave contributions non-negligible.[5]

Much of the anomalous behavior appeared to be simply the result of an incorrect compressional wave attenuation. The excess SPL at TP 3 appears to be entirely explainable in terms of the compressional wave attenuation (compare Figures 5.10 and 5.11). The excess SPL at TP 5 appears to be due to compressional wave attenuation at low (5 kHz and 8 kHz) and high (60 kHz and 80 kHz) frequencies. The two mid-frequencies (15 kHz and 30 kHz) at TP 5 are not well-explained by the present modeling but may be due to effects not accounted for in the modeling such as the presence of the shell layer (an impedance boundary) at 15 cm (see Figure 5.8). Suffice it to say, however, that the anomalies are not due to the Type II wave.

Thus, in large measure, the failure of SAFARI in predicting the observed levels lay not in the neglect of the Type II waves but simply in the incorrect geoacoustic model which was based on the apparently contaminated core data. The Biot theory provided the means to check the core data based upon the geophysical inputs that are, in general, more reliably measured.

[5] The one possible exception is if gases were present in the interstitial fluid. Even small amounts of gas are known to have significant effects on compressional wave velocity. If gas were present, the measured velocity of 1100 m/s may be velocity of the Type I wave, and the excess SPL in Figure 5.10 could be explained by simple path length considerations.

Chapter 6

SUMMARY AND CONCLUSIONS

The Biot theory of propagation in a porous medium provides a mathematical framework for studying acoustic interaction with the seafloor. The theory considers the two-phase porous nature of marine sediments in contrast to the classical models of wave propagation in the seafloor that consider marine sediments as an extended single-phase fluid or solid. A boundary value problem was set up and solved for a line source in a fluid medium above a poro-viscoelastic halfspace. Expressions for the reflected and transmitted field were given in integral form and asymptotic expansions in the high-frequency, far-field limit. A set of simultaneous equations was solved to give plane wave reflection and transmission (Type I , Type II and shear wave) coefficients. These equations also yielded the Scholte, pseudo-Scholte, and pseudo-Rayleigh wave phase velocities and attenuations.

The expressions obtained for the transmitted field in the pore fluid were compared with measured data from an array of hydrophones buried in sand and insonified at high frequency. This data set had shown much higher transmissivities near the critical angle than that predicted by a single-phase, solid model (SAFARI). The Biot theory was used both to develop a geoacoustic model (Type I, Type II, and shear wave velocities and attenuations, and density) and to model the acoustic transmissivity of the sand. The Biot theory showed qualitative agreement with the measured data. Surprisingly, this was not due to a poro-viscoelastic effect (i.e., contributions from the Type II wave) as speculated. In fact the contributions from both the Type II wave and the shear wave were negligible. The agreement was due simply to the realism of the geoacoustic model (in particular the Type I wave attenuation) at the experimental frequencies. The SAFARI results were based on measured core data believed to be contaminated by scatter.

The principal objective of this work was to understand how the porous nature of marine sediments influences reflection from and transmission through the seafloor. This

was accomplished by comparing plane wave coefficients between poro-viscoelastic (using Biot theory), viscoelastic, and fluid models of the sediment. The differences between the geoacoustic models from Biot theory and from the single phase models include: the frequency dependence of the phase velocities, and the existence of the compressional wave of the second kind. The effect of each difference on the plane wave coefficients is summarized in the following paragraphs.

The frequency dependence of the velocities and attenuations in Biot theory were sufficient to cause differences in the plane wave coefficients with respect to those predicted by the classical single phase models. For the sand case the critical frequency was low enough to be in the frequency range of interest. Therefore, the velocity and attenuation of each wave type (especially the Type I wave which is the most important wave influencing reflectivity for this sediment type) varied non-linearly over the band of interest leading to the frequency dependent plane wave coefficients. For the silty clay case, the critical frequency was high enough that the velocity of the Type I wave (the only wave participating strongly in the reflection and transmission process) was nearly constant with frequency and the attenuation was slightly non-linear with frequency. The reflection coefficient was independent of frequency over the 10 Hz - 10 kHz band. For the sandstone case, the velocity of the Type I and shear waves were only weakly dispersive. From previous results this suggests that the plane wave coefficients should exhibit only a weak frequency dependence. In this case, however, the velocity dispersion of the Type II significantly influenced the plane wave coefficients at high frequency.

For the unconsolidated sediments considered here (silty clay, carbonate sand, and shelly sand of Chapter 5) the excitation of the Type II wave was negligible at all frequencies. In a layered sedimentary sequence (e.g. turbidites in abyssal plains) with multiple interfaces; however, the excitation of the Type II wave may provide a non-negligible loss mechanism not contemplated in the classical single-phase models. Moreover, the existence of such layers introduces the possibility of excited resonances of

the Type II wave in the layer. In any case, if the Type II wave did prove to be important for a layered medium, it would only be important at high frequencies (with respect to the critical frequency) where the Type II wave is propagatory. The losses due to the Type II wave were clearly evident at a single interface for the consolidated sediment (sandstone) at high frequencies.

Finally, the model-to-model and model-to-data comparisons provided some unexpected insight into the propriety of the common use of core data (velocity and attenuation) in developing geoacoustic models. First, core data measured at 400 kHz cannot in the general case be extrapolated in frequency by assuming a linear frequency dependence on attenuation. Second, the core data for sandy sediments may be contaminated by scatter (as was the case in the measurements discussed in Chapter V). The Biot theory can be used in both instances: to either extrapolate in frequency or as an aid in determining the reliability of the core data. Examples of the effect of extrapolation from (synthetic) core data at 400 kHz were given for plane wave reflectivity and surface wave velocity and attenuation.

Bibliography

Addison, S.R., "Study of Sound Attenuation in Sediments," PhD Dissertation, University of Mississippi, December 1984.

Badiey, M., T. Yamamoto, and A. Turgut, "Laboratory and In Situ Measurements of Selected Geoacoustic Properties of Carbonate Sediments," J. Acoust. Soc. Am., 689-696, 1988.

Beebe, J.H., "An Experimental Investigation of Ocean Sediment Effects Upon Long-Range Transmission Loss in Shallow Water," (doctoral thesis), The Pennsylvania State University, University Park, PA, 1981.

Beebe, J.H.; and Holland, C.W., "The Effect of Unconsolidated Sediment Rigidity on Low Frequency Acoustic Propagation in Ocean Seismo-Acoustics," in Ocean Seimo-Acoustics, ed. by T. Akal and J. M. Berkson, Plenum Press, 1986.

Biot, M.A., "Generalized Theory of Acoustic Propagation in Porous Dissipative Media," J. Acoust. Soc. Am., 34, 1254-1264, 1962.

Biot, M.A., "Theory of Elastic Waves in a Fluid-Saturated Porous Solid. I. Low Frequency Range," J. Acoust. Soc. Am., 28, 168-178, 1956.

Biot, M.A., "Theory of Propagation of Elastic Waves in a Fluid-Saturated Porous Solid. II. Higher Frequency Range," J. Acoust. Soc. Am., 28, 168-178,1956.

Brekovskikh, L.M., Waves in Layered Media, 2nd Ed., Translated by Robert T. Beyer, Academic Press, New York, 1980.

Brocher, T.M., "Experimental Studies of Low-Frequency Waterborne and Sedimentborne Acoustic Wave Propagation on a Continental Shelf," J. Acoust. Soc. Am., 960-972, 74, 1983.

Brunson, B.A., and R.K. Johnson, "Laboratory Measurements of Shear Wave Attenuation in Saturated Sand," J. Acoust. Soc. Am., 68. 1371-1375, 1980.

Candel, S. M., and Crance, C. "Direct Fourier Synthesis of Waves in Layered Media and the Method of Stationary Phase," Journal of Sound and Vibration, 74, 477-498, 1981.

Chapman, D.M.F. and D.D. Ellis, "Modeling of Shear Waves on the United Kingdom Continental Shelf," DREA Technical Memorandum 84/p, 1984.

Chotiros, N.P. "High Frequency Acoustic Bottom Penetration: Theory and Experiment," Conference Record, Oceans '89, 1158-1161, 1989

Costley, R.D. "An Experimental Investigation of Acoustic Propagation in Saturated Sands with Variable Fluid Properties," Applied Research Laboratory of the Univers.ty of Texas at Austin, ARL-TR-85-14, 1986.

Clay, C.S., and H. Medwin, Acoustical Oceanography, pg 263-269, John Wiley and Sons, New York, 1977.

Domenico, S.N., "Elastic Properties of Unconsolidated Porous Sand Reservoirs," *Geophysics*, 42, 1339-1368, 1977.

Deresiewicz, H., "The Effect of Boundaries on Wave Propagation in a Liquid-Filled Porous Solid: I. Reflection of Plane Waves at a Free Plane Boundary (Non-Dissipative Case)," Bull. Seism. Soc. Am., 50, 599-607, 1960.

Deresiewicz, H., "The Effect of Boundaries on Wave Propagation in a Liquid-Filled Porous Solid: II. Love Waves in a Porous Layer," Bull. Seism. Soc. Am., 51, 17-27, 1961.

Deresiewicz, H., "The Effect of Boundaries on Wave Propagation in a Liquid-Filled Porous Solid: III. Reflection of Plane Waves at a Free Plane Boundary (General Case)," Bull. Seism. Soc. Am., 52, 595-625, 1962.

Deresiewicz, H., "The Effect of Boundaries on Wave Propagation in a Liquid-Filled Porous Solid: V. Transmission Across A Plane Interface," Bull. Seism. Soc. Am., 54, 409-416, 1964.

Deresiewicz, H., "The Effect of Boundaries on Wave Propagation in a Liquid-Filled Porous Solid: VI. Love Waves In A Double Surface Layer," Bull. Seism. Soc. Am., 54, 417-423, 1964.

Deresiewicz, H., "The Effect of Boundaries on Wave Propagation in a Liquid-Filled Porous Solid: VII. Surface Waves in the Presence of a Liquid Layer," Bull. Soc. Am., 54, 425-430, 1964.

Deresiewicz, H., and J. T. Rice, "The Effect of Boundaries on Wave Propagation in a Liquid-Filled Porous Solid: IV. Surface Waves In A Half-Space," Bull. Seism. Soc. Am., 52, 627-638, 1962.

Deresiewicz, H., and R. Skalak, "On Uniqueness in Dynamic Poroelasticity," Bull. Seism. Soc. Am., 53, 783-788, 1963.

Dicus, R.L., and R.S. Anderson, "Effective Low-Frequency Geoacoustic Properties Inferred from measurements in the Northeast Atlantic," Naval Ocean Research and Development Activity, NSTL Station, Miss., 1982.

Ellis, D.D., and D.M.F. Chapman, "Propagation Loss Modeling on the Scotian Shelf: Comparison of Model Predictions with Measurements," in Bottom Interacting Ocean Acoustics, ed. by W.A. Kuperman and F.B. Jensen, Plenum Press, 1980.

Feng, S., and D.L. Johnson, "High-Frequency Acoustic Properties of a Fluid/Porous Solid Interface. I. New Surface Mode," J. Acoust. Soc. Am., 906-914, 1983a.

Feng, S., and D.L. Johnson, "High-Frequency Acoustic Properties of a Fluid/Porous Solid Interface. II. The 2D Reflection Green's Function," J. Acoust. Soc. Am., 915-924, 1983b.

Fryer,G. J., "Reflectivity of the Ocean Bottom at Low Frequency," J. Acoust. Soc. Am., 68, 35-42, 1978.

Geertsma, J., and Smit, D.C. "Some Aspects of Elastic Wave Propagation in Fluid-Saturated Porous Solids," Geophysics, 27, 169-181, 1961.

Hamilton, E.L., "Geoacoustic Modeling of the Seafloor," J. Acoust. Soc. Am., 68, 1313-1339, 1980.

Holland, C.W., "Shear Wave Excitation in Unconsolidated Ocean Sediments," (unpublished master's thesis), University Park, PA, 1985.

Holland, C.W., and B.A. Brunson, "The Biot-Stoll Sediment Model: An Experimental Assessment," J. Acoust. Soc. Am.,84, 1437-1443, 1988.

Hovem, J.M., and G.D. Ingram, "Viscous Attenuation of Sound in Saturated Sand," J. Acoust. Soc. Am., 66,1807-1812, 1979.

Hughes, S.J., D.D. Ellis, D.M.F. Chapman, and P.R. Staal, "Low-Frequency Acoustic Propagation Loss in Shallow Water over Hard-Rock Seabeds Covered by a Thin Layer of Elastic-Solid Sediment," J. Acoust. Soc. Am., 88, 283-297, 1990.

Hunter, A.N., "Measurement of Acoustic Attenuation and Velocity in Sand," Acoustica, 11, 1961.

Ingenito, F., "Measurements of Mode Attenuation Coefficients in Shallow Water," J. Acoust. Soc. Am., 53, 858-863, 1973.

Ingenito, F., and S.N. Wolf, "Acoustic Propagation in Shallow Water Overlying a Consolidated Bottom," J. Acoust. Soc. Am. 60, 611-617, 1976.

Kibblewhite, A.C., "Attenuation of Sound in Marine Sediments: A Review with Emphasis on New Low-Frequency Data," J. Acoust. Soc. Am., 86, 716-738, 1989.

McDaniel, S.T., and J.H. Beebe, "Influence of Semiconsolidated Sediments on Sound Propagation in a Coastal Region," in Bottom Interacting Ocean Acoustics, ed by W.A. Kuperman and F.B. Jensen, 1980.

Muir, T.G., C.W. Horton and L.A. Thompson, "The Penetration of Highly Directional Acoustic Beams into Sediments," J. Sound Vib. 64, 539-551, 1979.

Muller, D.E., "A Method for Solving Algebraic Equations Using an Automatic Computer," Math. Tables and Aids to Comp., 10, 208-215, 1956.

Paterson, N.R., "Seismic Wave Propagation in Porous Granular Media," Geophysics, 21, 691-714, 1956.

Plona, T.J., "Observation of a Second Bulk Compressional Wave in a Porous Medium at Ultrasonic Frequencies," Appl. Phys. Lett., 36, 259-261, 1980.

Plona, T.J., and K.W. Winkler, "Scattering of Fast and Slow Compressional Waves in Fluid Saturated Porous Media," in Multiple Scattering of Waves in Random Media and Random Rough Surfaces, ed. by V.J. Varadan and V.V. Varadan, Plenum Press, 1985.

Roever, W.L., Vining, T.F., and E. Strick, "Propagation of Elastic Wave Motion from an Impulsive Source Along a Fluid/Solid Interface," Philos. Trans. R. Soc. London, Ser A 251, 455-523, 1959.

Rubano, L.A.,"Acoustic Propagation in Shallow Water Over a Low Velocity Bottom," J. Acoust. Soc. Am.,67,1608-1613,1980.

Satkowiak, L., "Acoustic Transmission Across the Water/Sediment Interface,"J.Acoust. Soc. Am. Suppl. 1, 84, S120, Fall 1988.

Shirmer, F., "Experimental Determination of Properties of the Scholte Wave in the Bottom of the North Sea," in "Bottom Interacting Ocean Acoustics," ed. by W. A. Kuperman and F. B. Jensen, Plenum Press, New York, 1985.

Schmidt, H., and F.B. Jensen, "A Full Wave Solution For Propagation in Multilayered Viscoelastic Media with Application to Gaussian Beam Reflection at Fluid-Solid Interfaces," J. Acoust. Soc. Am., 77, 813-825, 1985.

Stoll, R.D., "Acoustic Waves in Saturated Sediments," in Physics of Sound in Marine Sediments, ed. by L. Hampton, Plenum Press, 1974.

Stoll, R.D., "Acoustic Waves in Ocean Sediments," Geophysics, 42, 715-725, 1977.

Stoll, R.D., "Experimental Studies of Attenuation in Sediments," J. Acoust. Soc. Am., 66, 1152-1160, 1979.

Stoll, R.D., "Theoretical Aspects of Sound Transmission in Sediments," J. Acoust. Soc. Am., 68, 1341-1350, 1980.

Stoll, R.D., and Kan, T.K. "Reflection of Acoustic Waves at a Water-Sediment Interface," J. Acoust. Soc. Am., 70, 149-156, 1981.

Strutt, J.W. (Lord Rayleigh), "On Porous Bodies in Relation to Sound," Philos. Mag. 16 (5), 181-186, 1883.

van der Hijden, J.H.M.T., "Quantitative Analysis of the Pseudo-Rayleigh Phenomenon," J. Acoust. Soc. Am., 75, 1041-1047, 1984.

Vidmar, P.J., "Ray Path Analysis of Sediment Shear Wave Effects on Bottom Loss Reflection," J. Acousst. Soc. Am. , 68, 639-648,1980.

Vidmar, P.J., "The Effect of Sediment Rigidity on Bottom Reflection Loss in a Typical Deep Sea Sediment," J. Acoust. Soc. Am., 68, 634-638, 1980.

Winkler, K.W., "Dispersion Analysis of Velocity and Attenuation in Berea Sandstone," J. Geophys. Res., 90, 6793-6800, 1985.

Wolfram, S.W., Mathematica: A System of Doing Mathematics by Computer, Addison Wesley, 1988.

Yamamoto, T., "Acoustic Propagation in the Ocean with a Poro-elastic Bottom," J. Acoust. Soc. Am., 73, 1587-1596, 1983a.

Yamamoto, T., "Propagator Matrix for Continuously Layered Porous Seabeds," Bull. Seism. Soc. Am., 73, 1599-1620, 1983b.

Yamamoto, T., and A. Turgut, "Acoustic Wave Propagation Through Porous Media with Arbitrary Pore Size Distributions," J. Acoust. Soc. Am., 83, 1744-1751, 1988.

Zwikker, C., and Kosten, C.W., Sound Absorbing Materials, Elsevier, New York, 1949.

APPENDIX A

Definition of the Complex Elastic Moduli

The complex elastic moduli were shown by Stoll (1974) to depend upon the bulk moduli of the fluid, solid, and frame constituents in the following way:

$$C = K_S (K_S - K_m) / (D - K_m)$$

$$H = (K_S - K_m)^2 / (D - K_m) + K_m + 4\mu/3$$

$$M = K_S^2 / (D - K_m)$$

$$D = K_S (1 + \beta (K_S / K_f - 1))$$

where K_S is the bulk modulus of the individual grains, K_f is the bulk modulus of the interstitial fluid, and K_m is the complex bulk modulus of the sediment frame. In the general case, the grain bulk modulus can be complex to account for losses within the individual grains; however, in this work only the frame bulk modulus and the frame shear modulus, μ, are complex. Losses arising from a non-ideal interstitial fluid are taken into account via the viscosity rather than a complex modulus.

APPENDIX B

Numerical Methods

In general, the computations required a high degree of precision. This is primarily due to the disparate values of the material parameters that comprise a marine sediment; the difference between the smallest and largest parameter typically spans 15-20 orders of magnitude (e.g., see Table 2.1). This resulted in numerical instabilities, for example, in the solution of Eq (2.70) using Cramer's rule. Partial pivotal scaling and use of double precision was sufficient render the matrix calculations stable.

The most difficult numerical problem encountered was the solution of the secular equation which required finding roots of a transcendental equation in the complex plane. Few numerical methods for solution of such a problem in fact exist. Muller's (1956) method was attempted but was *non-con*vergent even at double precision arithmetic. Thus the behavior of the solution surface was too erratic (under-resolved) for the granularity of the number system of the dependent variable. *Mathematica* TM (Wolfram (1988)) software, which allows arbitrary precision, was then employed using the secant method extended to the complex plane. This technique was successful and reasonably efficient (less than fifty iterations were usually sufficient for convergence) in finding the roots to the secular equation.

The numerical implementation of the theory was coded in Microsoft Fortran and executed on an 80386 personal computer with an 80387 math co-processor. IMSL routines were employed to evaluate the Kelvin function and its first derivative, the plane wave coefficients, and the FFT.

APPENDIX C

Derivation of the location of the virtual source

Candel and Crance (1981) derive the location of the virtual source for a lossless two-fluid boundary. The equations for a porous medium can be rewritten as:

$$x_i = h\left[\left(\frac{V_i}{V_o}\right)^2 - 1\right]\tan^3\theta_{oi}$$

$$z_i = h\frac{V_o}{V_i}\left(\left[1-\frac{V_i^2}{V_o^2}\sin^2\theta_{oi}\right]^{1/2} \Big/ \cos\theta_{oi}\right)^3 \qquad \text{(C-1)}$$

where the subscript i = p, 2 refer to the Type I and Type II wave, respectively. That is, for a given source/receiver geometry, the angle of incidence (θ_{oi}) corresponding to the steepest descent geometrical ray path will be different for each wave type. Note that the quantity

$$\left[1-\frac{V_i^2}{V_o^2}\sin^2\theta_{oi}\right]^{1/2} \Big/ V_i$$

should be taken such that the imaginary part is negative (which follows from the radiation conditions discussed in Chapter 2). Now Eq. (C-1) together with Eq. (4.22) requires that θ_{oi} be complex. The transcendental equation for θ_{oi} can be written as :

$$z \sin\theta_{oi} = (h \tan\theta_{oi} - x) V_o \left[1 - \frac{V_i^2}{V_o^2} \sin^2\theta_{oi} \right]^{1/2} \Big/ V_i \quad . \qquad \text{(C-2)}$$

In order to preserve the meaning of the geometrical ray path, the following changes are made to the virtual source position as derived by Candel and Crance (1981). The angle of the ray connecting the receiver and the boundary will be redefined as the angle of the planes of constant phase, which is a real angle and given by Eq. (4.27). Eq. (4.27) can be rewritten to depend on source/receiver geometry and angle of incidence as follows :

$$z \sin\theta_{oi} = (h \tan\theta_{oi} - x) V_o \, \mathrm{Re}\left\{ \left[1 - \frac{V_i^2}{V_o^2} \sin^2\theta_{oi} \right]^{1/2} \Big/ V_i \right\} \quad . \qquad \text{(C-3)}$$

Note that the angle of incidence is also now real. For the results in Chapters 4 and 5, Eq. (C-3) is first solved numerically for θ_{oi}, the x coordinate of the virtual source position is then given by Eq. (C-1) and finally the z coordinate of the virtual source is obtained from Eq. (4.22) as

$$z_i = z + (x - x_i) \left[1 - \frac{V_i^2}{V_o^2} \sin^2\theta_{oi} \right]^{1/2} \Big/ \left(\frac{V_i}{V_o} \sin\theta_{oi} \right) \quad . \qquad \text{(C-4)}$$